8-2017

Fluid Dynamics of Watercolor Painting : Experiments and Modelling

David Edward Baron
Montclair State University

Abstract

In his classic study in 1908, A.M. Worthington gave a thorough account of splashes and their formation through visualization experiments. In more recent times, there has been renewed interest in this subject, and much of the underlying physics behind Worthington's experiments has now been clarified. One specific set of such recent studies, which motivates this thesis, concerns the fluid dynamics behind Jackson Pollock's drip paintings. The physical processes and the mathematical structures hidden in his works have received serious attention and have made the scientific pursuit of art a compelling area of exploration. Our current work explores the interaction of watercolors with watercolor paper. Specifically, we conduct experiments to analyze the settling patterns of droplets of watercolor paint on wet and frozen paper. Variations in paint viscosity, paper roughness, paper temperature, and the height of a released droplet are examined from time of impact, through its transient stages, until its final, dry state. Observable phenomena such as paint splashing, spreading, fingering, branching, rheological deposition, and fractal patterns are studied in detail and classified in terms of the control parameters. Using the one-dimensional (1-D) Saint-Venant differential equations, which are a simplification of the three-dimensional (3-D) Navier-Stokes equations from fluid dynamics, we created a computer-simulated, mathematical model of a droplet splash of watercolor paint onto a flat surface. The mathematical model is analyzed using a MATLAB code which considered changes in droplet height, radius, and velocity of dispersal over time. We also implemented a stochastic version of the Saint-Venant equations which captured the random fingering patterns of a droplet splash. Initial conditions for height, radius, and velocity of a radially spreading droplet were given at the onset of the simulation. Dynamic viscosity and fluid density were parameters incorporated into this system of differential equations, which could be easily adjusted in the MATLAB code for the paint type to be simulated. The stochastic nature of our model was designed to recreate the complex behavior of water splashes, the non-homogeneity of the watercolor paper, and the resulting patterns. We then computed the fractal dimension of each computer-generated droplet image to compare theoretical and experimental values. Analysis of the set of data consisting of over 10,000

trials was conducted to determine any significant statistical correlations among the spreading pattern, the number of fingers, viscosity, density and fractal dimension. Finally, we extended the system of differential equations based on the Saint-Venant equations to include the effects of temperature upon the paint-spreading pattern. In a similar manner, we compared the theoretical values of fractal dimensions generated by our MATLAB model to the experimental results for paint droplets on a frozen substrate.

Fluid Dynamics of Watercolor Painting: Experiments and Modelling

By

David Edward Baron

A Master's Thesis Submitted to the Faculty of

Montclair State University

In Partial Fulfillment of the Requirements

For the degree of

Master of Science

August 2017

College of Science and Mathematics

Department of Mathematics

Thesis Committee:

[redacted]

Dr. Ashwin Vaidya

[redacted]

Dr. Haiyan Su

[redacted]

Dr. Eric Forgoston

FLUID DYNAMICS OF WATERCOLOR PAINTING:

EXPERIMENTS AND MODELLING

A THESIS

Submitted in partial fulfillment of the requirements

For the degree of Masters in Mathematics

By

David Edward Baron

Montclair State University

Montclair, NJ

August 2017

MONTCLAIR STATE UNIVERSITY

Acknowledgements

I am very grateful to Dr. Ashwin Vaidya for giving me the opportunity to write this thesis under his direction, for identifying the relevant literature on this vast topic, for teaching me to be a better scientist, and for encouraging me to publish this research.

I also want to thank Dr. Haiyan Su for giving her time to be part of this scientific and creative endeavor, and for doing the statistical analysis.

Finally, I want to thank Dr. Eric Forgoston for his contribution to this paper and for his critical analysis, giving a deeper insight into the mathematics involved in our research.

Contents

List of Figures

List of Tables

Chapter 1: Introduction and Literature Review

Section 1.1 The Fluid Dynamics of Art

The literature available on experiments involving droplet splashes is extensive. From Newtonian fluids to non-Newtonian fluids, droplets onto hard surfaces or onto a thin, liquid film, splash dynamics are a complex, remarkable, and beautiful phenomenon to observe and to study. The investigation of the physics that drives the resulting fluid mechanics is rich not only in analytical content but also in mathematical models that attempt to predict droplet behavior from the moment of impact and afterward, given some initial conditions and varying parameters. Crown formation, deposition, and dispersion are just a few of the noticeable characteristics that a droplet might produce upon splash impact, and its practical application is vast, from ink jet printing to aerosol spraying; from particle ejection for seed dispersal to molecular aggregation in cloud nucleation.

Recent review papers discuss advancements in the study of the field up until the last decade. In this regard, studies concerning the impact of droplets on dry surfaces are most relevant to our own work. The experimental work by Rioboo, *et al*. [25], explored the impact of different liquids on solid surfaces corresponding to varying surface roughness. Their investigations revealed six categories of splashes: deposition, prompt splash, coronal splash, receding break-up, partial rebound, and complete rebound, which depend upon the properties of the liquid and surface. In addition to the roughness of the surface, the viscosity, density, and surface tension of the liquid droplet have been recognized as being significant, and the different regimes of droplet splashes are often expressed in terms of three dimensionless quantities, namely the Reynolds (*Re*), Weber (*We*), and Ohnesorge (*Oh*) numbers which depend upon the afore-mentioned parameters.

The viscosity of the droplet and friction of the surface determine the initial stages of the splash while surface tension takes control of the final stages, when the drop thickness on the surface is diminished. The prominent regimes are distinguished by the parameter $K = We\sqrt{Re}$, the critical value of which determines the onset of splashing [8].

There has also been a substantial amount of work on the splash patterns of non-Newtonian and particle laden droplets [8,15,20,22,26]. As might be expected, non-Newtonian characteristics such as viscoelasticity, yield-stress, and shear-thinning result in marked variation in the observed post-impact behavior of droplets. These have been categorized as irreversible viscoplastic, perfect elastic recoil, and viscoelasticity. In the case of non-Newtonian fluids, the Deborah number (*De*), the critical strain parameter (Υc), and the Mach number (*M*) have been used to classify the various, observed regimes. The splash dynamics of droplets with embedded particles is equally interesting and unique. For droplets with a sufficiently low particle concentration, the parameter *K* has been employed to characterize the drop impact with the viscosity μ replaced by an effective, concentration-dependent viscosity μ_e. In the case of high concentration droplets, it is observed that a reinterpretation of the Weber number, based on particle characteristics, is needed to accurately capture the onset of splashing.

Ivo Peters, *et al*. [14] investigated the impact of droplets of spherical glass and zirconium dioxide (ZrO_2) beads in water suspension onto a solid substrate. They studied three types of suspensions – two uniform suspensions of beads, one with a 78-micrometer radius bead and one with a 362-micrometer radius bead and a third mixture containing a 50/50 combination of the two sizes of particles – to demonstrate a correlation between droplet radius and surface tension and thus, derived a particle-based Weber number. The

Weber number is a dimensionless number that relates droplet impact velocity and radius to surface tension and is crucial in driving the dynamics of a splash, $We = \frac{\rho D V_h^2}{\sigma}$, ρ is the density of the fluid, *D* refers to the characteristic length, which is taken to be the diameter of the droplet, V_h is the impact velocity of the droplet, and σ is surface tension. Peters' revised, particle-based Weber number is roughly equivalent to the ratio of kinetic energy at impact to the surface energy which is simply the energy required for a particle to escape the inside of a droplet by overcoming surface tension. This ratio is now dependent on the particle radius as well as the particle density and yields the following result: $\frac{E_{kin}}{E_{surf}} = \frac{1}{6} We_p$, where We_p is the particle based Weber number. The findings of this groups' experiments predict that a $We_p > 14$ is the threshold at which splashing may occur. Splashing is defined by Peters as the ejection of particles or secondary droplets from the initial droplet [14]. In our experiments, we used permanent rose, Prussian blue, and sepia watercolor paints dissolved in water. If we consider these as suspensions, which is a reasonable assumption based on the chemical composition of watercolor paint which will be discussed later, we can show that our experimental results fall within Peters' predictions. Droplets for some of our early experiments were released from a straw which had a diameter of roughly 0.6 cm. Using this value, as a lower bound, in the formula based on the particle-based Weber number, we found our We_p values to be about 20, thus the occurrences of splashing at a height of 6 inches and having an impact velocity of about 1.73 m/sec, conditions which might seem insufficient as to produce a splash, are however, consistent with the predictions of Peters $et\ al.$ For our droplets released with a medicine dropper having a diameter of approximately 0.3 cm, we calculated a particle-based Weber

number of about 10, well below the threshold of splash onset. This is similarly confirmed in our experimental results.

Deegan, Brunet, and Eggers [37] posit that an ejecta sheet is formed at the moment of impact between a fluid drop and a thin fluid layer of the same liquid, which projects outward in the horizontal direction and it contains, in that instant, an equal amount of drop fluid as layer fluid. As the drop penetrates the layer, the sheet thickens and a greater percentage of the sheet comes from the layer fluid. Ejecta sheet spreads were measured experimentally by this team and showed high speeds with decreasing viscosity, reaching up to 50 m/s. These researchers discussed the results of their series of experiments analyzing ejecta sheets and splashes for water, propanol, silicon oil, and glycerol/water mixture into shallow pools of the same liquid as the droplet. Our experiments explore paint drops onto wetted, solid, porous surfaces.

S.D. Howison and his colleagues [41,60] derived models for four stages of an inviscid (having no or negligible viscosity) droplet onto a thin film of incompressible (when divergence equals zero) liquid. In a physical sense, divergence, $\nabla \cdot$, is a measure of the quantity of flux emanating from any point in a vector field or the rate of loss of mass, heat, $etc.$, from it. First, the splash jet initiation stage, where the contact length is comparable with the layer depth; second, when the nominal penetration depth is comparable with the layer depth, called splash jet growth; third, when the jet thickness is comparable with the layer depth, known as splash jet and layer interaction, and fourth when the penetration depth is comparable with the initial droplet radius [37]. Yarin and Weiss categorized the various types of splashes, and detailed his experiments, devised to gain insight into splash behavior to derive a concise, predictive formula for theoretical

understanding as well as for practical use. Both Howison and Yarin derived mathematical models for simulations and computations comparing theoretical values with experimental data collected when observing jet formation, crown formation as well as crown position, when inertial forces dominate viscous forces. Jetting occurs when inertial forces dominate surface tension and liquid is squeezed out radially. However, the subject of our review combines the phenomenon of rheological deformation and deposition of particles in suspension along with the droplet impact on a wetted or frozen, porous substrate and incorporates a temperature variable component, thus affecting the viscosity of a fluid, specifically watercolor paint. To our knowledge, this is an area that has not been studied.

To understand the fluid dynamics of paint, we must first define a fluid; explore its behavior along with the associated properties that will govern a fluid's motion. A fluid is defined as any substance that deforms continuously when subjected to an applied shear stress, i.e. a tangential force (F) per unit area (A). The more stress that is applied, the more the fluid will deform. Shear stress will play an important role in deriving the equations of fluid motion. We can express shear stress, τ, as $\tau \approx \frac{F}{A}$, force per unit area. One critical assumption of fluids that permits us to study its behavior is the continuum hypothesis, which neglects the fact that fluids, in fact, consist of billions of individual molecules or atoms in a small region, and, instead, treats the properties (e.g. velocity, temperature, etc.) as if it were a continuum. If we forgo the use of the continuum hypothesis, the structure of the fluid consists of molecules moving about more or less randomly. If we are able to measure for example, the velocity at the molecular level, we will obtain the result at only a particular instance in time. If, instead, we average the velocities of the molecules in a region surrounding a particular point, we can derive a representative value for the velocity

at any desired point. Thus, we identify with each point, a "fluid parcel" and then consider the volume of the fluid as a whole to be continuous aggregation of fluid parcels [35].

An important property of a fluid is its viscosity or a fluid's resistance to shear stress. Consider a fluid region confined between an upper and lower plate, separated by a distance, h, moving at a velocity, U. If the bottom plate remains stationary, the velocity at this point $y = 0$, is also zero, a state called the no-slip condition. The first layer of fluid parcels away from the wall imposes tangential forces on the next layer, and so on. Note that this whole argument rests on the assumption that all fluid particles in a region are defined in a continuous way. If we apply a constant force, *F*, the upper plate moves with a steady velocity and furthermore, the force required to move the plate with a constant velocity, *U*, is directly proportional to both the area, *A*, of the plate and to velocity *U*, and inversely proportional to *h*, the distance between the plates. If we let μ be a constant of proportionality, then we have $F = \frac{\mu AU}{h}$. But since shear stress equals $\frac{F}{A}$, we then have $\frac{F}{A} = \tau = \frac{\mu U}{h}$. In differential form, $\frac{du}{dy} = \frac{U}{h}$, where u is the x-component of the velocity vector which changes only in the y-direction. Thus, shear stress is proportional to the rate of deformation with viscosity, μ, being the constant of proportionality. Hence, we have Newton's Law of Viscosity: $\tau = \frac{\mu U}{h}$, and since the velocity at any point in the fluid can be given by $\frac{du}{dy} = \frac{U}{h}$, we thus have $\tau = \mu \frac{du}{dy}$. We need to differentiate between dynamic viscosity, which is the ratio of the tangential force per area, and kinematic viscosity, which is the ratio of dynamic viscosity to density, i.e. $\frac{\mu}{\rho}$. The Reynolds number, *Re*, is a dimensionless number that relates inertial forces to viscous forces and is useful in

predicting fluid behavior, $Re = \frac{\rho D V_h}{\mu}$. Smooth, constant motion or laminar flow is characterized by a low Reynolds number when viscous forces are dominant. Turbulent flow occurs at a high Reynolds number when inertial forces tend to produce flow instabilities. Inertial forces come from applying Newton's Second Law of Motion, *F = ma, force = mass x acceleration*; viscous forces from Newton's Law of Viscosity. A given fluid will possess a density, ρ. The ratio of inertial forces to viscous forces equals $\frac{\rho U^2 L^2}{\mu U L} = \frac{\rho U L}{\mu} = Re$, Reynolds number [35]. A high Reynolds number indicates that inertial forces dominate the system; a low Reynolds number implies viscous forces are dominant. We need also to make use of the Navier-Stokes equations for fluid flow, the general form of which describes fluid behavior in three dimensions, but the foundation of which can be represented by using Newtonian mechanics *i.e.* the conservation of mass and the balance of momentum.

Luu and Forterre [18] utilize a simplification of the Navier-Stokes equations by making several assumptions and thus enabling them to use the Saint-Venant equations. First, they assume the surface tension of an aqueous solution to be *0.07 N/m*, the same as pure water. The surface tension of gels, analyzed by this team, was experimentally determined to be, in fact, less than that of water, thus this value provides an upper bound. Second, they considered the simplest time-dependent model of inertial spreading by using a shallow disc that spreads radially along a surface with thickness given as $h(t)$ and radius as $R(t)$. They neglect gravity, hoop stress and radial stress, hysteresis (secondary droplet ejection), and dissipation, since these factors and their contributions to the comprehensive dynamics of the droplet spread are negligible in yield-stress fluids. The viscosity of the yield-stress

fluids they used in their experiments is high compared to the surface tension and hence, they neglect surface tension. In our experiments, we released droplets of watercolor paint onto water-wetted substrates and similarly, we can neglect gravity, hoop and radial stress. We will assume that surface tension and capillary forces are negligible. From Lu and Forterre, we were able to utilize the following system of ordinary differential equations to model a radially spreading droplet given by considering various aspects of the physical problem such as the basal shear stress, τ_β which scales as velocity divided by height, U/h and is much larger than the elongation rate U/R in the shallow limit.

Our current work explores the interaction of watercolor paints with watercolor paper. Specifically, we conducted experiments to analyze the settling patterns of droplets of watercolor paint on wet and frozen paper. Variations in paint viscosity, paper roughness, paper temperature, and the height of a released droplet are examined from time of impact, through its transient stages, until its final, dry state. Observable phenomena such as paint splashing, spreading, fingering, branching, rheological deposition, and fractal patterns are studied in detail and classified in terms of the control parameters. The iconic photographs of splashes taken by Arthur Worthington in 1908 and Harold Edgerton in 1936 are famous not only for the mathematics and physics captured in an instant by a flash photograph, but also for the inherent beauty of a subject that has intrigued both artists and scientists alike for centuries [26]. Furthermore, a revolutionary art form was born in the mid-twentieth century when American artist Jackson Pollock dripped paint onto his canvases, thus beginning the abstract expressionist movement of visual arts, sometimes called “action painting”. Pollock dripped paint from trowels, sticks, and punctured cans to create his unique style, which has been emulated by enthusiasts and even imitated for profit by

forgers. Richard Taylor's studies of Pollock's work by utilizing fractal geometry analysis to authenticate a Pollock drip-style painting is both intriguing and controversial. The physics of art has become an exciting area of research for scientific investigation.

In 1941, F.I.G. Rawlins published one of the earliest reports on the subject when he was Scientific Advisor to the National Gallery in London. His work focused primarily on the maintenance, preservation, and restoration of the centuries-old works by the great masters, on the details of the oil medium, and on the varnish crackle that would differentiate an authentic masterpiece from a forgery, and generally gave art lovers and historians an understanding of the many levels that comprise a painting, $i.e.$ the support, the ground, the paint, and the tools. It is of paramount importance for the artist to have a knowledge of the materials that are used when creating a painting to gain a true insight into the fluid dynamics that shape art, and in our particular case watercolor painting, an area not thoroughly discussed by Rawlins. In fact, very little attention has been given to the scientific investigation that drives the mechanics of the watercolor medium. To that end, we must understand rheology. G.W. Scott Blair, presents a contemporary discussion of the subject by defining rheology as the science that deals with the flow and deformation of matter, primarily materials whose characteristics lie between those of crystalline solids and true liquids. A material that will not flow when small forces are applied is called a solid. A material that flows under the smallest measurable forces is called a fluid. A Newtonian liquid, or a perfect liquid, is one which flows at a steady rate under a steady pressure and whose rate of flow is proportional to the pressure, *i.e.* it flows twice as fast when the pressure is doubled. Water, light oils, and many other liquids, such as benzene and alcohol are very near to Newtonian. Fluids that do not behave in this manner are called non-

Newtonian liquids. Many paints and oils contain resins that have both solid and liquid properties. Solid particles mixed into liquids are called suspensions. A crucial property of liquids that will play an important role in our analysis of watercolor paint is called viscosity, which is, generally speaking, a fluid's thickness or internal friction. More precisely defined as pressure divided by rate of flow, viscosity is a measure of a fluid's resistance to deformation. Water has a low viscosity, while honey has a high viscosity. Still further, there are some materials that will not flow under very low pressures and would thus be considered solids, but under higher pressures, they flow readily. These substances, ketchup or mayonnaise for example, are termed yield-stress fluids. Watercolor paints are a curious mixture of these materials and their respective properties [19].

Marmanis and Thoroddsen examine the phenomenon of finger structures that emerge upon impact when a droplet hits a solid surface or substrate. Following the work of Marmanis and Thoroddsen, we estimate the *"number of fingers"* as a function of height for various cases that show clear, fingering patterns. As in their review, *"…everything that resembles a finger, no matter how short…"* is regarded as a finger. They performed experiments by releasing droplets from a 5-mm inner diameter syringe containing bromophenol blue dye from varying heights to attain impact velocities ranging from 0.77 m/s to 4.9 m/s, ignoring air resistance and simply using the kinematic formula $U = \sqrt{2gH}$, where g is acceleration due to gravity and H is the height of the released droplet. They derive an impact Reynolds number, Re_I, calculated as follows: $Re_I = (\frac{U}{\sqrt{\nu}})\sqrt[4]{(\frac{\pi^2 \rho D^3}{16\sigma})}$ which is proportional to $\sqrt[2]{Re_D}\sqrt[4]{We}$ and thus correlating this impact Reynolds number to the number of fingers that protrude outward from a droplet splash. The range of values for

Reynolds and Weber numbers in Thoroddsen and Marmanis's experiments were *1,100 < Re < 25,000* and *100 < We < 4,000*. In our study, the Weber number ranged from *150-323*, while the Reynolds number varied from *2,600-10,200*. The number of fingers, they conclude, is weakly dependent on the surface tension and depends primarily on inertial-viscous interactions. Using the Reynolds and Weber numbers calculated in our own experiments to compute the impact Reynolds number for our watercolor paints demonstrates results which fit nicely with the results of these researchers. Aside from the fact that we used paint in our experiments, our work differs from this article in another key aspect. Marmanis and Thoroddsen used dry, linen paper at room temperature as the flat surface upon which their droplets splashed. We will see that there is a direct correlation between fingering and height as is concluded in this article, however, we used wetted watercolor paper at or below room temperature, thus allowing for fluid diffusion and particle dispersal after impact [24].

Karol Mysels [16] examined the effects of surface tension that arise among various liquids such as oil, water, alcohol, and surfactants. Surface tension is defined as the tendency of a liquid to assume a spherical form in the absence of external forces, because, for a given volume of liquid, the spherical form presents the smallest possible surface in contact with other substances, e.g. oil in water. Mercury has a high surface tension, water has a low surface tension, and soapy water is lower even still. In the process of painting, capillarity plays an important role in the interactions between paint brush hairs and water as well as between water and porous watercolor paper, as explained by Mysels. For our purposes, the capillarity effects between brush hairs and water do not play a role in our experiments, since we dripped paint from two different heights. We nonetheless, leave for

future investigation and experiments, the study of water flow and paint dispersal affected by paint brushes as exhibited in some figures which follow. Mysels discussed to some extent the effect of the porosity of the paper substrate on watercolor paints' tendency to flow. Rate of spreading will depend on how free the liquid is to move, particularly, on whether there is any free liquid on the surface not held in pores. There are a few factors that can reduce the tendencies of fluid to spread or to retract. They are, for example, related to the roughness of a surface, to the deposit of particles from the liquid causing the surface under the liquid to differ significantly from that surrounding it, to the swelling of wetted paper, and to the occurrence of evaporation and the loss of liquid into the pores. The tendency of the liquid to enter the pores of the surface depends primarily on how fine the pores are. The finer the pores, the more surface involved for a given amount of liquid and therefore the stronger is the tendency of the liquid to enter them that is, to be absorbed by the paper. Particles may be pressed together by surface tension that exists among the paint, the paper, and the water [16]. We recognize this absorption process of paint into the canvas to be an important aspect of fluid dynamics involved in our investigation.

Section 1.2 The Art of Fluid Dynamics

Thus, it is from this vantage point that this thesis takes its motivation, *i.e*. to analyze the fluid dynamics of art or perhaps more appropriately the art of fluid dynamics. We were inspired by the many complex and beautiful patterns that result from sediment residues, (rheology), in the watercolor medium. The authors of this paper designed and performed "single-paint-droplet" experiments to reduce the watercolor painting process down to a procedure with simplest parameters. We released droplets of three types of watercolor paint, *i.e.* three different viscosities, from two distinct heights onto three types

of watercolor paper each with its own roughness, *i.e*. porosity, at three different temperatures. The results were categorized by the final, dry image of each painting and analyzed for any statistical correlation from any of the parameters, height, viscosity, etc., to a discernable or even reproducible pattern within the final dry painting. We draw motivation for our experiments from the complex nature and behavior of water and how watercolor painting is an immediate consequence of fluid dynamics. American watercolor artist Carol Grigg, for example, whose best-known works portray scenes from the American southwest, makes brilliant and stunning use of watercolor pigments' inherent viscosity and material composition to create patterns which seamlessly and effortlessly find their way into her paintings. The physical processes and the mathematical structures hidden in Jackson Pollock's paintings have received serious attention within the past two decades, and have made the investigation of the connections between science and art a compelling area of exploration. We return to the work of Richard Taylor and fractal analysis as a means for a new metric to examine our painting experiments.

The method of box counting was implemented to approximate the fractal dimension of each painting. Benoit Mandelbrot, the father of fractal geometry, defines a fractal as *"…geometric shapes that…if a piece…is suitably magnified to become the size of the whole, it should look like the whole, either exactly, or perhaps only after a slight limited deformation."* Mandelbrot's article, published in the journal *Leonardo* in 1989 gives a brief account of his inspiration for this new creation and its development into a branch of mathematics, its correlation to art and natural patterns, and ultimately the need for the computer's invention and development to understand, explore, and advance this new geometry along with its connection to iterative functions. Fractals encompass an enormous

collection of geometric patterns that lie outside Euclidean geometry and their complex mathematical form has in fact generated a new form of art. Fractals have a non-integer dimension [39].

Fractals can be generated with analytical precision using computers as evidenced in Figure 1. Fractal geometry or fractals, a twentieth-century mathematical advancement, quantifies shapes or forms or patterns that lie outside Euclidean geometry. Remarkably and curiously, fractals can be seen virtually everywhere in the natural world, from coast lines and river deltas, to vast salt flats and mountain ranges; from the path of a lightning bolt to the aggregation of sediment particles, even the shapes of the food we eat.

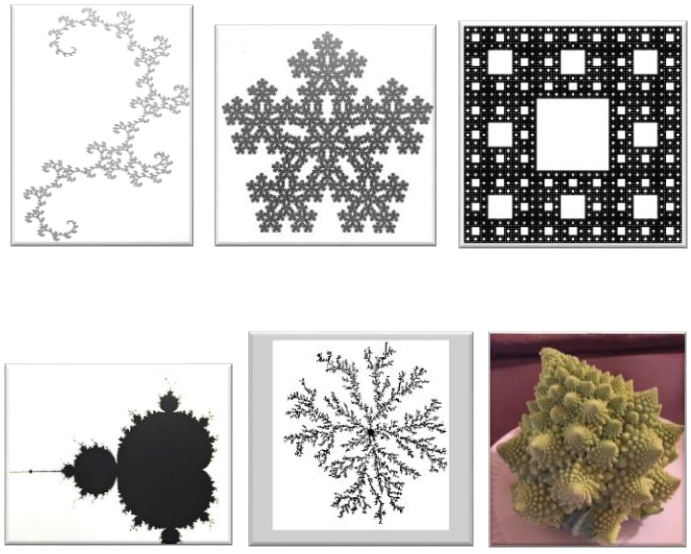

Figure 1. Golden Dragon, $D_f = 1.61803$, Pentaflake, $D_f = 1.8617$, Sierpinski Carpet, $D_f = 1.8928$, Mandelbrot Set, $D_f = 1.9340$, Diffusion Limited Aggregation, $D_f = 1.7$, Romanesco Broccoli, $2 < D_f < 3$.

Richard Taylor's numerous articles on his use of computers and fractal pattern studies to examine the paintings of Jackson Pollock are fascinating in their claims and discoveries. Taylor classified Pollock's drip works into three categories based upon the range of fractal dimension thus indicating the year Pollock would most likely have painted a particular work – the preliminary years, 1943-1945 when his work typically demonstrated a fractal dimension, D_f, ranging from to 1.1 – 1.3; the transient years which lasted from 1946-1948, D_f = 1.4 – 1.6; and the later years, 1947-1953, the period when Pollock perfected his technique, D_f = 1.7 – 1.9. It is not so much the mystery of Pollock's style that inspires our work, but the analysis of fractal patterns and their dimension as found in the fluid dynamics of the watercolor medium. Fluid motion has fascinated artist for centuries, for example waves as depicted in Chinese art, The Great Wave by Japanese artist Hokusai, or the hand drawings of water flowing, eddies, and turbulence by Leonardo da Vinci. Interest in the mechanics of turbulent flow has led to the analyses of Vincent van Gogh's most impassioned works such as "The Starry Night" or "Road with Cypress Tree and Star" which remarkably illustrate turbulence. There exists a similarity that has been observed in Jupiter's massive red spot and cosmic dust clouds to van Gogh's unique brush strokes and stunning use of color to capture luminance. Russian mathematician Andrey Kolmogorov proposed that energy in a turbulent fluid at length *R* varies proportionally to the five-thirds power of *R*, and experiments have shown Kolmogorov's formula to be fairly close to the way turbulent flow works. Turbulent flow, in 3 dimensions, is self-similar if there is an energy cascade, *i.e.* big eddies transfer their energy to smaller eddies at smaller and smaller scales [2,3,29]. More recent models have been proposed in the last several years to describe turbulent flow with the use of multifractals. Although this is beyond the scope of our

current work, it is nonetheless extraordinary that art, in its many forms, is inextricably linked to mathematics, presents insight into scientific understanding, and may offer further breakthroughs into other unsolved problems in mathematics and physics.

Figure 2. "Stars with Gas Clouds", watercolor on Arches 140 LB rough paper, 22" x 30", David Baron 2009.

The inspiration for this painting came after viewing images taken by the Hubble space probe. Two prior attempts to paint this subject were made before this "success". The long, vertically oriented strokes of Prussian blue and cadmium yellow disperse and blend into subtle areas of green, simply by mixing together with no other outside forces acting on that

specific area. Alizarin crimson pigment, along with areas of the paper intentionally left white, meander their way through the Prussian blue vastness to create not just orange patches, but the feeling of motion. Patches of stark white paper give the impression of reflected and refracted light from distant stars.

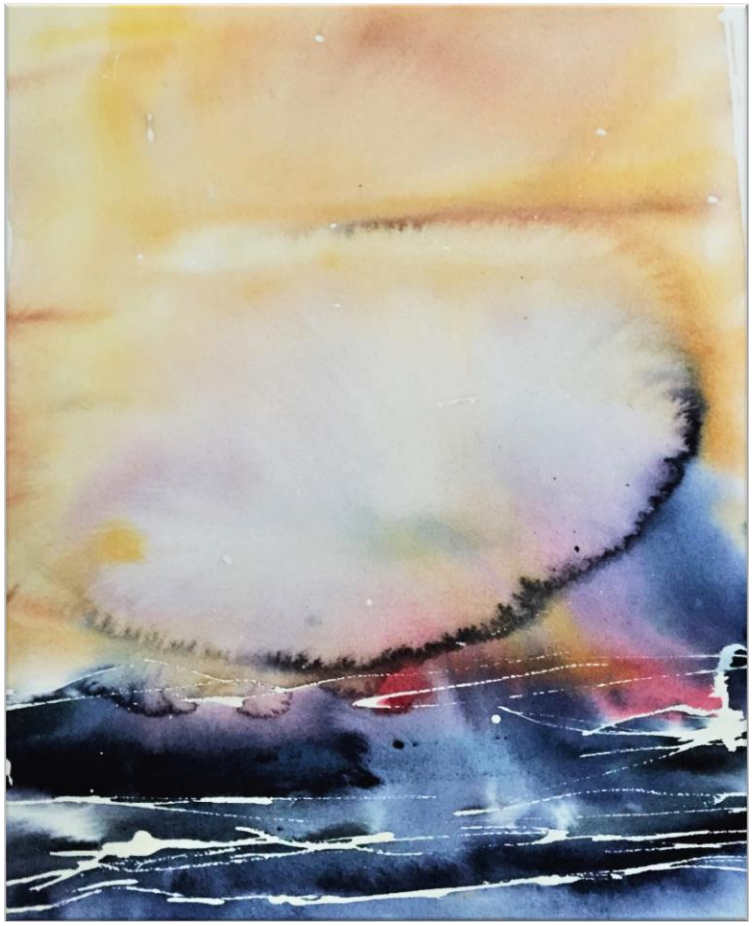

Figure 3. "Orange Skies Over Crashing Waves", watercolor on Arches 140 LB rough paper, 11" x 15", David Baron 2007.

This painting was intended to be a city landscape under an orange sky. Because the painting was left unattended for 2 hours, the different sections of the painting mixed over that time, and left a picture that looks like the crest of a giant wave, which became the most

striking area of the work. The biggest area of sediment deposit bears a resemblance to the Koch snowflake.

Figure 4. "Grey Field Under A Moody Sky", watercolor on Arches 140 LB rough paper, 22" x 30", David Baron 2009.

A brush was first used to apply paint in Rothko-esque fields of color. Loading up the same brush with clean water and dragging the water along the paper cuts the pigments to create not only the sense that clouds are moving through the sky, but the fingering phenomenon in the foreground suggests vertical activity, such as wheat field growth.

Figure 5. Watercolor paint drop experiment - permanent rose, 90 LB Canson paper, 6”x4”; $D_f = 1.5104$. David Baron June 10, 2015.

Chapter 2: Experimental Outline and Results

Section 2.1 Experiment Set-Up

This experiment was conducted utilizing three types of Winsor & Newton Artist Series watercolor paint, namely, permanent rose, Prussian blue, and sepia. These pigments were chosen based upon their individual and significantly differing viscosities and chemical compositions. Each color was available in tube form. Approximately 5 mL of pigment was squeezed from the tube and dissolved in roughly 30 mL of clean, filtered water. Three grades of acid-free watercolor paper were used – Arches 140 LB rough, Arches 140 LB cold pressed, and Canson 90 LB paper. The papers were cut into smaller pieces measuring about 5"x7" and liquid frisket was applied with a knife around the edges of each rectangular paper to create a thin latex border in order to reduce and contain water dispersion. Filtered water was then applied with a soft sea sponge to both sides of the paper, a technique known as wet-on-wet, and the paper (or substrate or canvas) was mounted flat on a backing board. Excess water was spilled off and the paper let sit for a couple of minutes to allow the substrate to thoroughly absorb the water. The papers were then separated into three categories – unfrozen, frozen for 5 minutes, or frozen for 30 minutes. A droplet of paint was released onto a substrate from a height of either 6 inches or 12 inches. For the first set of paintings, the droplet was released from a standard drinking straw by holding the thumb over the top, open end, removing the thumb and letting gravity pull down the pigment. For the remaining sets of paintings, a medicine dropper (of outer diameter 4mm and inner nozzle diameter 1mm) was used to release the droplets. Photographs were taken with a cellular phone camera at roughly 1-minute intervals for about 20-30 minutes or until the paint spread had reached a maximum dispersion. We used the iPhone 6 which has a

resolution 750 x 1334 pixel display and a 29-mm lens which is as effective as a 35-mm camera. Our choice to use the iPhone was based not only on its sufficient capabilities and excellent resolution for its camera, but also for ease of storing and transferring data, roughly 750 photos. Each digital photograph was uploaded onto computer and analyzed using ImageJ software (National Institute of Health, Bethesda, MD, USA). The greatest distance covering each splash was measured by first calibrating the measuring tool of ImageJ which would convert pixels into centimeters, thereby yielding the effective radius (R_{eff}) for each droplet and repeatedly measured at each time interval in minutes.

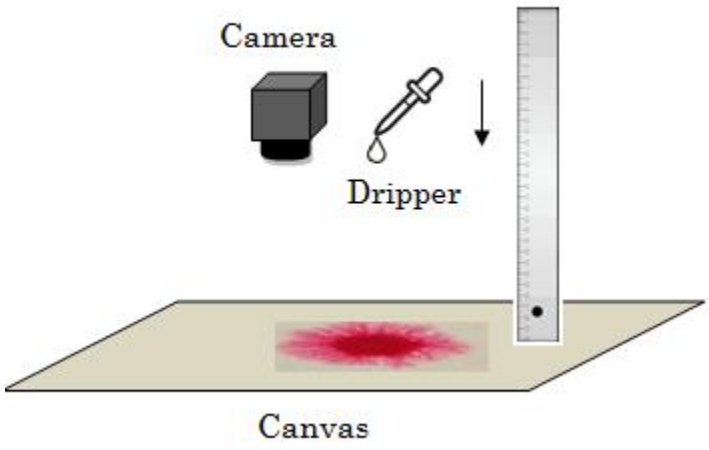

Figure 6. Experimental set-up.

The volume of each droplet released from the medicine dropper was, on average, about 0.04 mL, while the volume released from the straw was about 0.18 mL. The density, ρ, of the droplets of the different paints was measured by weighing 10 mL of the solutions and the volume of each droplet was measured by counting the number of drops that made up 10 mL. The density of the paints ranged between 0.99-1.02 gm/cc. The viscosities of

the paints, μ, were measured using a hand held Haake viscometer (Thermo Scientific, Waltham, MA, USA). The surface tensions of the watercolor paints, σ, could not be measured and were therefore assumed to be the same as that of water, 72 millinewtons per meter at 25 degrees Celsius. The impact velocity of the droplet from the two different heights was computed using the elementary kinematic formula, $V_h = \sqrt{2gh}$, where $V_h$refers to the terminal, impact velocity of the droplet, released from height h. We find that $V_{6in} = 1.73\ m/s$ and $V_{12in} = 2.45\ m/s$. Using these parameters, we can estimate the values of the non-dimensional Weber number and Reynolds number which are given by

$$We = \frac{\rho D V_h^2}{\sigma}, \text{ and } Re = \frac{\rho D V_h}{\mu}$$

where D refers to the characteristic length in the problem which was taken to be the approximate diameter of the droplet. In this study, the Weber number ranged between $150 - 323$, while the Reynolds number varied from $2{,}600 - 10{,}200$. Comparing with the Re vs. We curve we note that our experimental conditions put us in a very interesting part of the phase map which is between the viscous-inertial and capillary-inertial spreading regimes.

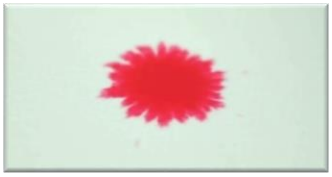

Figure 7. Camera image of permanent rose paint drop at impact. Fingers are beginning to spread.

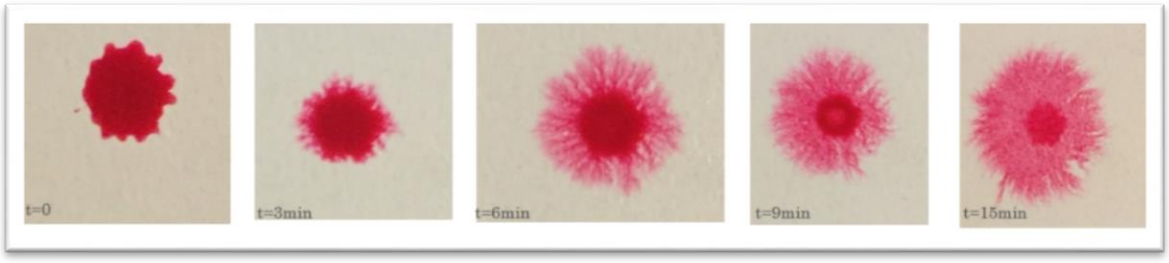

Figure 8. A time sequence of the spreading drop of permanent rose on frozen Arches 140 LB cold-pressed paper.

Section 2.2 Materials

Rheology of paint: The rheological properties of the materials used for painting are each important in their respective ways and interact differently with the other agents involved in the process of painting [16]. Overall, we need to pay particular attention to the following: (1) the support in these experiments: namely the watercolor paper; (2) the ground: the first layer on the support, *i.e.* the water applied to the paper; (3) the paint: one or more pigments, and sometimes a brightener, transparent or "white" that lighten the value and increase the chroma of the dried paint dispersed in a vehicle or medium. The paint consists of: a binder, traditionally and still commonly said to be gum Arabic or glycerin used for softening the dried gum and helping it re-dissolve. The paint also contains humectant, which is made of syrup, honey or corn syrup, to aid in moisture retention; an extender or filler, such as dextrin, to thicken the paint; additives, to prevent clumping of the raw pigment after manufacture and to speed up the milling of the pigment; fungicides or preservatives to suppress the growth of mold or bacteria; and finally, water, which dissolves all the ingredients, transports them onto the paper and evaporates quickly [19].

A sheet of paper is most commonly composed of tangled cellulose fibers. Cellulose is extracted from wood pulp by chemical and physical methods by successive cutting, grinding, soaking, and screening of woodchips or sawdust, which is then bleached in a sulfite or peroxide solution. The resulting mash of pulp is chemically neutralized by adding sufficient amount of base, such as calcium carbonate, to create paper that is usually labelled pH neutral. By contrast, the designation acid free usually means the paper was made by using cotton or linen and that the pulp was not chemically bleached during the manufacturing process. Most commercial art papers are manufactured by machine by injecting the pulp onto a running wire mesh, or between two meshes. The water is drained from the mesh; the wet sheet is fastened between two felts and finally dried. The finished sheet is extruded in a continuous roll or web, and the web is torn or cut into sheets. Mold-made papers are produced with a cylinder mold machine. The pulp is poured over wire mesh cylinders operating at very low speed. The pulp adheres to the cylinders in a continuous thin sheet. This web is pressed into a belt of wet felt, which lifts the web of paper away from the screen. A second felt is placed on top of the sheet and this sandwich is passed through a series of rollers that extrude the water and dry the sheet with forced air. Finally, the bare sheet is run through a stack of heavy iron rollers that refine the surface texture. Methods of drying vary, *e.g.*, by being placed between heated cylinders or by the gentle air flow of loft drying. The different methods affect both the surface texture of the paper, and its stability, *i.e.*, its resistance to buckling when wet. Watercolor papers are supplied in three types of finish or surface texture: rough, cold pressed, or hot pressed. Rough watercolor papers are dried as they are removed from the mold. The pebbly rough texture results from the shrinking of the paper around the natural irregularities in the pulp.

For this reason, the texture becomes rougher. Rough sheets are usually more absorbent and often expand and buckle more than other types of finishes when wet. Cold pressed paper is made by hanging the sheets to loft dry in clusters or by applying light pressure during the felt covered rolling process. The sheets are more stable when wet and usually less absorbent than rough sheets. Hot pressed sheets are manufactured at high pressure between highly polished cold metal rollers, which creates a smooth, polished finish. The surface and fiber density resist paint absorption so more paint stays on the surface [36].

The pigments within the paints used for this experiment are indicated as follows: permanent rose: quinacridone red (PV19), Prussian blue: alkali ferriferrocyanide (PB27), and sepia: carbon black and iron oxide (PBk6, PR101). Experiments were conducted using approximately 5 mL of pigment dissolved in 30 mL of water. Accordingly, the materials were scaled up to 20 mL of pigment dissolved in 120 mL of water for viscosity measurement purposes. The viscometer was first calibrated to zero deciPascal·seconds ($dPa \cdot s$) for clean, filtered water, and then the viscosity of each paint type was measured at 15 second intervals for 10 minutes. An average value for each paint was calculated, along with one standard deviation. The Table 1 lists the average viscosity of the various paints used.

Table 1. Average viscosity measurements of the watercolor paints.

Viscosity	Permanent Rose	Prussian Blue	Sepia
Average Viscosity (dPa·s)	0.0257	0.0132	0.0098
Standard Deviation	0.0085	0.008	0.0071

The non-Newtonian characteristics of watercolor paint are not presented in this study. However, there is reason to believe that paints could be non-Newtonian based on their various components, as mentioned above. Such a multi component suspension has the tendency to display properties such as yield, thixotropy or dilatancy, which are fundamental non-Newtonian characteristics and extend important properties for painting purposes. It has long been thought that the low viscosity of the carrier fluid (water) would render the watercolor system Newtonian, but recent work has shown that components such as gum Arabic possess non-Newtonian properties when in solution. The effect of freezing temperatures upon paint and surface roughness could also potentially bring out non-Newtonian properties. These are, however, not rigorously proven at this stage and need to be investigated in greater detail in the future.

Heating Curves for Canvas: The canvas was wetted on both sides according to the procedure described earlier and placed in a freezer for a duration of 5 and 30 minutes, corresponding to the two cases of frozen paper. The freezing times were chosen under the assumption that freezing longer would allow us to maintain the surface as a solid for a longer period. The time interval between the removal of the melting of the canvas from the freezer and the start of the experiment was about 10-15 seconds. Therefore, no significant effects would have occurred in this time. To verify how the temperature of the

canvas changed with time, we measured the average surface temperature on the canvas in all three cases using an infrared thermometer (General IRT 206 Infrared Thermometer, Taiwan.) The Figure 9 shows the "heating curves" for all three cases which reveals the Classical Newtonian profile. After approximately 10 minutes, the temperature of all three canvases reach a common temperature and very slowly converge to room temperature. The melting temperature for the two frozen canvases are approximately at the 1min and 4 min mark indicated by the dashed lines in the Figure 9. Prolonged residence times in the frozen state results in reduced viscous resistance for the paint to disperse on the canvas.

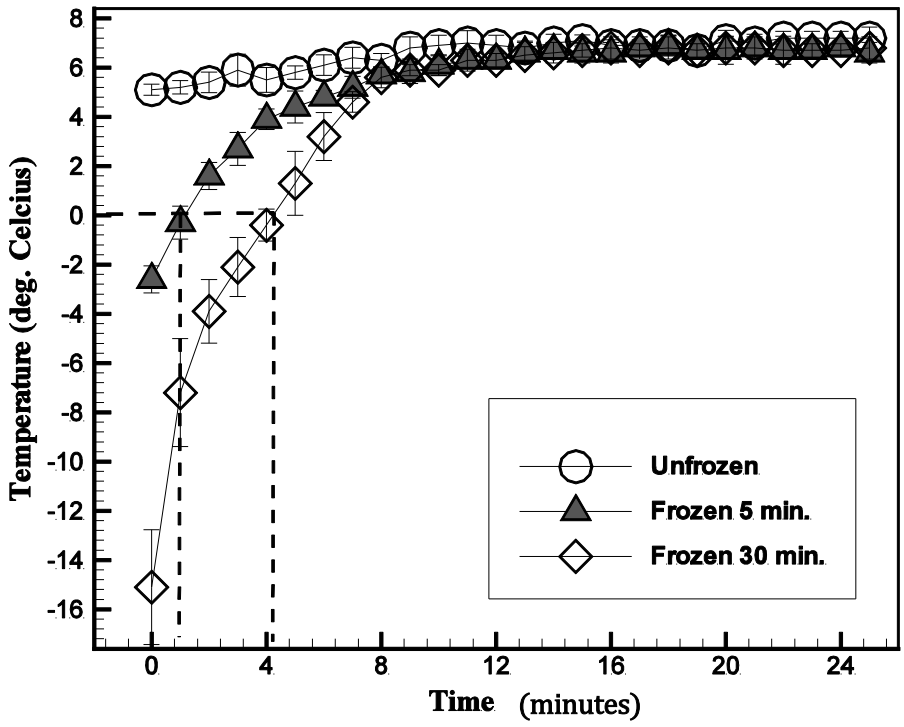

Figure 9. Temperature of the canvas as a function of time for all three cases. The dashed lines point to the times when the canvas surface appears to be in molten liquid state.

Porosity of Canvas: The porosity of the canvas was analyzed using the standard water evaporation method [23]. The pore volume fraction is given by $\varepsilon = \frac{V_p}{V_t}$, where V_t is the total volume and V_p is the volume of pores of the form:

$$V_p = \frac{weight\ of\ wetted\ canvas - weight\ of\ dry\ canvas}{density\ of\ water}.$$

Our estimations of the porosity of the three of the three different canvas types reveal that the void fractions for 90 LB, 140 LB, and 140 LB cold-pressed are $0.489, 0.319$, and 0.290, respectively suggesting 30% to nearly 50% of the canvas being empty space. Figure 10a-c show the canvas under a microscope with the last one, Figure 10d showing a regular, uncoated printer paper under the same magnification for comparison. All the surfaces have been stained with watercolor paint to highlight surface features. The images reveal substantial coarseness of the surfaces, especially in cases in cases (a)-(c), when compared to plain paper and the porous nature of the canvas, even at such relatively low levels of magnification.

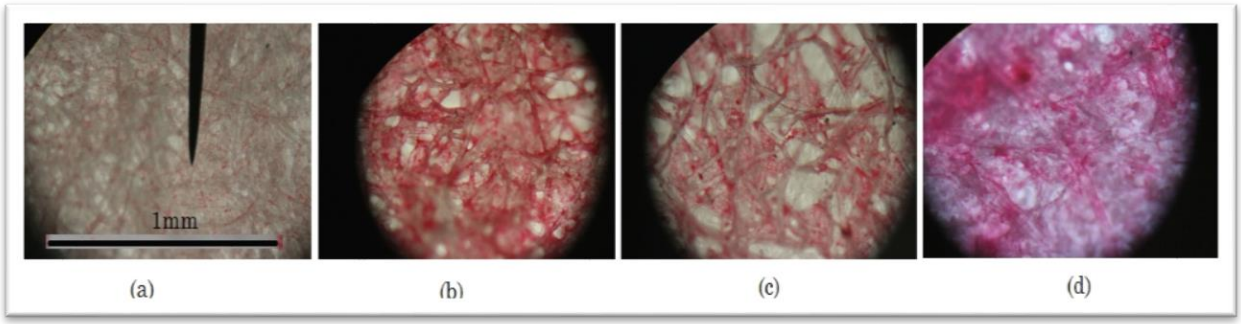

Figure 10. Closeup view of the three canvases used in this study showing their surface features and porous nature. The pictures were taken with a Leica CME microscope at magnification of 100x. Images (a)-(c) correspond to 90 LB, 140 LB, and 140 LB cold-pressed canvas, respectively. The image (d) is of stained, uncoated printing paper at the same magnification.

Section 2.3 Results

The greatest distance covering each splash was measured in centimeters, thereby yielding the effective radius (R_{eff}) for each droplet, and repeatedly measured at each time interval in minutes (see Figure 13b). The final, dry image was measured with a ruler to find the true distance of the effective radius. Each ImageJ-generated R_{eff} was then adjusted using a scaling factor. Graphs plotting R_{eff} vs. Time were generated using Microsoft Excel for each individual trial, as well as for displays to compare each parameter, *i.e.* paint viscosity, paint volume, paper roughness, paper temperature, and height of droplet. The data was then analyzed to look for statistical correlation among height, temperature, paint viscosity, and paper type on (a) the final radius of the splash, (b) splash pattern, and (c) fractal dimension.

The effective diameter of each splash was measured in centimeters, approximated by the largest width of the splash. The effective radius of each droplet was repeatedly measured using ImageJ at time intervals on the order of 15 seconds to 1 minute from the time of impact until the time of equilibrium state, when the paint eventually dried on the paper, on average 15 to 20 minutes. Figure 11 depicts the evolution of the effective radius of the splash as a function of time. In particular, the figure shows a representative image of the impact of: height of droplet, temperature of the canvas, surface roughness of the canvas, and the viscosity of the paints upon this saturating curve. One can clearly see the impact of some of these parameters more strongly than others from the figures. The effective radius of the paint is most affected by the paint type and nature of canvas (Figure 11c, d) which can be attributed to the varying frictional forces caused by the different pigment concentration of the paints and surface roughness of the canvas, respectively. The

temperature of the canvas (Figure 11b) also shows interesting trends in the initial phase when surface characteristics are different. However, the true impact of all the parameters can be procured only by means of some more rigorous statistical means. Statistical analyses were conducted for the 46 different cases that were studied and correlations between the size of the splash and the various control parameters are best determined using these tools. The statistical correlations are discussed below in Section 5, but, in the rest of this section, we discuss some other specific quantitative features, drawing upon similar work in the literature on slightly different systems.

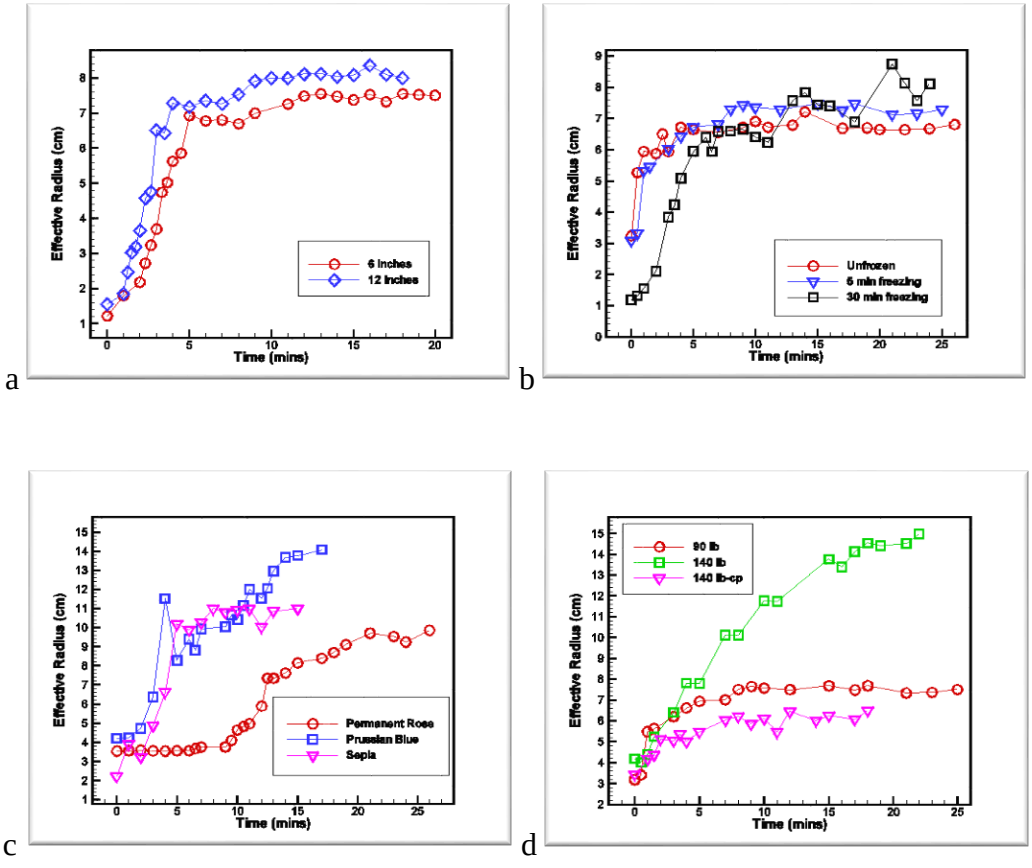

Figure 11. The effective radius of the splash as a function of time showing the effect of (a) height of droplet; (b) the temperature of the canvas; (c) the viscosity of the paint; and (d) the type of canvas used.

We made a qualitative analysis of our paint drop experiments, as in [24]. We only observed two broad categories of splashing, namely deposition and prompt splashing due to the rapid absorption of much of the paint into the canvas upon contact. Within these categories: (i) symmetric or circular patterns; (ii) splash pattern with a visible inner stamp; (iii) splash with strong radial fingering patterns; and (iv) satellite droplets. In Table 2 below, we explain the qualitative impact of the experimental parameters upon the appearance and strength of the splash patterns which are also shown in Figure 12. This is also further investigated in our statistical analysis section. In the table ↑ indicates that the control parameter has an increasing effect upon the strength/magnitude/existence of that particular pattern while the symbol ↓ indicates the reverse.

Table 2. Repeated patterns observed in our experiments are analyzed for their qualitative dependence upon canvas roughness, paint viscosity, height (or impact speed), and temperature of canvas.

	Symmetric/Circular	Visible Inner Stamp	Radial Fingering	Satellites
Increase in…				
Height	↓	–	↑	↑
Paper Roughness	↓	↓	↓	
Paint Viscosity	–	↑	↓	–
Freezing	↑	↑	–	–

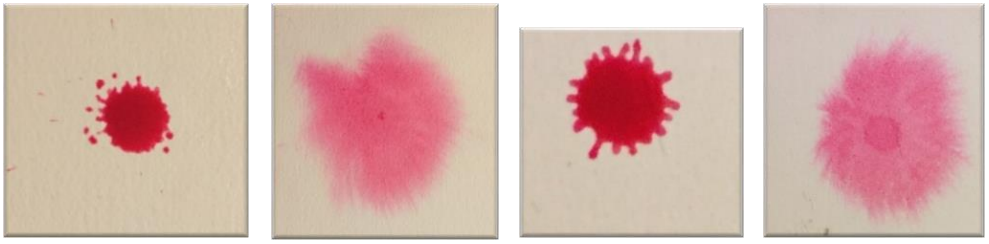

(A1) (A2) (B1) (B2)

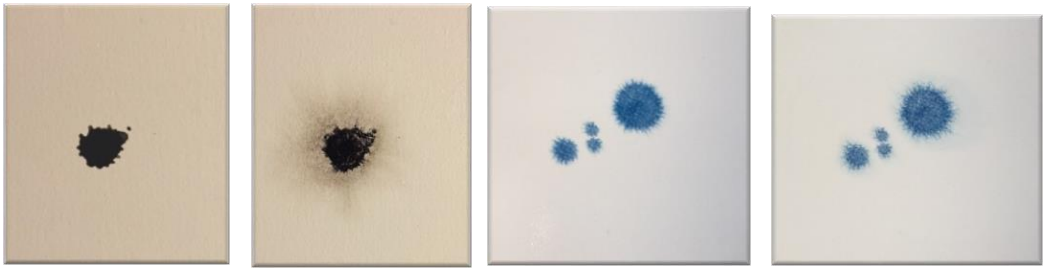

(C1) (C2) (D1) (D2)

Figure 12. Examples of the four distinct splash patterns seen in our experiments. A single splash can contain one or more of these patterns. The images are organized in pairs, with the first image (X1, where X = A, B, C, D), immediately upon impact and the final image (X2) are the images at the final times, at equilibrium.

Rioboo *et al*. [25] break down the deposition of paint on a dry surface into two phases: kinetic and actual, with the former displaying a radial growth $r \sim \sqrt{t}$, where r is the effective radius of the splash and t, is time. Such a profile is also observed in other studies concerning droplet splashes on liquid surfaces [26]. However, the value of the exponent is seen to vary in some other studies between $0.2 - 0.5$ [27,28] which is attributed to the interaction of adjacent splashes. In our experiments, we also fit a power law function $r \sim at^b$, to verify the radial growth rate of the splashes (see Figure 13). On average, over all the experiments performed, the average values of the fit parameters

are $\bar{a} = 4.39$ and $\bar{b} = 0.26$, with an average fit correlation $R^2 = 0.86$. However, if the data is analyzed in terms of the freezing period of the canvas, we observe a distinctly different value of $\bar{b}$; (i) in the case when the canvas is not frozen, $\bar{b} = 0.091$, (ii) when the canvas is frozen for 5 minutes, $\bar{b} = 0.194$, and when the canvas is frozen for 30 minutes, $\bar{b} = 0.471$. in the current study, we therefore hypothesize the existence of three phases: (i) initial absorption, (ii) kinetic, and (iii) actual. The initial absorption phase, which does not exist in previous experiments, could potentially leave a relatively smaller volume of the droplet to spread. This would suggest a short kinetic phase which is dominated by capillary forces resulting in a slower growth rate. The relatively low value of our own exponent can be attributed to such an initial absorption phase.

a 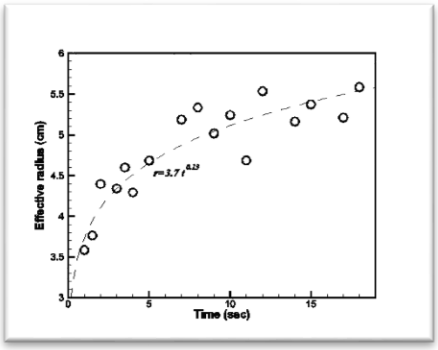

b 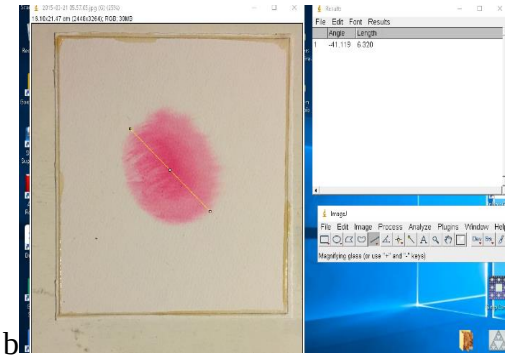

Figure 13a, b. The graph shows the evolution of the effective radius of the splash with time. A power law fit to the data is also shown, with an exponent value of 0.13, which is smaller than those seen in other kinds of splashes. Figure 13 b. An example of how measurements were made using ImageJ.

Following the work of Marmanis and Thoroddsen [24], we estimate the *"number of fingers"* as a function of height for various cases that show clear fingering patterns. As in [24], *"…everything that resembles a finger, no matter how short…"*is regarded as a finger. The exact number of fingers however, is difficult to determine and the numbers

reported must be realized to be approximate. Figure 14 depicts some sample cases of our analysis which shows the count for the two different heights considered in this study ($h = 6\ in$ and $h = 12\ in$) and two different paints (permanent rose and Prussian blue). Clearly, in both cases, the height, or impact velocity is directly related to the number of fingers (also noted in [24]). In addition, the viscosity of the paint is inversely related to the number of fingers seen from comparing the two graphs Figure 14a, b. Other potential factors are more difficult to identify directly from the count and are dealt with in the following section 5.

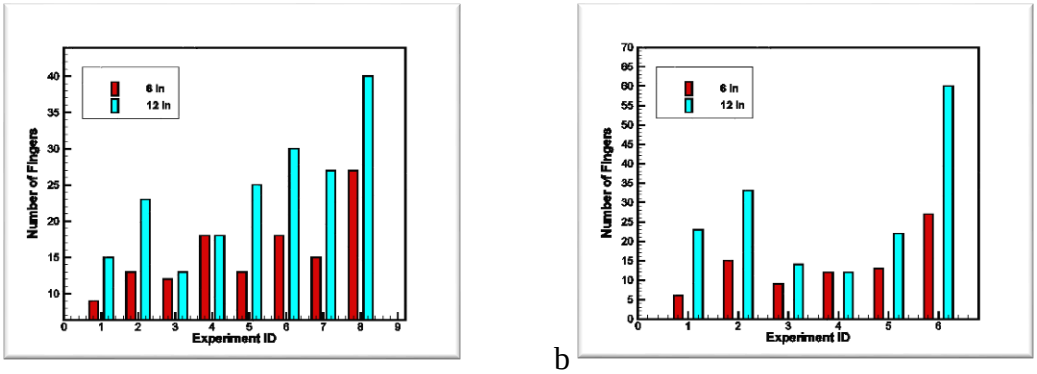

a b

Figure 14. Number of fingers as a function of release or impact velocity, dependent on height of release, 6 inches versus 12 inches. Figure (a) shows the results for permanent rose and figure (b) shows the count for Prussian blue. The x-axis represents different experimental cases where fingering was observed.

Section 2.4 Fractal Dimension

The fractal analysis of drip paintings has become a research area of widespread interest in the past two decades [2,3,29]. The "organic" paintings of Jackson Pollock, in particular, have been identified as having a unique fractal signature. As a result, Taylor

et al. [29] have claimed that the fractal dimension can be used as a means to identify artists and expose fakes, a claim which is contested by some [30]. However, this controversial issue aside, the fractal dimension analysis of art is an interesting issue in itself. Furthermore, fractal patterns have also found unique and interesting application in fields such as environmental psychology, or for therapeutic purposes (see [31] and references therein).

The method of box counting was implemented to approximate the fractal dimension of each painting. To estimate a two-dimensional fractal, a grid of boxes, each with a horizontal and vertical dimension of $2^n, \{n = 0,1,2, \dots, m\}$, is superimposed over an image and the total number of boxes, N_m, that are needed to cover the image are counted. At any given value of m, the fractal dimension, or Hausdorff dimension, is then approximated by $D_m = \frac{\log(N_{m)}}{\log(2^{m)}}$. This procedure is repeated as $m \rightarrow \infty$, thus $D_m \rightarrow D$, the dimension of the figure. A MATLAB based code was used to perform this computation. Test images with known fractal dimension were used to determine the accuracy of the MATLAB code. A numerical analysis of fractal dimension versus number of boxes graphically demonstrates an ideal box count around 200-400. At box count numbers, greater than 400, the fractal dimension diverges from the target value because the number of boxes covering the image, N_m, becomes negligible in comparison to the total number of boxes, 2^m, just as an object under a microscope might become blurry even though the lens gets closer and closer to a specimen on a slide. Consequently, a limit must be imposed on m to prevent $N_m$from becoming infinitesimally small and 2^minfinitely large so as to yield a value equal to zero, and thus an indeterminate logarithmic ratio. Test images with known fractal dimension were used to determine the accuracy of the MATLAB code. A numerical analysis of fractal

dimension versus number of boxes graphically demonstrates an ideal box count around 200-400.

a 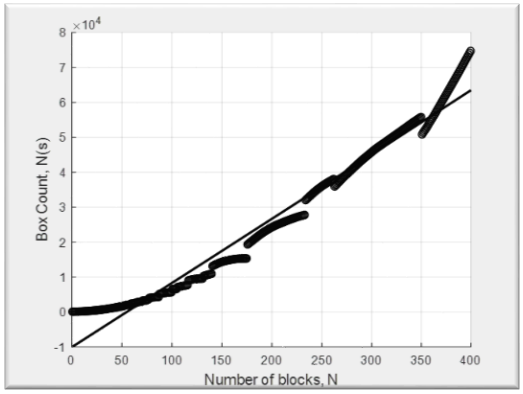

b 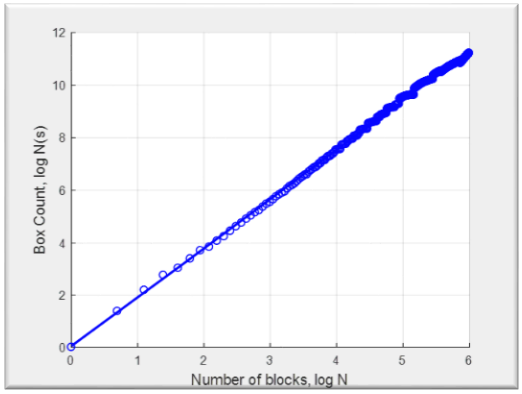

Figure 15a, b. Limit for the numerical approximation of Hausdorff dimension of a typical image. The box bount is method used in 15a keeps a count to compute the ratio of the boxes that cover the image being analyzed to the total number of boxes. The limit of the logarithmic ratio of those two values indicates the fractal dimension as shown in 15b.

The photographs were saved in 'JPG' format, loaded into MATLAB which converted a color image into a binary data array to produce a black and white figure (see Figure 16) which could then be analyzed with the box count method. Benchmark tests for the fractal dimension were performed (see Table 3) on several well-known patterns such as Sierpinski triangle, Koch snowflake, and Apollonian gasket, (see figure 16) [32]. Convergence studies were also conducted for box counts ranging from 25-500. Maximum error in our fractal dimension computation was about 0.09% when compared with their known dimensions.

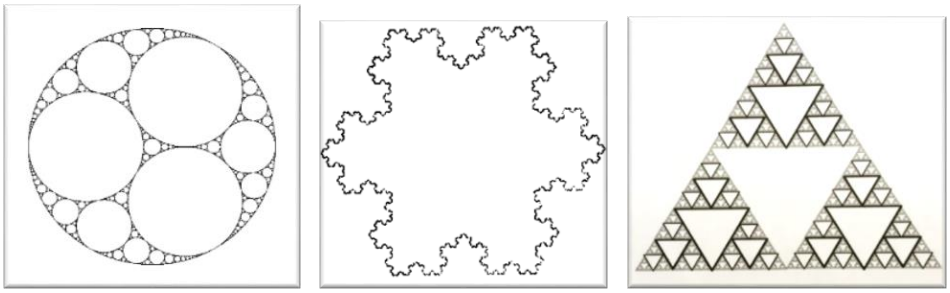

Figure 16a, b, c. Apollonian Gasket, $D_f = 1.3057$; Koch Snowflake,$D_f = 1.26$; Sierpinski Triangle, $D_f = 1.5849$. Some of our bench mark fractals used in convergence studies to test the box count code's accuracy.

Figure 17. Black and white images of 3 different splashes. We are looking for patterns of self-similarity, i.e. fractals.

Table 3. Fractal dimension of some sample cases.

Cases	Permanent Rose	Prussian Blue	Sepia
Unfrozen (6in)	1.637	1.832	1.826
Frozen 30 min (6in)	1.975	1.570	1.707
Unfrozen (12in)	1.822	1.820	1.738
Frozen 30 min (12in)	1.931	1.722	1.650

The time evolution of the fractal dimension was also computed and shows a similar overall profile to the effective radius. Figure 18 shows a sample curve corresponding to the images in Figure 8. However, this curve does not display a power-law correlation. The factors affecting the fractal dimension are discussed in the following section.

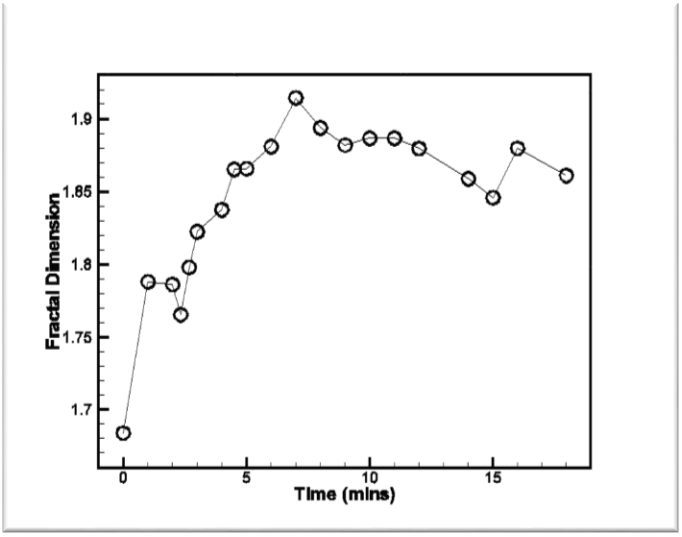

Figure 18. Time evolution of fractal dimension of a splash.

Section 2.5 Statistical Analysis

We first modeled the relationship between scaled radius and the predictor variables: temperature (1 = unfrozen, 2 = frozen 5 min, 3 = frozen 30 min), height (1 = 6” and 2 = 12”), time, viscosity (1 = permanent rose, 2 = Prussian blue, 3 = sepia), type of paper (1 = Canson 90 LB, 2 = Arches 140 LB rough, 3 = Arches 140 LB cold-pressed), and the volume (1 = medicine dropper, 2 = straw), where time is the only continuous variable and all the others are treated as categorical variables. The fitted model result is given in Table 4. Further ANOVA analysis showed that all the predictors are significant predictors to the scaled radius. Based on Table 4, we can see that frozen 30 minutes significantly decreases the scaled radius compared to the unfrozen temperature (p-value = 0), but frozen 5 minutes is not significantly different from unfrozen temperature. Height at 12” significantly increases the scaled radius compared to height at 6”. With time increasing, it significantly increases the scaled radius. The normality and constant assumption of this multiple regression are met through residual plot check.

We modeled how the same set of covariates affect certain specific parameters (termed hole pattern 1 and hole pattern 2, see Figure 23 for comparison). We created a binary variable for hole pattern 1 which corresponds to a prominent initial droplet stamp where paint has landed and dispersed, such as in Figure 12(B2). We fitted a logistic regression model using the covariates to explain the binary response variable hole pattern 1. The fitted model is given in Table 5. Height, time, paper type, and volume are significant predictors to the binary response hole pattern 1. Specifically, height at 12”

increases the odds of hole pattern 1; longer time increases the odds of hole pattern 1; using paper type 2 has higher odds of hole pattern 1 than using paper type 1; and volume 2 has lower odds of hole pattern 1 than volume 1.

We fitted a similar logistic model with response variable hole pattern 2 (rheological settling paint pattern within boundary of initial droplet with no interior stamp, for example Figure 12(A2)). The fitted model is given in Table 6. The result indicates that all predictors are significant except for height. Frozen for 30 minutes has higher odds of hole pattern 2 than unfrozen. However, frozen for 5 minutes has no significant difference from unfrozen. Longer time increases the odds of hole pattern 2. Prussian blue and sepia both have significant higher odds of hole pattern 2 than permanent rose, sepia has the highest odds of hole pattern 2 compared to the other two viscosity levels. Canson 90 LB paper has the higher odds of hole pattern 2 than Arches 140LB rough and Arches 140 LB cold-pressed. Volume 2 (straw), as seen in Figure 21, has higher odds of hole pattern 2 than volume 1 (medicine dropper).

We then fit the fractal dimension with all the predictors. For each experiment, we recorded the last fractal dimension value. In total, there were 46 observed fractal dimension values. We fit a multiple regression model but found two outliers from the residual plot and normal Q-Q plot. We removed the two outliers and refit the model. The final result is given in Table 7. The result indicates temperature frozen at 30 minutes significantly reduces the fractal dimension value compared to unfrozen. Prussian blue and sepia significantly reduce the fractal dimension value compared to permanent rose. The residual against the fitted plot (see Figure 19a) and the normal Q-Q plot (see Figure 19b) indicate that the model assumptions are met and the inference obtained from this model are valid.

a 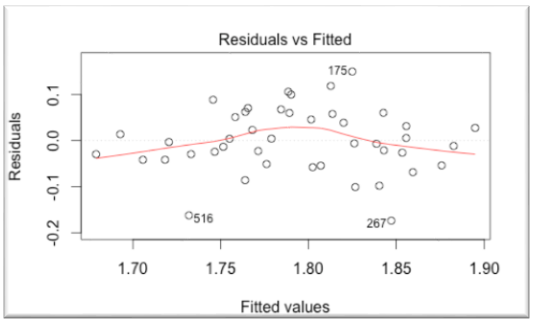

b 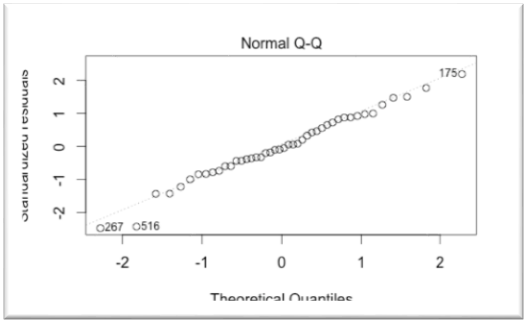

Figure 19a. Residual against fitted value plot for multiple regression model of fractal dimension. 19b. Normal Q-Q plot for multiple regression model of fractal dimension.

Tables of Statistical Data

Table 4. Multiple regression model results for scaled radius.

	Estimate	Std. Error	t Value	Pr(>|t|)
(Intercept)	5.5634	0.2156	25.81	0.0000
factor(Temp)2	0.1926	0.1931	1.00	0.3188
factor(Temp)3	–1.8528	0.1841	–10.06	0.0000
factor(Height)2	0.2908	0.1398	2.08	0.0378
Time	0.1579	0.0088	17.89	0.0000
factor(Viscosity)2	–2.3478	0.1580	–14.86	0.0000
factor(Viscosity)3	0.7302	0.2721	2.68	0.0074
factor(Paper)2	0.8153	0.1941	4.20	0.0000
factor(Paper)3	–0.4384	0.2769	–1.58	0.1138
factor(Volume)2	0.5852	0.1895	3.09	0.0021

Table 5. Logistic model results for hole pattern 1.

	Estimate	Std. Error	z Value	Pr(>|z|)
(Intercept)	–26.6447	1457.5012	–0.02	0.9854
factor(Temp)2	20.1488	1457.5009	0.01	0.9890
factor(Temp)3	24.0557	1457.5010	0.02	0.9868
factor(Height)2	1.0877	0.3406	3.19	0.0014
Time	0.3074	0.0365	8.42	0.0000
factor(Viscosity)2	–28.0664	1122.4010	–0.03	0.9801
factor(Viscosity)3	–20.9046	2602.5289	–0.01	0.9936
factor(Paper)2	2.2046	0.4948	4.46	0.0000
factor(Paper)3	0.5124	0.4571	1.12	0.2623
factor(Volume)2	–2.8894	0.5487	–5.27	0.0000

Table 6. Logistic model results for hole pattern 2.

	Estimate	Std. Error	z Value	Pr(>|z|)
(Intercept)	–0.8532	0.2482	–3.44	0.0006
factor(Temp)2	0.0944	0.2309	0.41	0.6827
factor(Temp)3	1.3492	0.2220	6.08	0.0000
factor(Height)2	–0.2046	0.1654	–1.24	0.2161
Time	0.0035	0.0101	0.35	0.7289
factor(Viscosity)2	1.3398	0.1847	7.25	0.0000
factor(Viscosity)3	3.6557	0.5041	7.25	0.0000
factor(Paper)2	–1.2459	0.2277	–5.47	0.0000
factor(Paper)3	–1.2640	0.3389	–3.73	0.0002
factor(Volume)2	0.8644	0.2167	3.99	0.0001

Table 7. Multiple regression model results for fractal dimension.

	Estimate	Std. Error	t Value	Pr(>|t|)
(Intercept)	1.8432	0.0537	34.35	0.0000
factor(Temp)2	–0.0329	0.0297	–1.11	0.2762
factor(Temp)3	–0.0720	0.0303	–2.38	0.0232
factor(Height)2	–0.0126	0.0240	–0.53	0.6027
Time	0.0004	0.0021	0.18	0.8553
factor(Viscosity)2	–0.0582	0.0269	–2.16	0.0377
factor(Viscosity)3	–0.1247	0.0483	–2.58	0.0144
factor(Paper)2	0.0035	0.0414	0.08	0.9338
factor(Paper)3	0.0774	0.0476	1.63	0.1134
factor(Volume)2	0.0359	0.0337	1.06	0.2947

A qualitative analysis of the images that resulted during the "life-span" of our paintings reveal some fascinating results. The similar nature of the branching fingers, shown in Figure 20, to that of blood-carrying capillaries or to the diffusion limited aggregation fractal, (Figure 1e), is quite interesting. This form of the spreading droplet only exists for a couple of minutes after which time the fingers have dispersed and displacement grows with increasing temperature. Before we begin devising our mathematical model, it is worth examining more closely, other transient moments caught on camera. Figure 22 a, b, and c show a near radial symmetry for the entire time-evolution of this particular experiment. A side-by-side comparison of hole patterns 1 and 2 are shown in Figure 23a and b. Figure 24 a and b help explain how and why we refined our experiment with emphasis on Prussian blue and permanent rose. The general results for

sepia paint showed few dissimilarities among the initial, transient, and final images. The difference between initial and final images shown in Figure 25a and b are difficult to discern. The outward spread of mostly carrier fluid may be more obvious to find than the very fine changes that occur along the perimeter of the drop. We use fractal dimension to measure these imperceptible differences. Furthermore, compare Figures 26a and b to see that we cannot be certain at this point if fractal dimension is monotonically increasing or decreasing. These two images appear identical, yet the fractal value increases, exhibiting the opposite behavior as Figure 25a and b. Figures 27 and 28 show the time-evolution for two experiments differing only by the grade of watercolor paper used for the respective experiments. The transient images and the final results are vastly different for these two experiments.

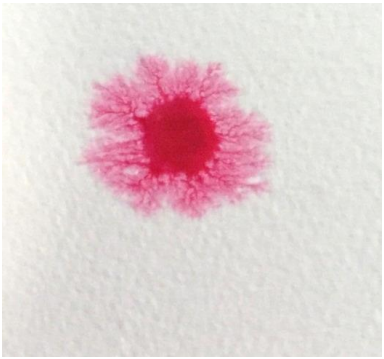

Figure 20. Experiment #5 Melting permanent rose released with a medicine dropper from a height of 6 inches onto Canson 90LB paper, frozen 30 minutes, $t \approx 4\ min$. The branching patterns seen only during the transient stage of this spreading droplet are similar to those found in diffusion limited aggregation.

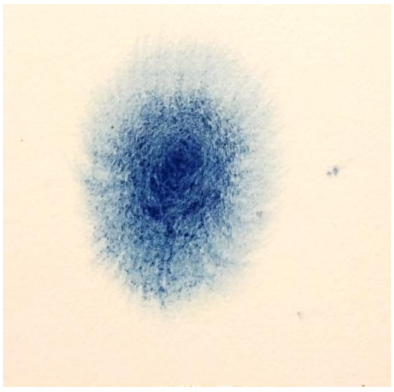

Figure 21. Experiment #34 Prussian blue paint pigment pattern, final dry image, 12 inches, frozen 5 min, Arches 140LB rough, released using a straw, $t_f = 25\ min$. A larger volume of paint droplet results in a larger, final, effective radius. The release height results in satellite splashes (hysteresis), and with that increased surface area covered comes a greater range of possible patterns.

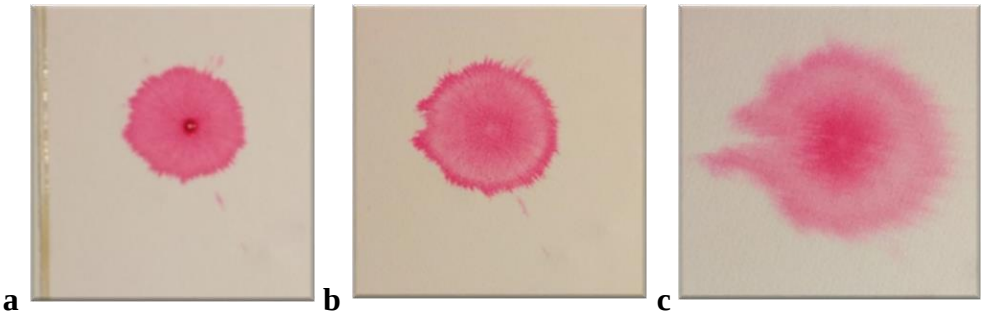

Figure 22a, b, c. Time sequence Exp. #20 permanent rose, 90 LB Canson paper, unfrozen, release height of 12 inches. The entire drop appears to spread out radially more or less uniformly at the early stages (a), the beginning of a non-uniformity on the left side of (b), finally resulting in pattern (c). The time when each image was taken: (a) $t = 0$, (b) $t = 30$ seconds, (c) $t = 4\ min$.

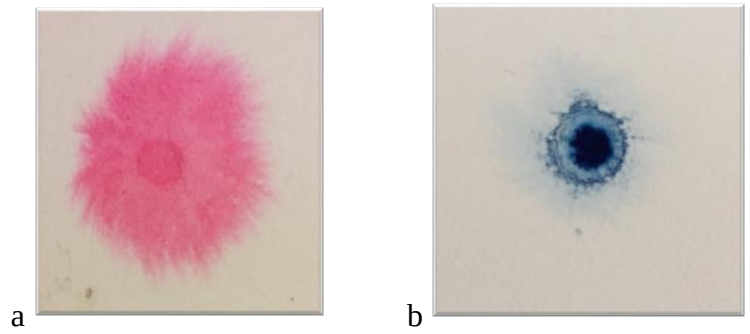

Figure 23a, b. Exp. #6 permanent rose with hole pattern 1, $t_f = 18\ min$; Exp. #23 Prussian blue with hole pattern 2, $t_f = 16\ min$. Figure 23b shows the carrier fluid has spread outward, leaving pigment behind in a region contained within the original radius distance. In 23a, all of the paint has spread outward but left a stamp of the drop's flattened appearance upon impact.

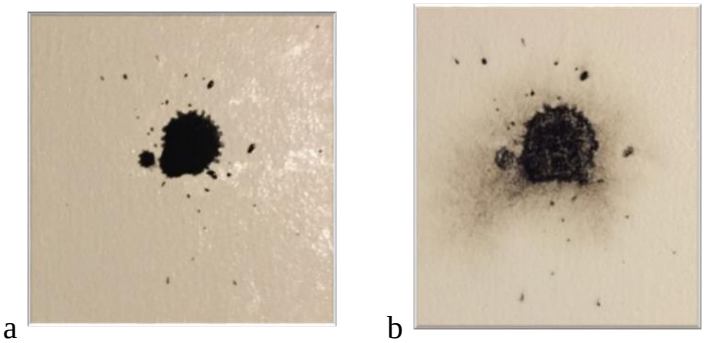

Figure 24a, b. Time sequence Exp. #45 sepia 140 LB Arches rough, frozen 30 minutes, height at 12 inches. Satellites are the result of hysteresis, ejection of particles from the liquid drop. Dry sepia paint pigment sediment residue is visible as very little appears to have dispersed. Sepia paint was experimentally determined to have the lowest viscosity of the paints used. $t_f = 15\ min$.

a 

b 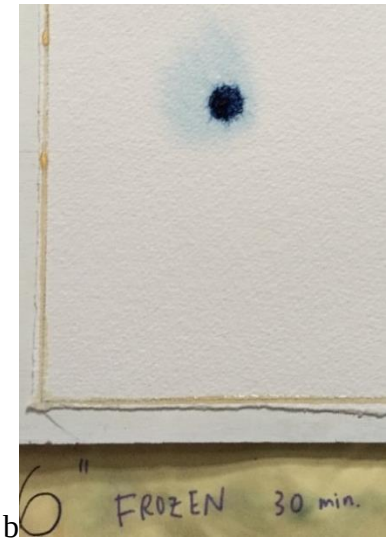

Figure 25a, b. Exp. #27 Prussian blue drop released from height of 6 inches with a medicine dropper spreading on Arches 140 LB rough paper at $t_0, D_f = 1.7285$ and $t_f, D_f = 1.6390$. The carrier fluid has dispersed and the fingers have barely branched out. $t_0 = 0, t_f = 40$ min.

a 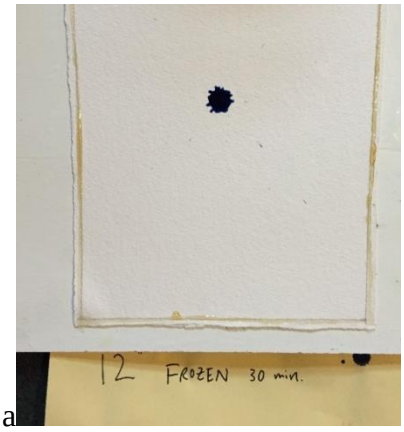

b 

Figure 26a, b. Exp. #36 Prussian blue drop from 12 inches height spreading on Arches 140LB rough paper at $t_0, D_f = 1.4270$ and $t_f, D_f = 1.4550$, almost no noticeable change in the drop. $t_f = 38$ min.

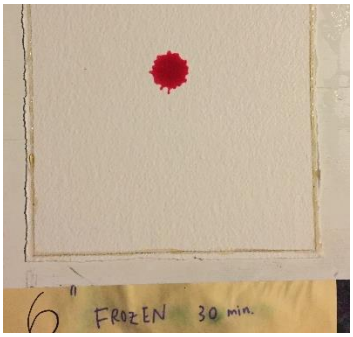

$(a)\ t = 0$

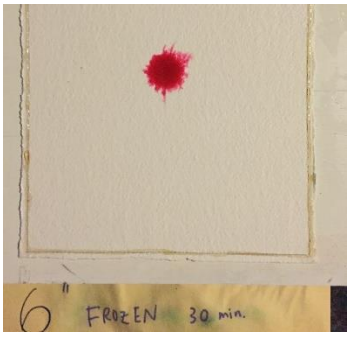

$(b)\ \ t = 7\ min$

$(c)\ t = 10\ min$

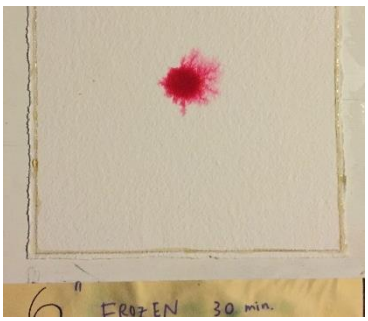

$(d)\ t = 11\ min$

$(e)\ t = 13\ min$

$(f)\ t = 15\ min$

$(g)\ t = 17\ min$

$(h)\ t = 21\ min$

$(i)\ t = 37\ min$

Figure 27a-i. Time sequence for Experiment #19, a droplet of permanent rose paint released from a height of 6 inches, from a straw onto Arches 140 LB rough paper frozen for 30 minutes. Viscous forces compete with inertial forces producing a spectacular show of changing patterns until equilibrium. The end result is a large radial spread, a small amount of pigment left in the center (hole pattern 2), and a very faint trace of the initial stamp (hole pattern 1).

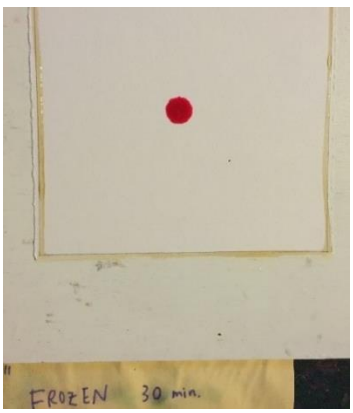

$(a)\ t = 0$

$(b)\ t = 2\ min$

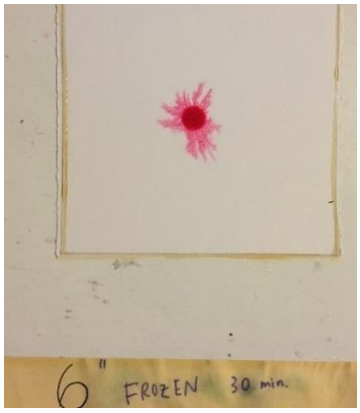

$(c)\ t = 3\ min$

$(d)\ t = 4\ \ min$

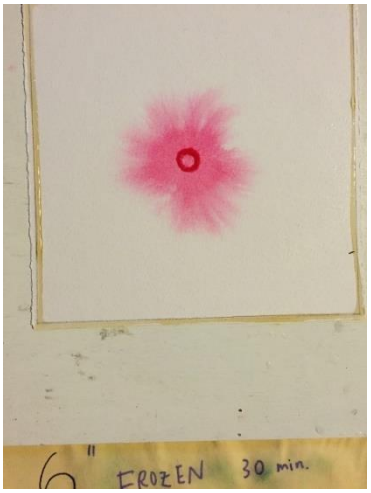

$(e)\ t = 6\ min$

$(f)\ t = 12\ min$

Figure 28a-f. Time sequence for Experiment #5, a droplet of permanent rose paint released from a medicine dropper onto Canson 90 LB paper frozen for 30 minutes after impact from a height of 6 inches. A more porous paper will permit further dispersal of carrier fluid and pigment particles.

Chapter 3: Mathematical Models

3.1 The Basic Model

Introduction

The splash instability is a complex sequence of problems within fluid mechanics. Experimental investigations of the many different regimes have been performed to develop mathematical models to quantify and predict phenomena such as the coronal splash, or the ejecta sheet, or the point at which particle ejection (hysteresis) occurs [8,26,41]. Our model for a slow-spreading watercolor paint drop begins from the moment of impact, after a falling droplet hits a hard, wetted surface, see Figure 7, and continues until the paint drop reaches a maximum dispersal. We ignore hysteresis [14], and begin our model where the finger studies in the literature end [24]. The shape of the drop at impact is assumed to be spherical. This may be a reasonable assumption; however, we must remember that in fact, gravitational forces on each point of the falling drop compete with surface tension forces, simultaneously pulling each point of the drop back inward, holding the liquid drop together. This causes a drop to oscillate between ellipsoidal and spherical forms, as demonstrated in the first schematic diagram, Figure 29. We then assume that the fingers radiate outward from points equally spaced along the circumference of a circular drop, assuming energy dissipation in the y-direction is the same as in the x-direction, hence there is no angular change over time. We ignore the fact that we are dropping paint onto a porous surface, thereby disallowing for absorption into the paper and energy dissipation along the z-direction. We assume that surface tension, defined as the tension of the surface film of a liquid caused by the attraction of the particles in the surface layer by the bulk of the liquid which tends to minimize surface area, will be negligible compared to viscous and inertial

forces. We ignore capillary forces, generally defined as the ability of a liquid to flow in narrow spaces without the assistance of, or even in opposition to gravity, the assumption here being that vertical displacement will be negligible compared to horizontal dispersal. The theoretical, one-dimensional model developed in this paper deals with the simplified spreading regime when inertial forces compete with viscous forces.

From the continuity equation for the conservation of mass, we measure the quantity of flux emanating from any point in a vector field or the rate of loss of mass or heat, $etc.$, often referred to as the divergence in applied terms, using the differential operator short-hand notation. The equation for conservation of momentum is a balance of the forces acting on and in a dynamical fluid system, comprised of inertial, viscous, pressure, and external forces applied to a fluid. This pair of equations form what is referred to as the 3-dimensional Navier-Stokes equations, a set of equations used to mathematically model fluid flow in general. Simplifications of Navier-Stokes can be made, if certain conditions are held. For example, the 2-D Saint-Venant equation is used in systems of equations for shallow water. The 1-D Saint-Venant equation, a simplification of the 2-D problem, is commonly applied to one-directional fluid flow, $e.g.$ open-channel flow or a stream. Assume for now that a drop disperses uniformly in all directions with no lateral energy dissipation. Everything that happens in the x-direction also happens in every other direction. We can simplify a two-dimensional phenomenon into a one-dimensional problem. The Saint-Venant equations for conservation of mass and momentum for an incompressible flow, meaning divergence is zero, are given as follows:

$$\frac{\partial h}{\partial t} + \frac{1}{r}\frac{\partial (ruh)}{\partial r} = 0 \qquad \textbf{(1)}$$

$$\rho\left(\frac{\partial hu}{\partial t}+\frac{1}{r}\frac{\partial rhu^2}{\partial r}\right)=-\tau_\beta \qquad \textbf{(2)}$$

Basal shear force, τ_β, is the shear stress between the spreading drop and the solid plane and has dimensions force per unit area. Let the thickness of the droplet be defined by the function $h(r,t)$, dependent on the radius over time, and the depth-average velocity defined by $u(r,t)$ [11]. Assuming the drop aspect ratio, i.e. the ratio of the height of the droplet to the radius of the droplet, h/R, is negligible, allows us to ignore inertial pressure terms, and stresses in the normal and tangential directions. We will use the approximation for shear stress as: $\tau_b \approx \frac{\mu U}{h}$. From equation (1), and from the fact that divergence is zero at $r=0$, the equation for velocity as a function of radius and time is reduced to:

$$u(r,t)=-\frac{r}{2h}\frac{dh}{dt} \qquad \textbf{(3)}$$

Simplification of the equation for conservation of mass ultimately yields:

$$\frac{dh}{dt}+2\frac{Uh}{R}=0 \qquad \textbf{(4)}$$

Similarly, from the conservation of momentum, we are left with

$$\rho h\frac{dU}{dt}=-\tau_b, \qquad \textbf{(5)}$$

the equation for acceleration. Making the substitution for basal shear stress, and the droplet velocity front becomes:

$$\frac{dU}{dt}=-\frac{\mu U}{\rho h^2}. \qquad \textbf{(6)}$$

We include the simple the rate of change of the radius over time, equivalent to the spreading drop's velocity:

$$\frac{dR}{dt} = U \qquad \textbf{(7).}$$

We have now based our model of an outward, radially-spreading paint drop on a system of three ordinary differential equations using the simplest time-dependent model of inertial spreading with radius: $R = R(t)$; height: $h = h(t)$; front velocity: $U = U(t)$ [11].

Schematic Diagrams for Two-Dimensional Paint Drop Radial Spread

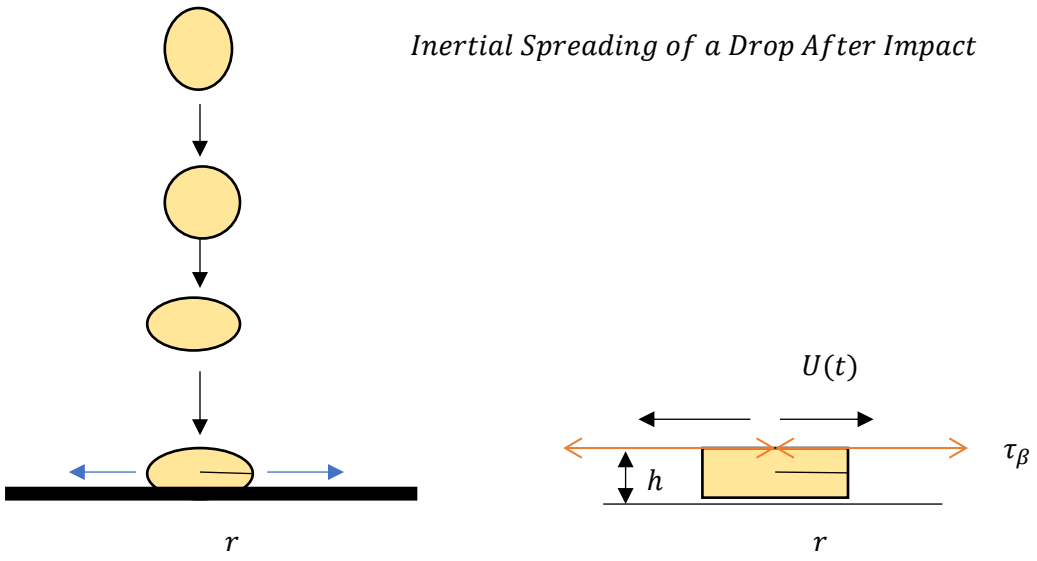

Figure 29. A falling drop oscillates under gravity and surface tension forces to make spherical and ellipsoidal forms. After impact with a solid surface, inertial and viscous forces compete until equilibrium is reached.

First, we assume that immediately upon impact, a droplet has a uniformly circular shape with an initial radius, $R_{t=0}$, (see Figure 30). This will be the first of three initial conditions in our system of equations **4, 6, and 7**. Discretizing points along the circumference of the initial droplet, we assume each point will then move radially outward creating a finger moving at an initial velocity, $U_{t=0}$, which will be the second initial condition, and thus determines each point's new radial distance, $R_{t=1}$. This process continues for each successive time interval, $\Delta t = 0.01$ for the time-step in our ode solver. The third initial condition to our system will be the initial height or thickness, $h_{t=0}$, of the droplet. This magnitude of this value, we estimate to be roughly between the radius of the drop and the diameter, or twice the radius. The height is assumed also to be initially uniform throughout the droplet, i.e. rectangular in shape as shown below in the schematic diagram for thickness, or height, Figure 31. The last schematic, Figure 32, demonstrates the forces acting on or in our particular system, $i.e.$ basal shear force, which may tell us something about acceleration.

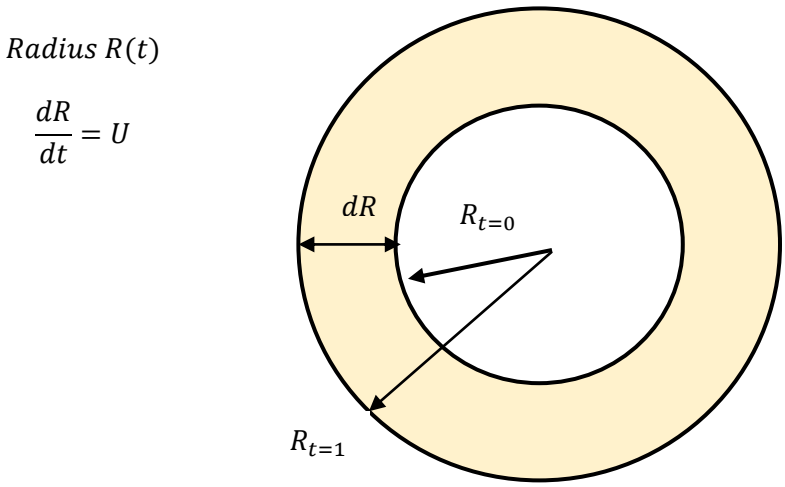

Figure 30. **The initial drop is assumed to be circular. The circumference, we will assume, is made of discrete points that radiate outward with no angular change. It is in fact a continuous fluid mass made of an infinite number of points.**

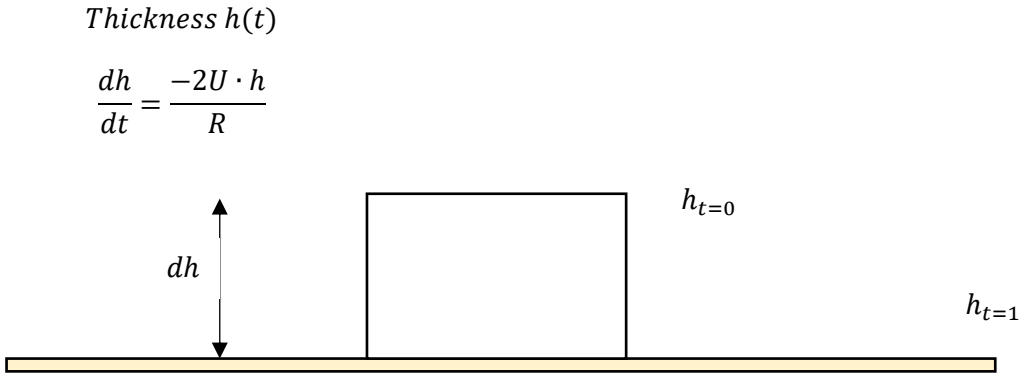

Figure 31. Height, or thickness h, is assumed to be uniform which would give the model droplet a rectangular shape, simplifying the geometry of our model.

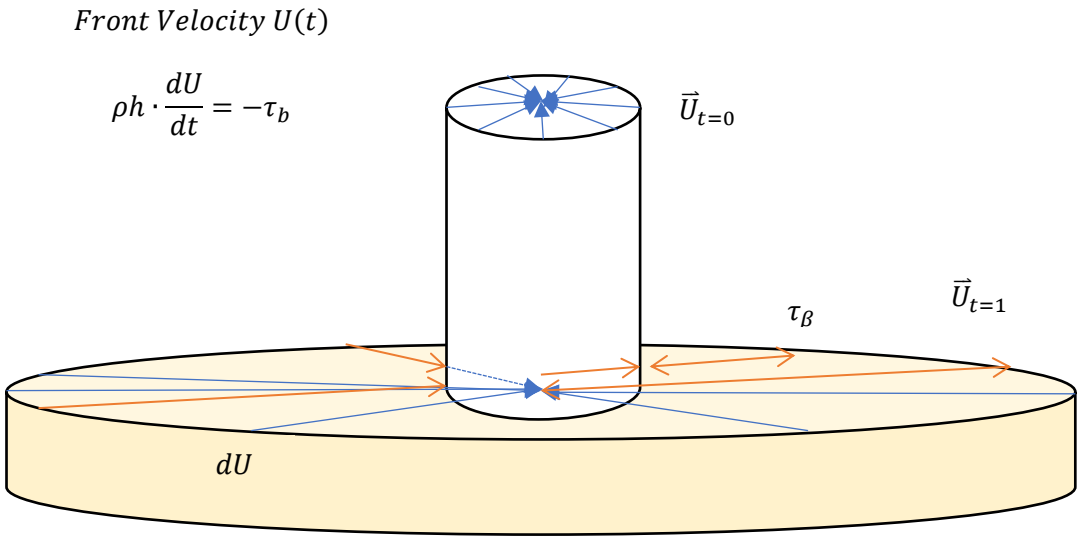

Figure 32. Basal shear stress is the pair of forces, acting in opposite directions, but parallel to the surface.

3.1.1 The Homogeneous Case

We begin our radial-spread model with the homogeneous case, varying only the number of circumference points which produce a finger. Droplet height and radius are fixed. For the homogeneous case, we assume that the solid, impact surface is smooth for a first approximation. For our model, we assume a discrete number of points along the circumference, N, radiate outward at the same rate or initial velocity, also called the front velocity. In reality, the circumference of the spherical-ellipsoid droplet is a continuous, fluid mass and thus consists of an infinite number of points moving at different rates. Since each point moves outward at the same rate, there are no true fingers for the homogeneous model, but rather a radially-symmetric system that has spread outward, covering a certain portion of the canvas. From our experimental data, recall from chapter 2, we measured the change in effective radius over time for a radially-spreading drop using ImageJ software.

From this data, $\frac{\Delta R}{\Delta t}$, we determined the front velocity, $i.e.$ the average velocity at any given point along the leading edge of a fluid body, to have a value on the order of $U = 10^{-3}$ to10^{-2} meters/second. Again, using ImageJ software, we measured the longest distance that covered the maximum spread called the effective radius, $R_{eff} = 1.106\, cm$. The initial radius $R_0 = \frac{R_{eff}}{2} = 0.553\, cm = 0.00553\, m$; recall the outer diameter of the medicine dropper nozzle measured 4 millimeters. A reasonable initial condition for the height of the drop at the moment of impact is then roughly $h_0 = 2R_0$ or $h_0 = 0.01106\, meters$. Also included in chapter two's experimental data, were measurements for the viscosity of three types paint, and in one particular paint, we found the value for $\mu = 0.00257\, Pa \cdot s$, paint-droplet density, $\rho = 998.0\, kg/m^3$

We have now extracted enough information from our experimental data to use for the parameters and initial conditions needed to run the system of equations **4**, **6**, and 7, beginning with the homogeneous case. We used MATLAB to find an approximate solution using a suitable numerical method. The initial velocity at each circumference point, $i.e.$ the point from which each finger originates, is constant, and using equations **4**,**6**, and **7**, along with the ode solver ode45, a MATLAB function which implements a fourth and fifth order Runge-Kutta method for numerical approximations to non-stiff differential equation, with a variable time-step for efficient computation. Order of Runge-Kutta is determined by the truncation of terms from a Taylor series expansion of approximations for a solution to a differential equation. We based our model of an outward, radially-spreading paint drop on the system of three ordinary differential equations with the following assumptions – gravitational effects are neglected, the drop has already made an impact on a surface.

Surface tension is the force on the water drop inward, maintaining a spheroid form for a minimal surface area; radial stress, the stress toward or away from the central axis, and hoop stress or circumferential stress, the normal stress in the tangential direction, are all assumed to be zero. We are not examining the impact splash dynamics, and we neglect hysteresis, a term for particle ejection often referred to as "splashing". To simplify our theoretical model, we deal only with spreading. The following three figures graphically show the typical profiles for a droplet:

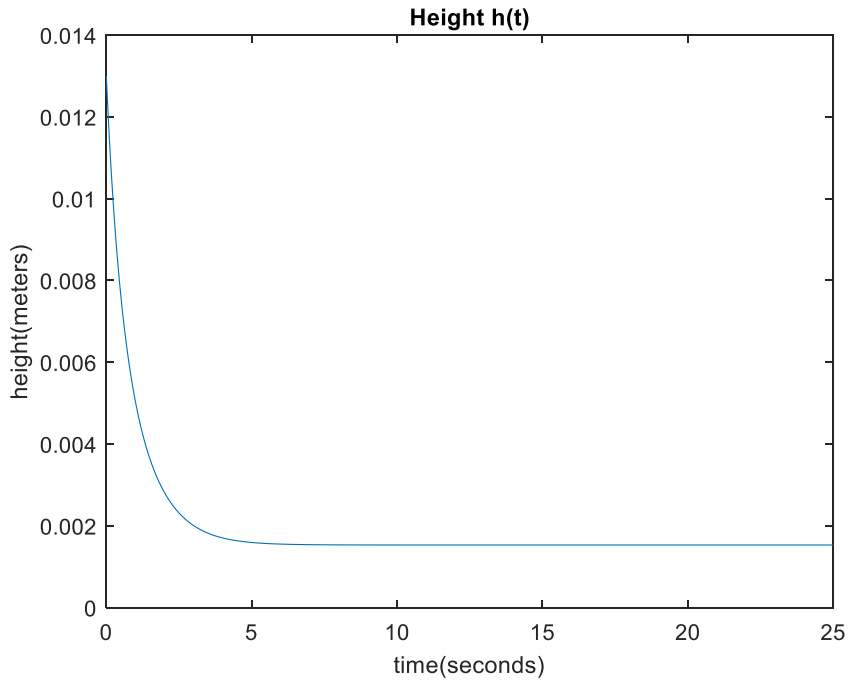

Figure 33. Between 0 and 5 seconds, the height of the drop has reached a minimum value, or saturation point, and is asymptotic to some value which is greater than 1/10th the initial height.

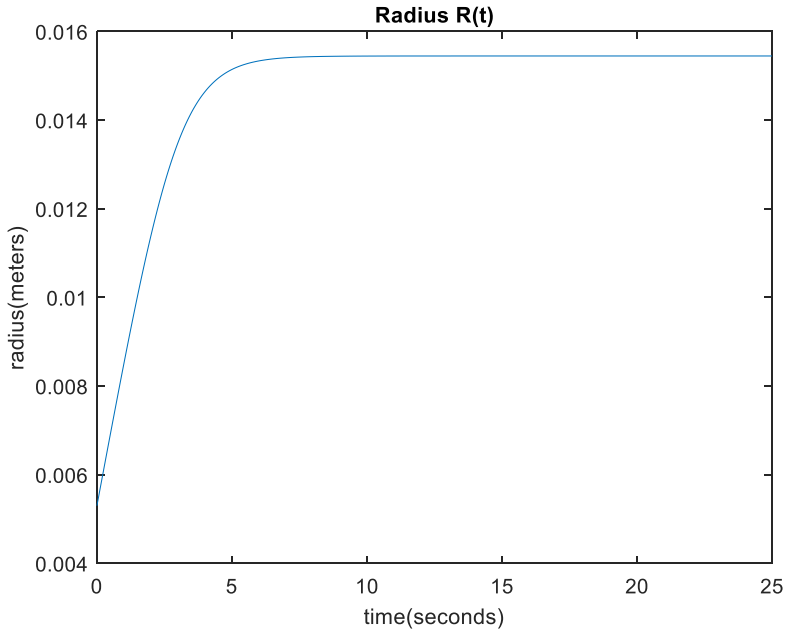

Figure 34. The radius of our model droplet attains a maximum displacement between $t = 5$ *to* 10 seconds.

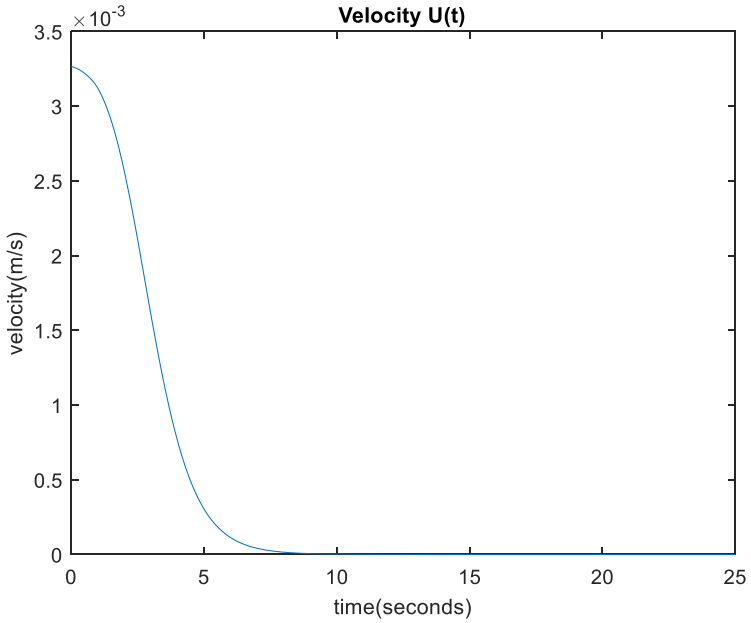

Figure 35. The ordinary differential equation for velocity is asymptotic to zero between $t = 5$ *to* 10 seconds.

The above profiles are what we might expect to see. The height should decrease rapidly as the drop spreads out over time; the radius will increase until it reaches a saturation point; and the velocity is asymptotic to zero in the long term. The next step is to create a two-dimensional representation of a radially spreading droplet. Figure 36 is an example of the type of output figure using conditions for the homogeneous case under our model. The red circle is the initial droplet, plotted according to the initial conditions $R_0 = \frac{R_{eff}}{2} = 0.00553\ m$. On the circumference, N = 700 points radiate outward with a constant initial velocity as the droplet spreads outward on the surface.

We experimented with different values of N ranging from 50 to 1,000 points, evenly spaced around the circle. The output figure was then subjected to the same analysis for possible fractal dimension, as was performed on our experiments presented in chapter 2. That being the case, recall that the image is converted into a black and white, or binary version, the color threshold having been set in the program so that values below the threshold will be converted to black, and those above will be converted to white, $i.e.$ zeros or ones. We will use the value of N = 700 for our comparison study cases as we investigate the effects of changes to various parameters, similarly to the qualitative and quantitative analyses made in chapter 2. Figure 36 shows an example of a droplet with 700 radii of equal distance. We will say more about fractal dimension later, but the D_f for the figure is given for future reference and comparison. Figure 37 shows that fractal dimension increases as N increases.

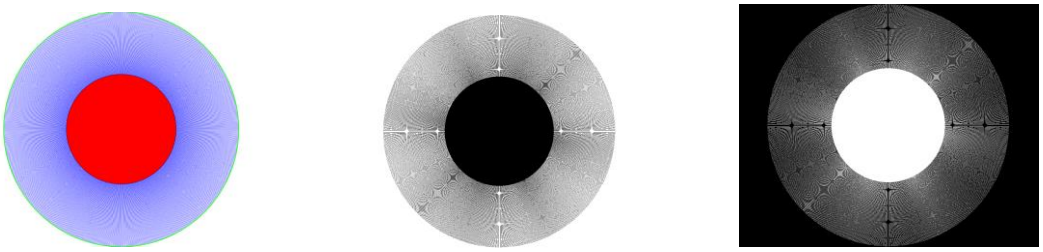

Figure 36. An example of the homogeneous case for 700 fingers or circumference points; average $D_f = 1.95 \pm 0.01$. The output rendering is converted to black & white. The image is then inverted and the box count method computes the fractal dimension. All MATLAB codes used for this analysis can be found in the Appendix.

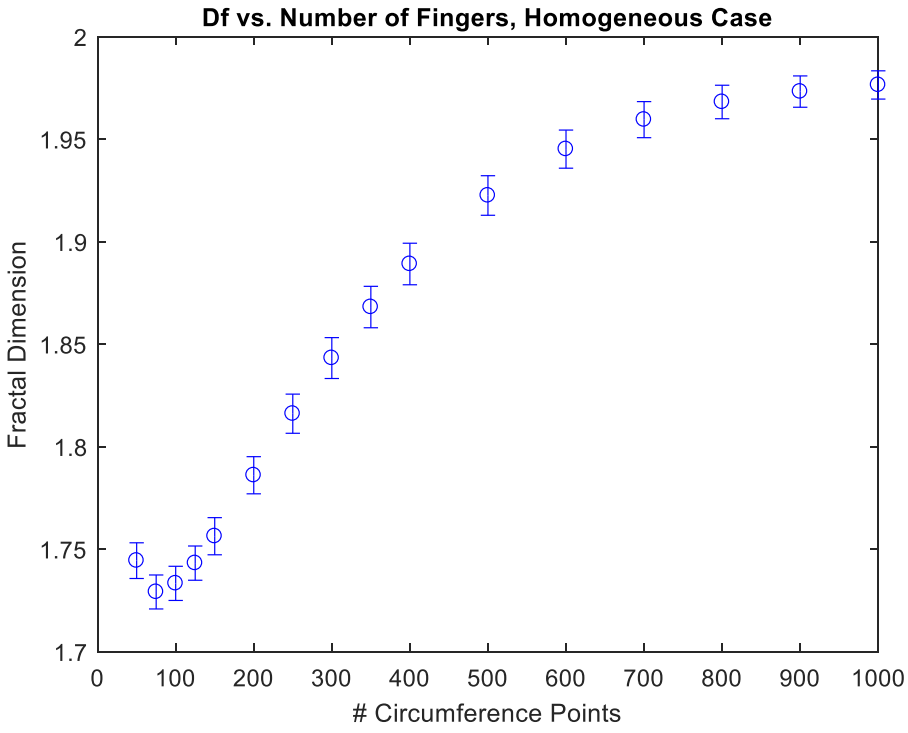

Figure 37. Fractal dimension increases with increasing number of circumference points, N, for the homogeneous case. Initial velocity, $U_0 = 0.00327 \frac{m}{s}$ for each circumference point. The average D_f with standard deviation shown by use of the error bars, was computed for 200 cases, for increasing values of N. Convergence to 2 begins around $N = 700$ circumference points.

As the number of circumference point increases, so does the fractal dimension, with Figure 37 showing convergence of D_f to some real number less than 2. The more radii, the more surface area is covered. Interestingly, though, the D_f is not a constant value at each N. A loop of 400 trials per value of N was run, recording the D_f for each trial. There is a range of values for the fractal dimension of the MATLAB generated figures, for any value of N. The error bar plot in Figure 37 shows the average fractal dimension with one standard deviation. In theory, because the paint drop is spreading outward radially, the D_f should be 2, but we are getting values on average of about 1.95 ± 0.01, due to the discretization, resulting in an error of about 2.5%.

3.1.2 The "Stochastic" Model

In order to account for the inhomogeneities intrinsic to each type of watercolor paper's roughness, we introduce a stochastic element to the system by randomly varying the velocity at each circumference point as a real value between zero and one. The effect of "paper quality" or roughness, is modelled by utilizing MATLAB's random functions for the velocity at each finger, again assumed to have originated along the circumference point for the initial drop. Upon impact, the drop will begin spreading radially, however due to roughness of paper along with porosity, some parts will radiate outward more slowly than others. Once again, we assume that immediately upon impact, a droplet has a uniformly circular shape with an initial radius, $R_{t=0}$. This will be one of the initial conditions in our system of equations **4, 6,** and **7**. Taking points along the circumference of the initial droplet, we assume this time, that each point will then move radially outward with a

velocity, U, which will be the second initial condition, and thus determines each point's new radial distance, $R_{t=1}$, creating a finger. This process continues for each successive time interval, $\Delta t = 0.01$ for the time-step in our ode solver. The third initial condition to our system will be the height or thickness, h, of the droplet. The magnitude of this value, we estimate to be roughly between the radius of the drop and the diameter, or twice the radius. The height is again assumed to be initially uniform throughout the droplet. Figure 40 illustrates the inertial spreading incorporating the stochastic element to our model. We have included some typical simulation results for final height, radius, and velocity, from which we derived respective profile figures. We created a two-dimensional model of the final resulting pattern from a radially spreading paint drop. However, it would not only be extremely time-consuming but meaningless to examine the profiles for height, radius, and velocity for each finger emanating from the drop. Therefore, we need some other metric by which to analyze the final patterns. We used fractal dimension, as we did as part of the analysis of our paint-drop experiments. Results were saved in excel spreadsheets, recording the D_f for 200 trials (a process which takes about 4 hours to complete). Beginning with N = 50, the number of circumference points (Figure 38), we derived an average value and one standard deviation. The number of circumference points, N, ranged up to 1,000 (Figure 39). What happens to fractal dimension as the number of fingers increases? As more surface area is covered, dimension values increase. In total, we generated about 3,000 random splash patterns, for which was calculated the fractal dimension of each trial output image. It is worth mentioning that the analyses of our paint-drop experiments were conducted using over 750 images. All MATLAB code can be found after the References

section. Figure 75 shows how fractal dimension changes as N changes for the non-homogeneous case. The range of values varies from roughly 1.73-1.97.

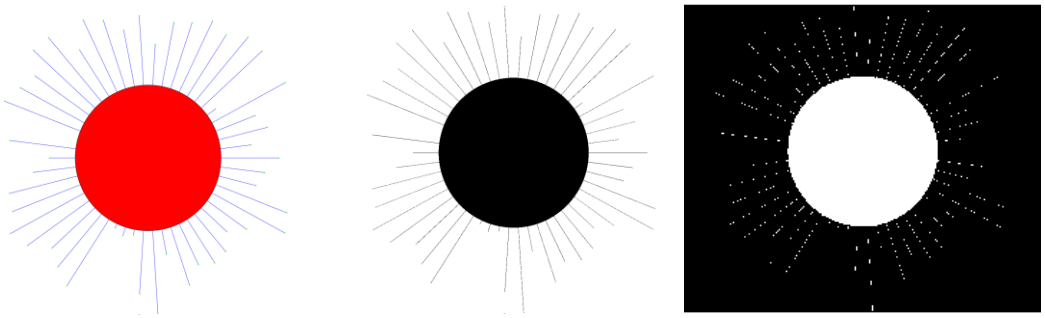

Figure 38. This is an example of the output figure of a paint droplet with $N = 50$ circumference points radiating outward to form fingers.

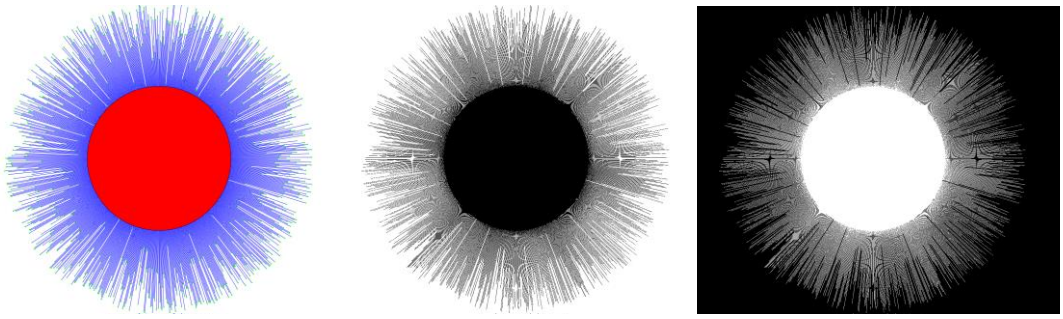

Figure 39. This is an example of the output figure of a paint drop with $N = 1,000$ circumference points radiate outward to form fingers.

Stochastic model of a slow spreading droplet

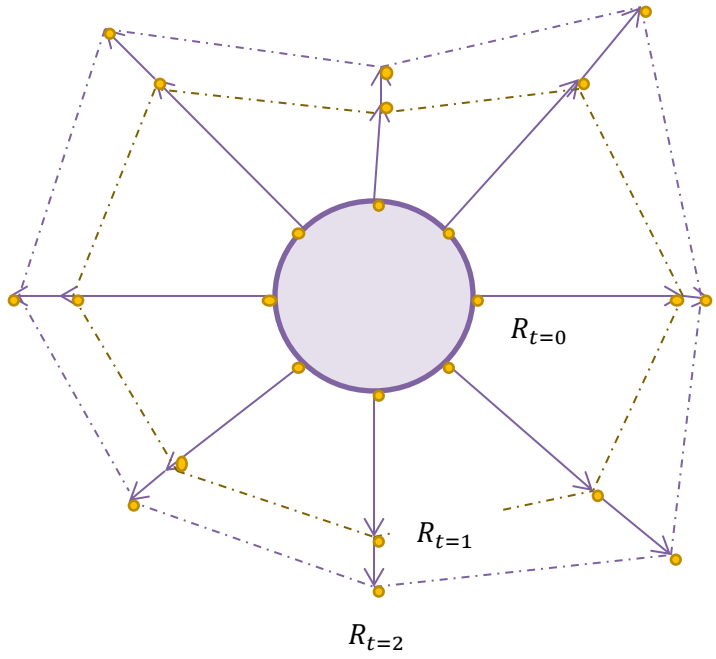

Figure 40. The stochastic nature of a radially spreading droplet. We assume each discrete point has an initial velocity, randomly chosen. This is done to model the porous nature of the paper, to the effect that some radii will flow slower than others.

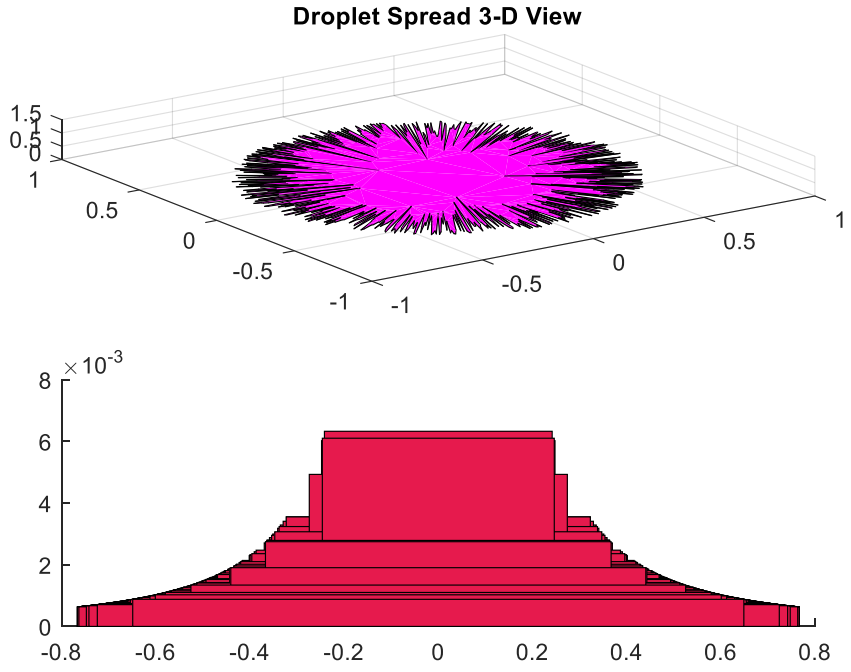

Figure 41. Three-dimensional view of the final pattern and the droplet height/thickness as it flattens on the substrate.

Figure 41(a) gives a 3-D view of a two-dimensional representation of the stochastic conditions for velocity in our model for radial spreading; 41(b) shows the stepwise decrease in droplet height as equilibrium is reached.

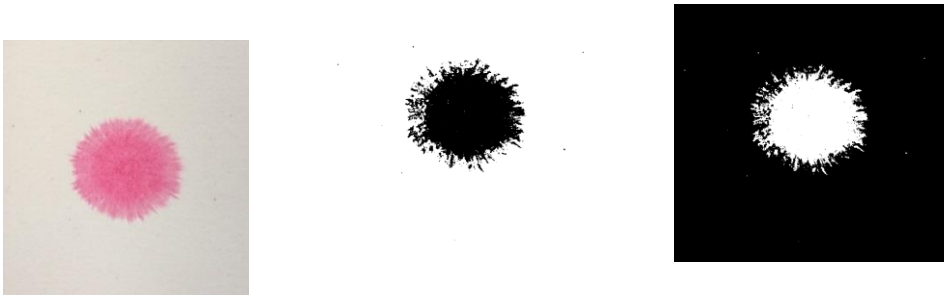

Figure 42. Permanent rose unfrozen paint droplet experiment #10, along with its MATLAB black and white conversion figure, and inverted black and white figure, $D_f = 1.8426$. A value between 0 and 1 is chosen as the threshold, colors with chrome values above are rendered black, and those below are rendered white.

Figure 42 shows an image from the transient stage from one of our paint-droplet experiments. The experiment and the 2-D figure generated by our model look very similar.

3.2 Temperature Effects

Until this point, we have assumed the initial temperature of the canvas to be room temperature and thus the change in temperature equals zero for the sake of simplicity. We used 25 degrees Celsius for the value for room temperature. However, much of our experimental work involved releasing a droplet onto a frozen surface. The motivation for this method was driven by the curiosity to explore water's complex behavior and various forms, $e.g.$ snow, ice, frost, $etc.$, under different temperature conditions, and to incorporate this technique to the watercolor paint medium; then to make any qualitative and possibly quantitative analyses within the physics of art. As this was the case, we incorporated Newton's formula for heating/cooling into our model to simulate the experimental conditions:

$$T(t) = T_R + (T_0 - T_R)e^{-\beta t} \qquad (\mathbf{8})$$

$T_R = 25℃$, is room temperature, and T_0 is the initial temperature of the paper substrate, which will vary according to our experimental results, i.e. $T_0 = -15℃$ or $T_0 = -5℃$ or $T_0 = 8℃$, the experimentally measured, average initial temperatures at the beginning of our single-droplet-painting experiments. When $T_0 < T_R$, this is indicative of a system that is heating up; if $T_0 > T_R$, then this is indicative of a system that is cooling down. From our graphs of data recorded for the changes in temperature of the paper substrate over time, we used the curve-fit feature to determine three different beta values for each of the three cases of initial temperature of the canvas. Since this temperature equation is an exponential

function, we adjust for values less than or equal to zero by adding T_R to all of the data points and then using the nonlinear curve fitting feature in both Maple or Excel, which uses the method of non-linear least squares algorithm, to extract the value for β in each case.

Table 8. Beta values for exponential rate of heating at three different initial temperatures extracted from experimental data shown in Figure 9.

Case I: unfrozen canvas $T_0 = 5.1$ ℃	$\beta_{\text{unfrozen}} = 0.01$
Case II: canvas frozen 5 minutes $T_0 = -2.6$℃	$\beta_{\text{frozen 5 min}} = 0.031$
Case III: canvas frozen for 30 minutes $T_0 = -15.1$ ℃	$\beta_{\text{frozen 30 min}} = 0.053$

It has been well established that viscosity is affected by temperature. The experiments performed in this area are numerous, and the number of articles on temperature's effect on viscosity is numerous and available publicly [63]. Thus, we can say with certainty that the viscosity (μ) of our paint will decrease with rising temperature. Because each droplet of paint contains mostly water, we will assume that the viscosities of watercolor paints behave similarly to that of water and thus we make use of the exponential decay rate for water's change in viscosity with respect to temperature, which is determined to be $\alpha = 0.029$ [63]. Consequently, we incorporated a temperature dependent model for viscosity (Reynolds' viscosity model [64]) as follows:

$$\mu(T) = \mu_0 e^{-\alpha(T-T_R)} \quad \textbf{(9)}$$

where μ_0 is the initial viscosity, in our case the viscosities of the three watercolor paints used. Hence, our model for the equation for the velocity becomes:

$$\frac{dU}{dt} = \frac{-\left(\mu_0 e^{-\alpha(T_0-T_R)e^{-\beta t}}\right)U}{\rho h^2} \quad \textbf{(10)}$$

The other two equations 4 and 7, although they remain unaltered in their form, are nonetheless affected by the temperature and viscosity components which we have now added to this dynamical system. To our knowledge there have been no previous studies of splash droplets under these conditions. One additional key assumption for the figures above is that the surface of the canvas be homogeneous, smooth, and continuous surface, thus the droplet would spread at the same rate in every direction. Also, much of our experimental work involved releasing a droplet onto a frozen surface. As this was the case, we incorporated Newton's formula for heating/cooling and we incorporated a temperature dependent model for viscosity where μ_0 is the initial viscosity, in our case the viscosities of the three kinds of watercolor paints used, $T(t) = T_R + (T_0 - T_R)e^{-\beta t}$, $\mu\,(T) = -\mu_0 e^{-\alpha(T_0-T_R)}$, which exhibit respective profiles:

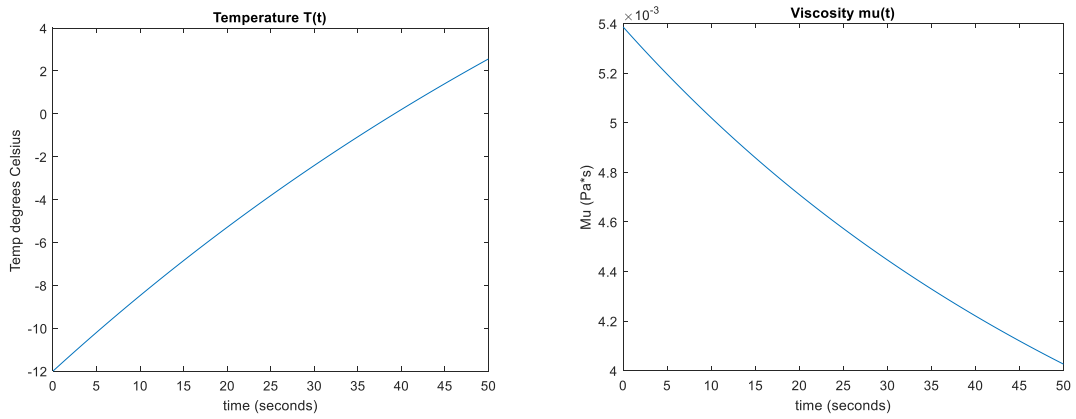

Figure 43. The profiles for temperature and viscosity are indicative of a system that is heating up at an exponential rate. It is expected that viscosity will decrease as the temperature of the system increases.

We summarize the equations, which we will be using to create our model of a slow-spreading paint droplet, and plot the figure of what would be analogous to the final resulting images of the experimental data analyzed in chapter two:

$$\rho h \cdot \frac{dU}{dt} = -\tau_b$$

$$\tau_b = \frac{\mu U}{h}$$

$$\frac{dR}{dt} = U$$

$$\frac{dh}{dt} + 2\frac{Uh}{R} = 0$$

$$\mu(T) = \mu_0 e^{-\alpha(T-T_R)}$$

$$T(t) = T_R + (T_0 - T_R)e^{-\beta t}$$

Figure 44. Summary of equations used in our model.

3.2.1 Temperature Effects on The Homogeneous Case

The initial temperature of the paper substrate in our model has an effect on the average radial displacement, as seen in Figure 45b. This seems like an inherently logical relationship, and the results from our computer model are supported by the results of our paint-drop experiments - the colder the initial substrate temperature, the shorter the radial spread. We need to use some metric to describe the results of this radially-spreading droplet, i.e. fractal dimension. We are looking for any effective change in the output figure at different temperatures. There is very little effect on the fractal dimension of the final pattern, regardless of substrate's initial temperature. The D_f for the homogeneous case is

fairly constant. There is a small range of variation, $1.950 - 1.968$. The reason for variations in fractal dimension, may be, in part, due to image resolution of the output figure as it is loaded into the box count code. This process then may lead to numerical differences and thus variations in calculations. The range of variation in D_f is similarly equal to the accuracy of the box count code convergence studies, which we demonstrated to be less than 1% error. The average final-radius, in the second panel, (shown with error bars indicating one standard deviation), increases slightly with increasing paper temperature.

At this point we investigate what effect, if any, changing the value of β will have on the fractal dimension. Keeping fixed the initial temperature at $T_0 = T_R$, the number of fingers on the circumference of the droplet, $N = 700$, we ran the two-dimensional model simulation code two hundred times for all three values of β, yielding the following average D_f values with one standard deviation. Table 9 shows the results. Are the three average values for D_f more or less equal, or is there an upward trend? As the exponential rate of change in heating/cooling, β is increased, the fractal dimension is increased. (Figures 67, 68, and 69 located in the Appendix are scatter plots showing the fractal dimension for 200 trials for each value of β.)

Table 9. Average D_f for three different values of beta using the stochastic model.

$N = 700$	$\beta = 0.010$	$D_f = 1.8969 \pm 0.0101$
	$\beta = 0.031$	$D_f = 1.8977 \pm 0.0097$
	$\beta = 0.053$	$D_f = 1.8980 \pm 0.0098$

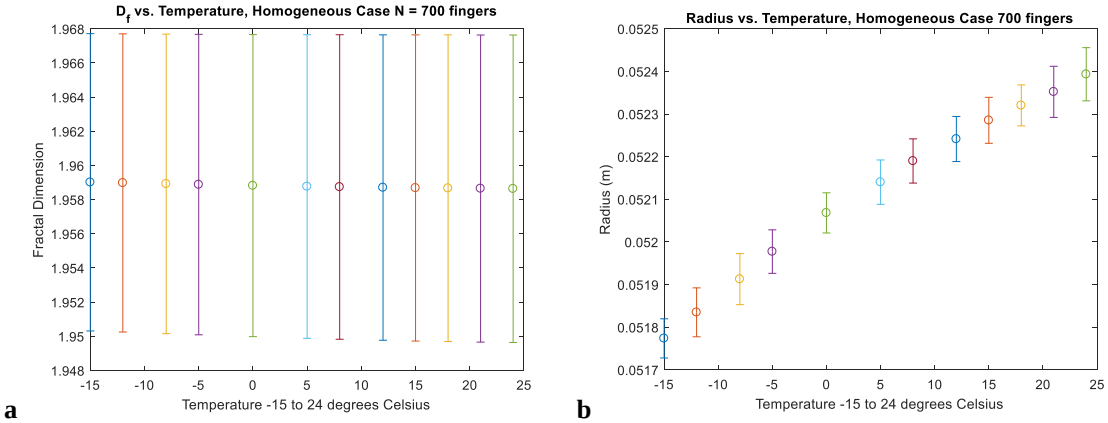

Figure 45a. D_f vs. Temperature for the homogeneous case. 45b. shows the effect of temperature on radial displacement. Error bars represent one standard deviation for an average value computed for 200 trials for each initial temperature shown in the graphs.

3.2.2 Temperature Effects on The Stochastic Case

Using MATLAB's ordinary differential equation solver, ode45, incorporating experimentally determined values for β, the exponential rate of growth/decay for the heating formula, ρ, the density of a paint droplet, μ_0, the initial viscosity of the paint at room temperature, initial conditions for droplet height, h, radius, R, and a randomly chosen value for velocity, U, we were able calculate numerical approximations for the final values

of the time-dependent position variables, as well as the final values for the temperature-dependent parameters. Compare the Figures 42 and 46 using the following initial conditions and parameters: number of circumference points, $N = 700$, initial temperature, $T_0 = 25℃$, room temperature, $T_R = 25℃$, the exponential rate of heating/cooling, also called Newton's Law of heating/cooling, $\beta = 0.01$, the exponential rate of heating/cooling, for what is also known as Reynolds' Viscosity Law, $\alpha = 0.02$, initial viscosity, $\mu_0 = 0.00257\, Pa \cdot s$, and initial velocity, U_0, for each finger will be between 0 and 1cm/sec for each circumference point on the perimeter of the drop. Each one of 700 U_0's is randomly generated by the MATLAB function command: $U = (randi([0,10]) + rand)/1000$, which will randomly choose an integer on the closed interval from zero to ten, add a random real number greater than zero but less than one, and divide the sum by one thousand, which would output an infinite number of initial velocities within an interval, $0 < U < 0.011$, in other words, roughly between 0 and 1 cm/sec. Clearly this interval contains the value for the velocity we measured, $U = 0.00327\, m/s$, in our experiment. The final time for the MATLAB ode solver was chosen at the time when the lower bound for the final height was one-tenth the initial height, because the order of the numbers we are using range from 10^{-3} to 10^{-4}.

We ran the same substrate-temperature-effect study as the homogeneous case on the stochastic model. The average fractal dimension with one standard deviation is plotted below in Figure 47. Figures 48 and 49 compare average fractal dimensions for increasing values of N for two cases, frozen and unfrozen substrate, and shows smaller readings as temperature increases. Figures 45 and 50 show the effect of temperature on the average radial displacement.

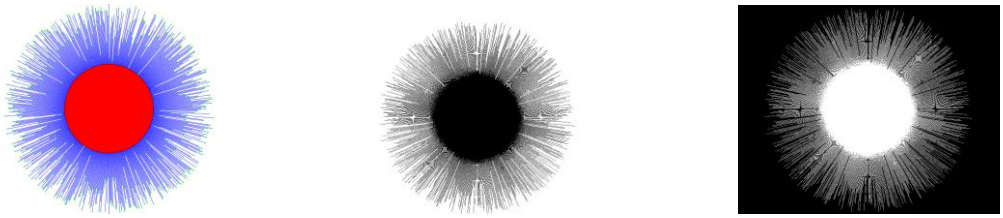

Figure 46. An experimental result for the stochastic model using MATLAB, $D_f = 1.8759, N = 700$. Each finger radiates outward with a randomly generated initial velocity resulting in a smaller value for fractal dimension compared to the homogeneous case.

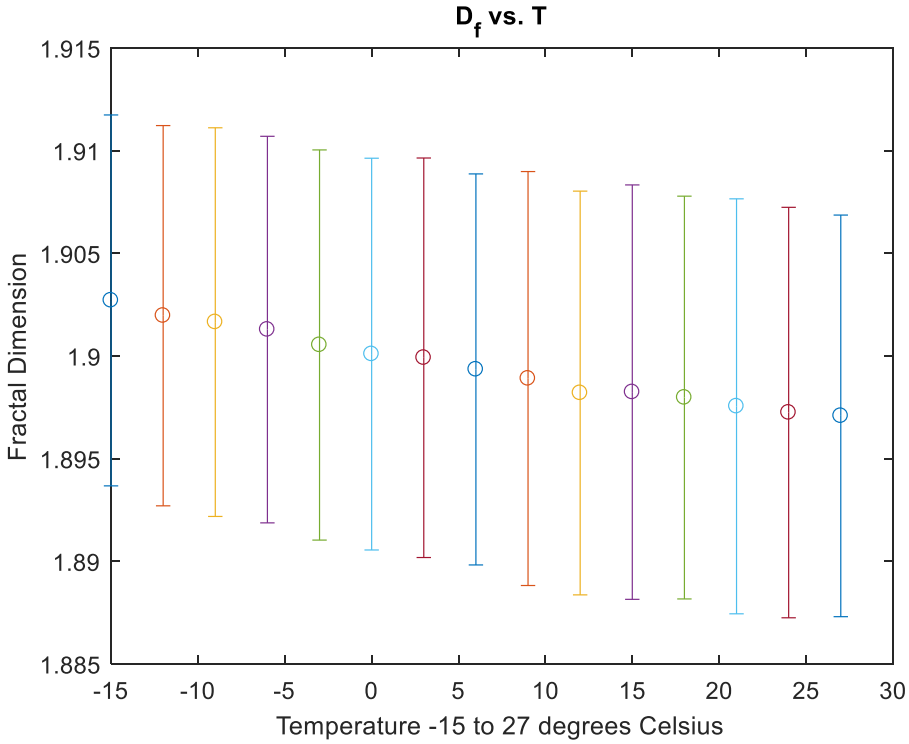

Figure 47. $N = 700$ fingers, stochastic case $U_0 \approx 1\ cm/sec$. Increasing temperature suggests a downward trend in fractal dimension.

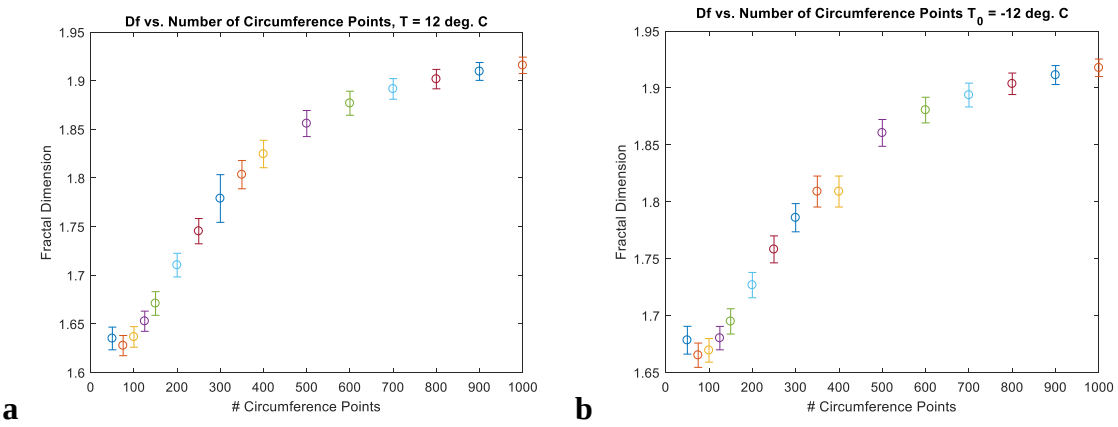

Figure 48. Fractal dimension will be affected by the number of fingers, N, however temperature effects are more difficult to discern. The average value for a droplet with 700 circumference points is around 1.88, regardless of temperature. Effects of temperature are observed when there are fewer circumference points.

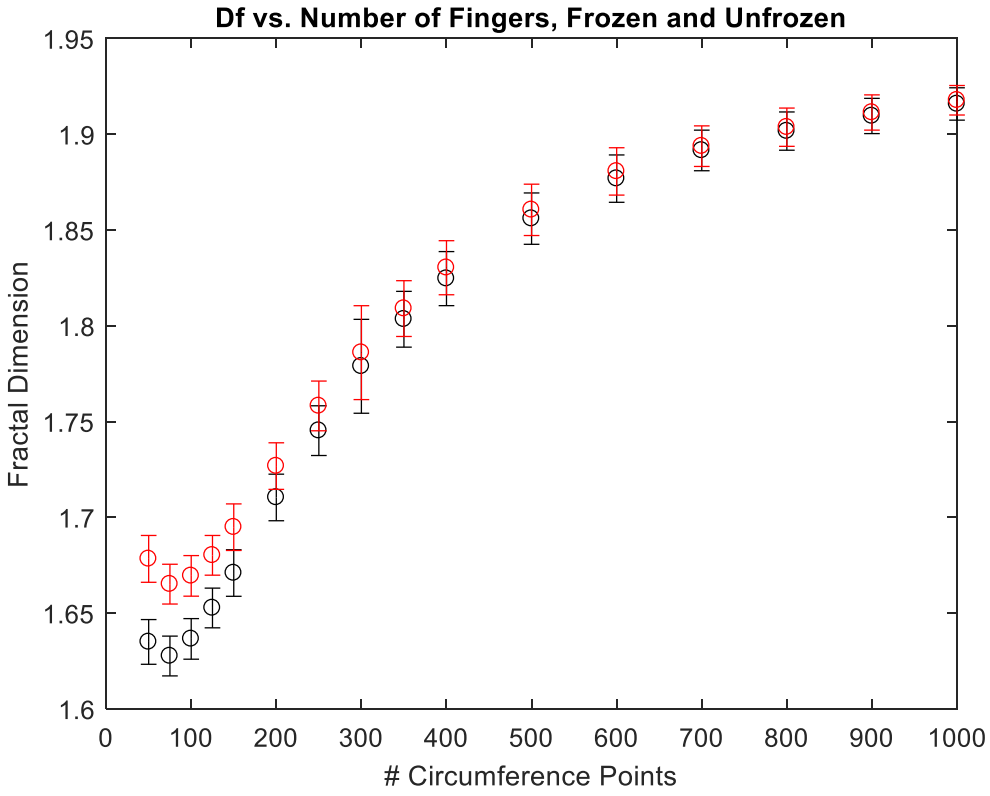

Figure 49. Temperature will also affect the final pattern and fractal dimension of the dispersed drop. Two cases are compared here, case i: temperature = -12 degrees Celsius (shown in red); case ii: temperature = +12 degrees Celsius. Overall, D_f decreases as temperature increases. Beginning around 700 circumference points, the differences become negligible as the two curves begin to converge.

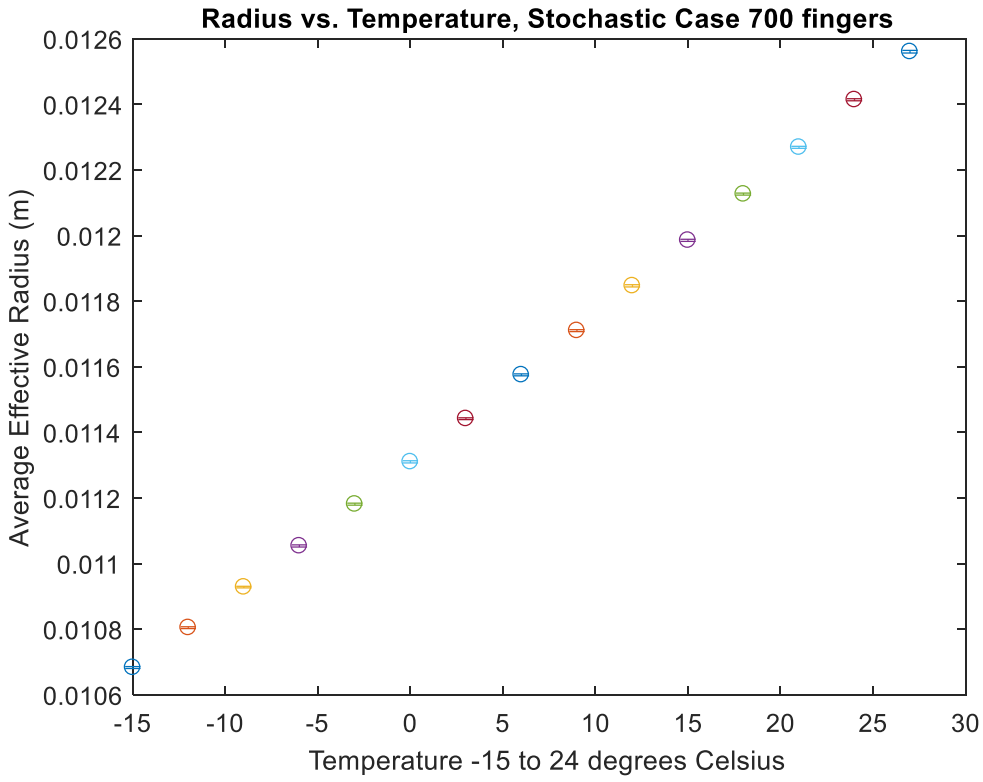

Figure 50. As temperature increases from frozen values to room temperature, the average effective radius will also increase showing results for average, effective radius generated with our theoretical model.

3.2.3 Comparison with Experiments

Now that we have a model for the radial spreading of a droplet of paint, let us compare our experimental results with our model system beginning with the same initial conditions and parameters. First, we begin by showing the power law function curve fitted to our experimental measurements, see Figure 48. The method of non-linear least squares is used to find the best non-linear function fit. The R^2 term is a statistical measurement of curve-fit accuracy (not to be confused with our use of R for radius) is very close to 1, indicating that this function is a good fit. These measurements were taken from movie

stills as a camera filmed the droplet spread immediately beginning at time of impact. In Figure 51, we see the data measurements, along with the power law function plotted on the same axes as radius profile from our model system of equations 4,5, and 10. Figure 53 shows the velocity profile from our model plotted on the same axes as measurements from our experiment along with the first derivative of the power law curve to see how accurately our model matches our experimental observations. The radial profiles are very good approximations (Figure 52). One significant difference is the shorter length of time that the experimental data takes to reach a saturation point, resulting in a shorter radial displacement, but why? What can we refine to account for this energy loss? The velocity profile (Figure 53) shows that the first derivative of the radial function of time, $R'(t)$,indicated with the black dashed lines is a good fit to the experimental data, shown in magenta circles. Our model's velocity profile demonstrates a slower convergence toward equilibrium. To what can we attribute this energy loss within our system? The same comparisons were made for the three temperature conditions we studied in Chapter 2. Table 10 gives the initial conditions and parameters for a substrate frozen for 30 minutes. The individual profiles for height, radius, velocity, temperature, and viscosity are shown in Figure 54. As might be expected, we observe that it takes longer for the profiles to achieve equilibrium. Figures 55 and 56 show the model radial and velocity profiles respectively, on the same coordinate axes as the experimental data. There is a significant difference between our model functions and experimental results. Radial displacement shows a time lag, which would occur during the molten phase of the substrate's temperature change. This phase change was not considered in the design of our model. The velocity

profile shows a perturbation in the experimental data, (magenta circles), for which we must account in our system of equations.

Table 11 and the figures that follow compare our paint-droplet experiment for a paper substrate frozen for 5 minutes. There is not much noticeable difference in the individual profiles, see Figure 57, except that temperature and viscosity curves are showing signs of non-linearity. Temperature will have an effect on maximal, radial growth, as we saw in the previous section on temperature effects, but this would not be noticeable on figures at this scale. Notice the spike in the radial spreading (Figure 58), that is missing from our model, however both curves eventually saturate on the same time scale. As in the frozen experiment comparison, the early dissipation of energy is seen in the gap between the model and the experimental data. The short-lived lag in the radial spread and the small perturbation in the velocity profile (Figure 59) would again be happening during the molten phase change from ice to water.

Table 12 and the subsequent figures compare results for our model on unfrozen watercolor paper. Keep in mind that the power law curves make use of the average values for coefficients and exponents collected from the experiments of chapter 2. Experimental data, plotted in magenta circles, are each a representative from the three temperature case studies we performed. The early dynamics for the radial spread are best studied using a high-speed camera. Overall, though, our model compares favorably.

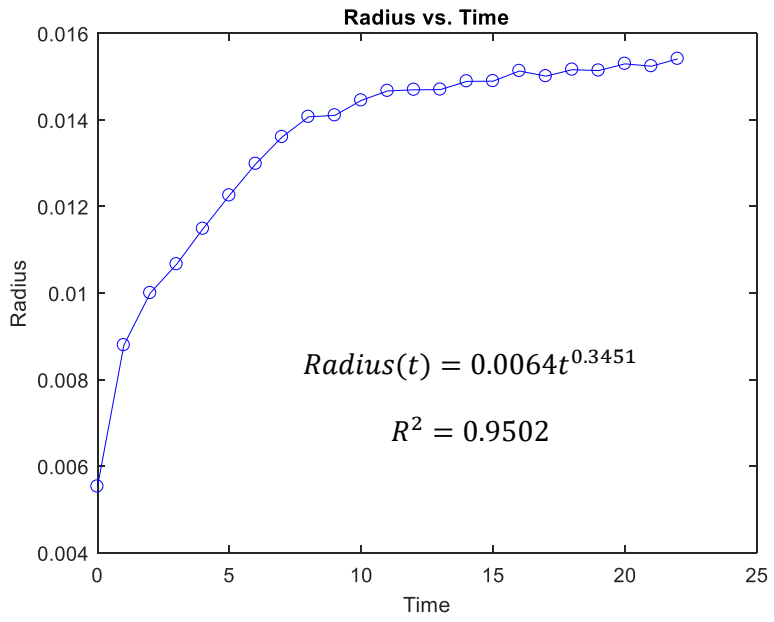

Figure 51. Data points (in blue) for radial spread measured using ImageJ. Radius is measured in meters; time units are seconds. The function, Radius(t) is the extracted non-linear power law curve fit, with R^2 value indicative of a highly accurate fit.

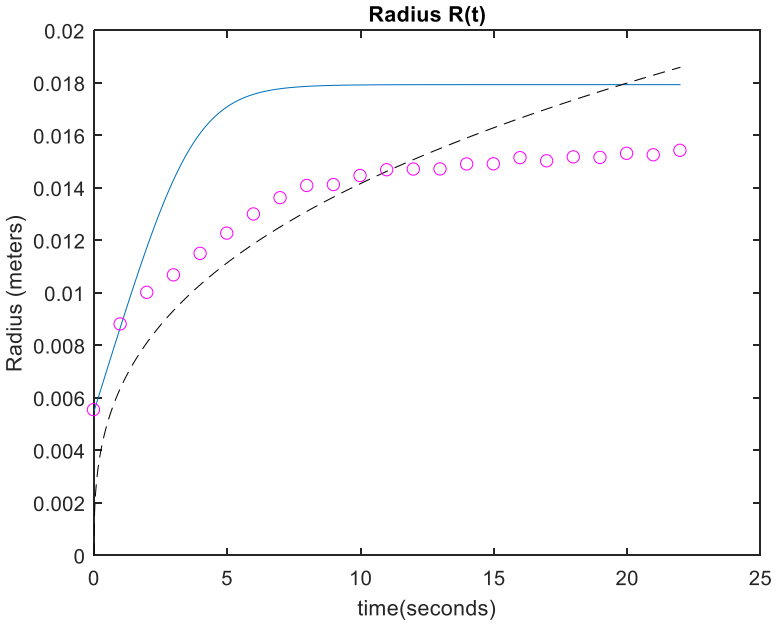

Figure 52. Compare the radius spread using ode45 solver from MATLAB, shown in the solid blue line, with experimental values measured using ImageJ at 1 second intervals, plotted in magenta circles, along with the power law fit, $Radius(t) = 0.0064t^{0.3451}$, shown by the black dashed curve.

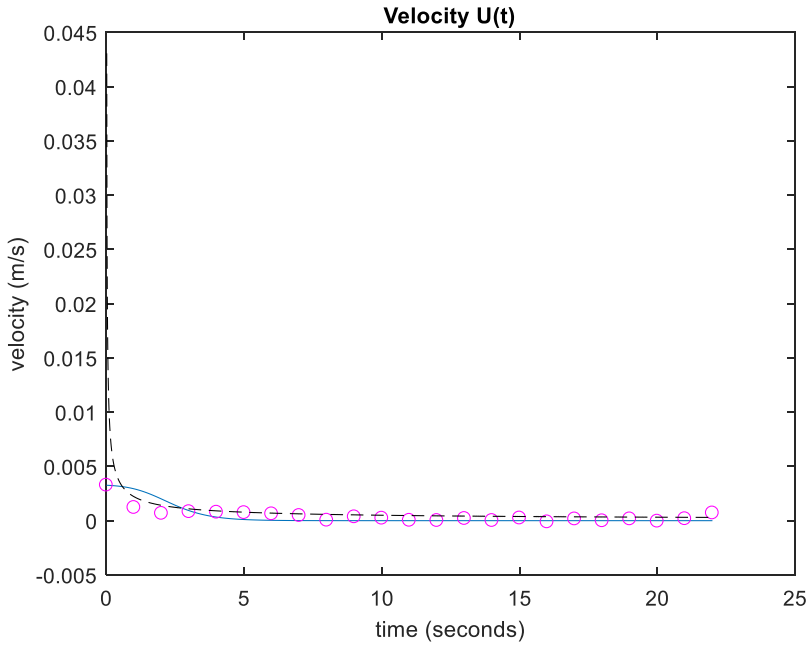

Figure 53. Velocity, $U(t)$, is plotted above using ode45 solver from MATLAB (solid blue line) along with experimental data collected to calculate velocity change over time, again at 1 second intervals (magenta circles), and the first derivative of the power law fitted curve, $R'(t) = 0.00221 * t^{-0.6449}$ (black dashed curve).

Table 10. Radial droplet spread, model simulation for canvas frozen for 30 minutes.

$$T_0 = -15℃, T_R = 25℃, \rho = 998.0\frac{kg}{m^3}, \mu_0 = 0.00257\ Pa \cdot s,$$

Initial	Height	Radius	Velocity	Temperature	Viscosity
	0.0130 m	0.0053 m	0.0009 m/s	-15℃	0.0054Pa·s
Final	Height	Radius	Velocity	Temperature	Viscosity
	0.0035 m	0.0102 m	0.0001 m/s	-8.479℃	0.0050 Pa·s

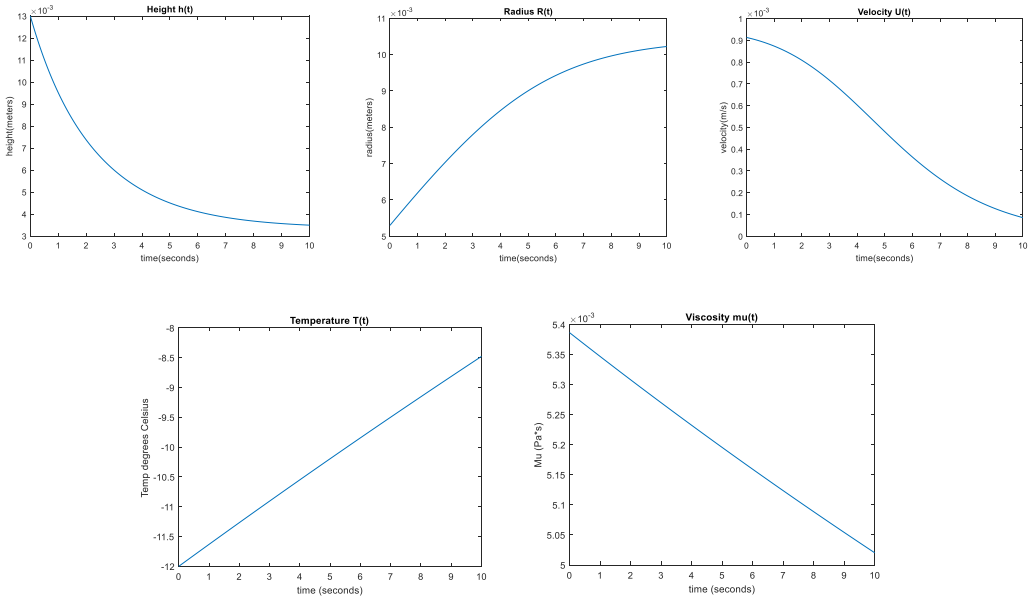

Figure 54. Profiles for our model simulating conditions for a substrate frozen for 30 minutes.

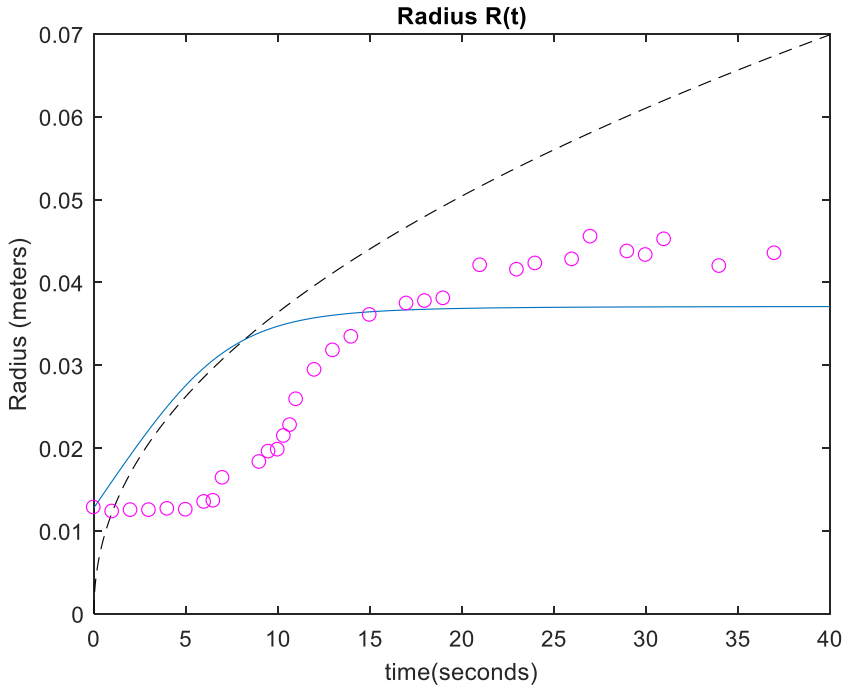

Figure 55. On the same set of axes, the plots above for the power law, $r = 0.0123t^{0.471}$ shown by the black dashed line, along with the data from experiment #8, shown in magenta circles, and our model system of ordinary differential equations shown by the solid blue line.

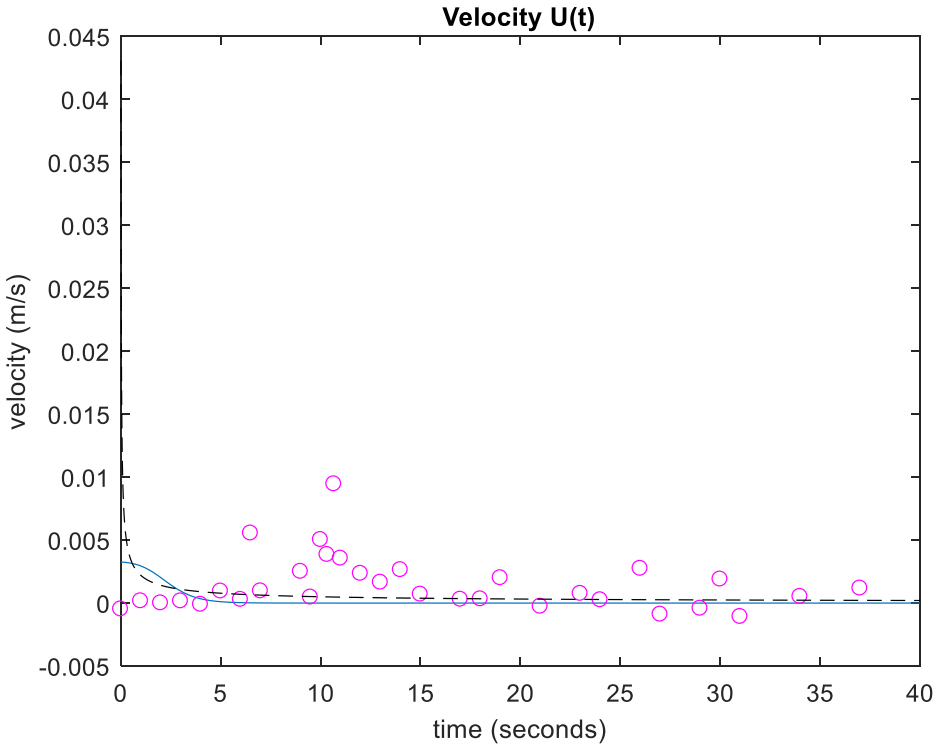

Figure 56. Velocity profiles for our model (solid blue line), the first derivative of the power law (black dashed line), and data collected from a paint drop experiment (magenta circles).

Table 11. Radial droplet spread model simulation for canvas frozen 5 minutes.

For a canvas frozen for five minutes: $T_0 = -5℃, T_R = 25,$

Initial	Height	Radius	Velocity	Temperature	Viscosity
	0.0275 m	0.0159 m	0.0033 m/s	-5℃	0.0047 Pa·s
Final	Height	Radius	Velocity	Temperature	Viscosity
	0.0034 m	0.0450 m	0.0000 m/s	1.638℃	0.0041 Pa·s

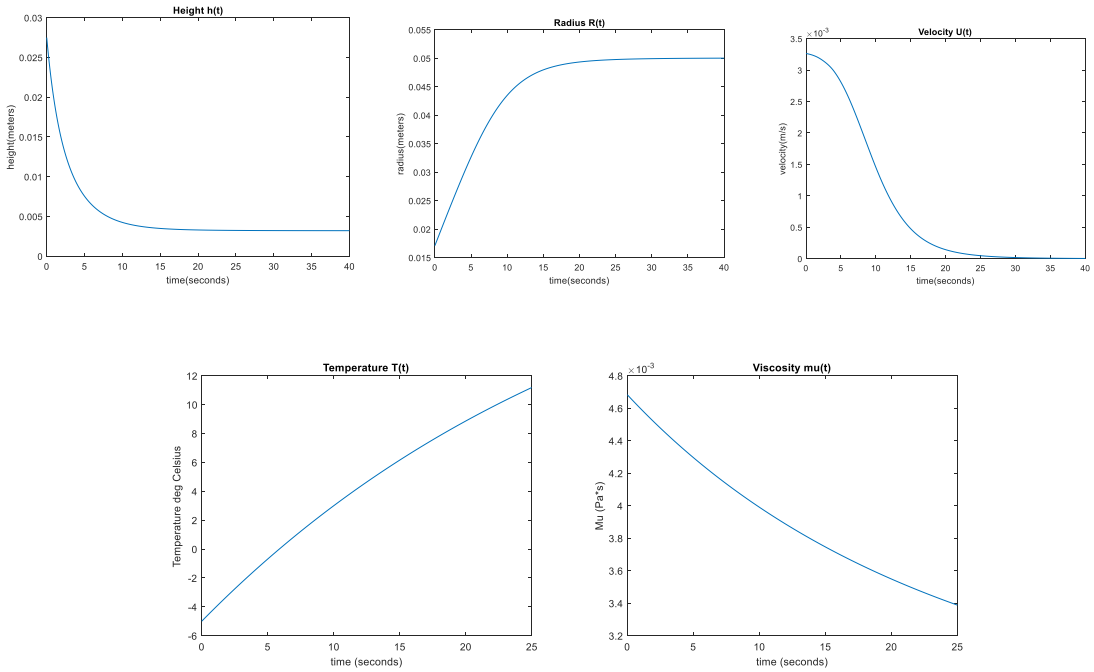

Figure 57. Profiles for our model, simulating conditions for a substrate frozen for 5 minutes.

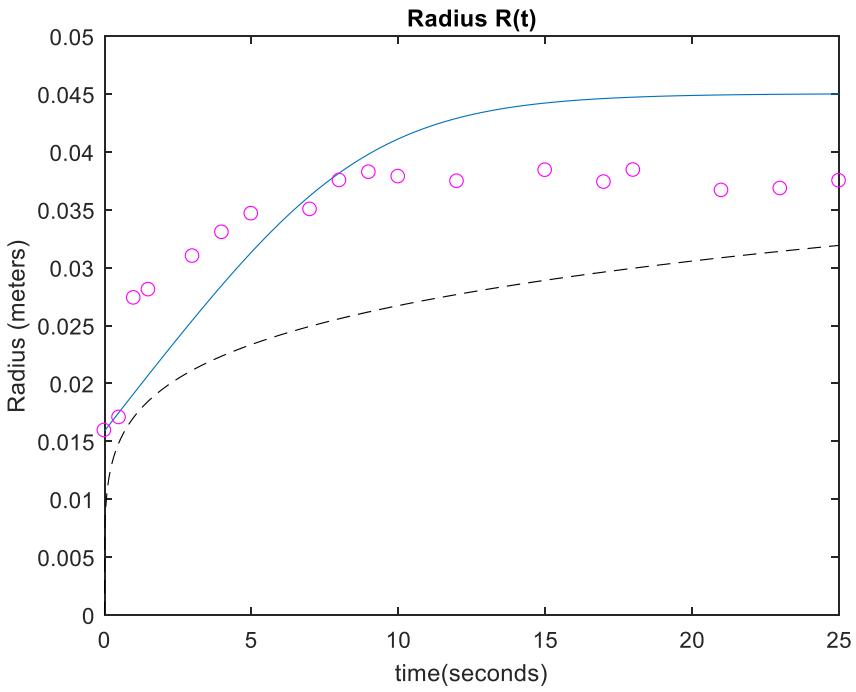

Figure 58. Compare the plots for power law curve (dashed line), our ode model (solid line), along with the data from paint drop experiment #1, permanent rose released with a medicine dropper from a height of 6 inches onto 90 LB paper frozen for 5 minutes.

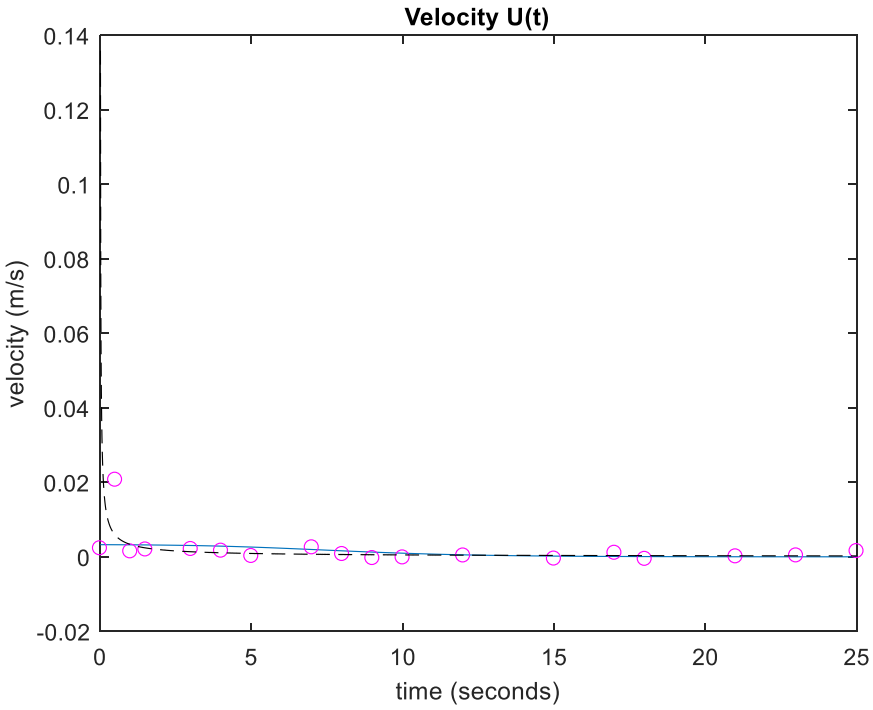

Figure 59. **Now compare the plots for the first derivative of the power law curve (black dashed line), our ode model (solid blue line), along with the data from experiment #1, permanent rose released with a medicine dropper from a height of 6 inches onto 90 LB paper frozen for 5 minutes.**

Table 12. Radial droplet spread model simulation for unfrozen paper substrate.

For an unfrozen paper substrate: $T_0 = 8, T_R = 25,$

Initial	Height	Radius	Velocity	Temperature	Viscosity
	0.0305 m	0.0162 m	0.0033 m/s	8.0°C	0.0036 Pa·s
Final	Height	Radius	Velocity	Temperature	Viscosity
	0.0032m	0.0503 m	0.0000 m/s	12.0225°C	0.0033 Pa·s

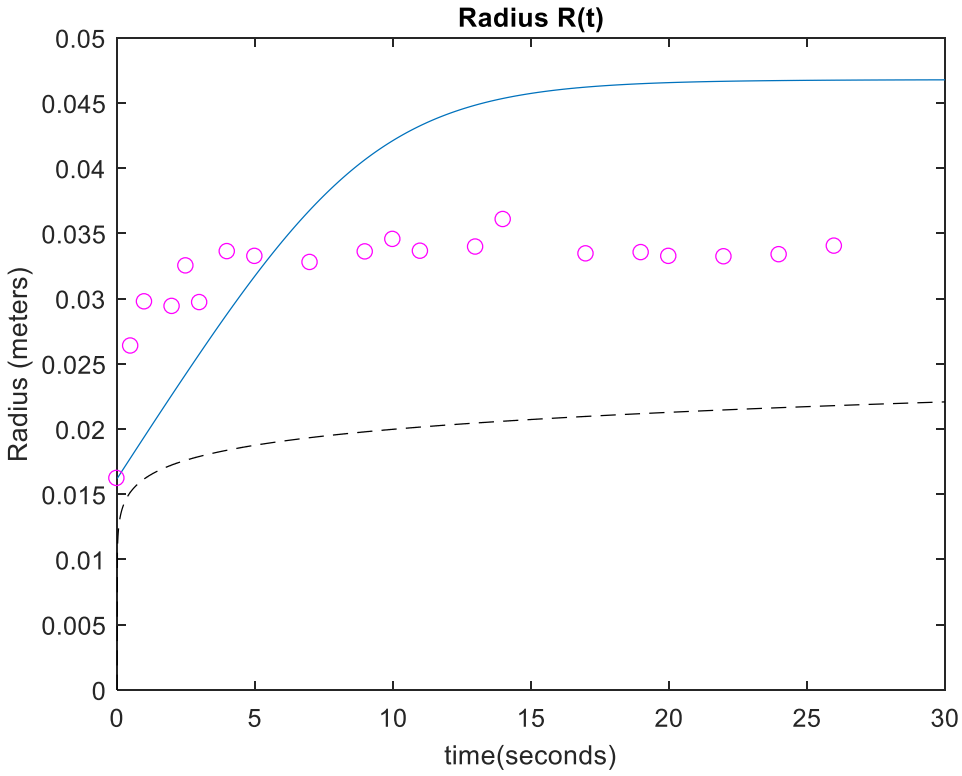

Figure 60. Compare the plots for power law curve (black dashed line), our ode model (solid blue line), along with the data from paint drop experiment #9, medicine dropper of permanent rose, 6", unfrozen, 90 LB paper.

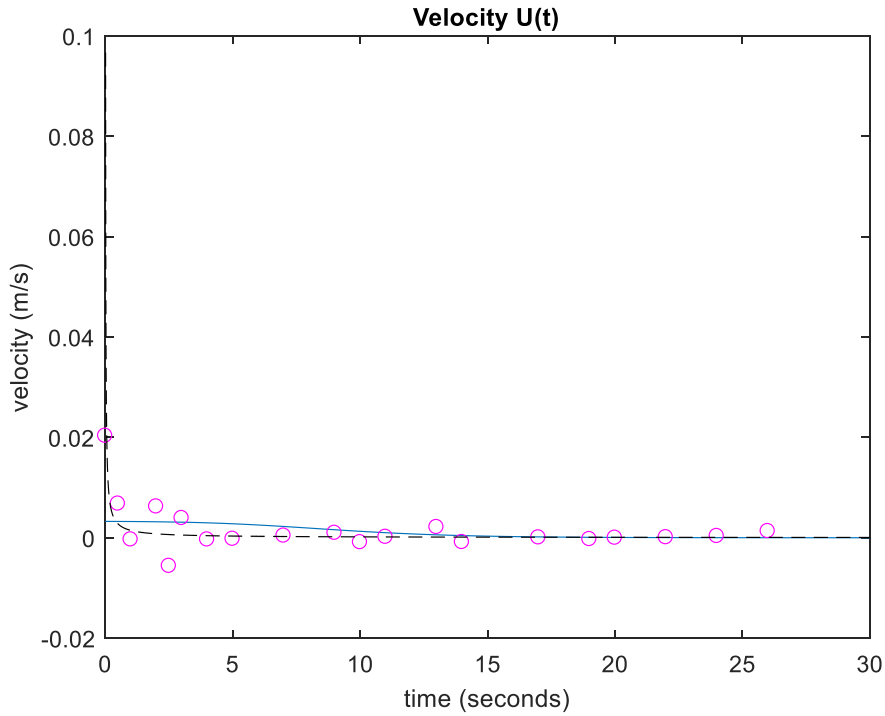

Figure 61. Velocity profiles for our model (solid blue line), the first derivative of the power law (black dashed line), and data collected from a paint drop experiment (magenta circles).

3.3 Fractal Patterns and Calculations

We used our system of ordinary differential equations to run our MATLAB scripts for 200 trials for each change in degree Celsius for temperature and for increasing number of circumference points spreading outward radially from an initial drop impact, assumed to be circular. In total, we generated over 10,000 figures representing our two-dimensional model. MATLAB's function calls linked to Excel make it very convenient to save output data. We collected model results for the longest finger, or R_{eff}, the average radius distance along with one standard deviation, the average final height, with one standard deviation, the average initial velocity, the maximum and minimum initial velocity, with one standard

deviation, and the fractal dimension for each trial. A more rigorous statistical analysis is needed for this data.

We narrowed the focus of our model by using the properties measured for the permanent rose paint. In chapter 2, our statistical analysis showed a correlation between substrate temperature and fractal dimension. In fact, we previously stated that fractal dimension will be significantly lower at freezing temperatures for Prussian blue and sepia paints, the two paints with very low viscosities. Figure 3 showed that the D_f for permanent rose, the most viscous of our paints, increases at freezing temperatures and decreases as the substrate warms up to ambient room temperature, thus confirming the validity of our model for permanent rose watercolor paint, but indicating that we have not accounted for something during dispersal. Future studies would be needed to generate data with the parameters of the other two paints to confirm the validity of our model for those respective experimental results. Perhaps capillary forces have a greater role in the net forces within the system and should not be ignored. After all, basal shear force may at times be on the order of 10^{-2}. Recall the surface tension of water, $0.07\ N/m$.

Focusing our model with the parameters based on permanent rose paint, we performed a series of simulation studies varying one parameter at a time while the others remained fixed to observe any trends in fractal dimension. The parameters we investigated were: initial temperature, T_0, wave-front velocity, U, exponential growth/decay rate, *i.e.* the 3 experimental values for β, the number of circumference points emanating from the droplet impact splash, N. The following data profiles and figures are the results of our model, given the parameters and conditions of our experiments for a canvas frozen for thirty minutes:

Fractal Dimension vs. Number of Fingers

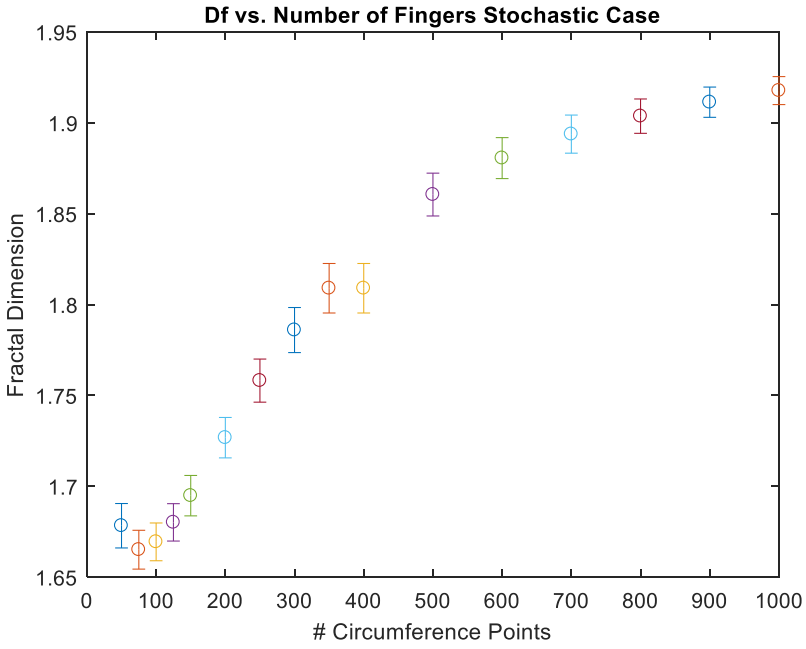

Figure 62. The stochastic case. $\mathbf{0 \leq U_0 \leq 6\frac{mm}{sec} = \frac{randi([0,5])+rand}{1000}}$ **for each finger.**

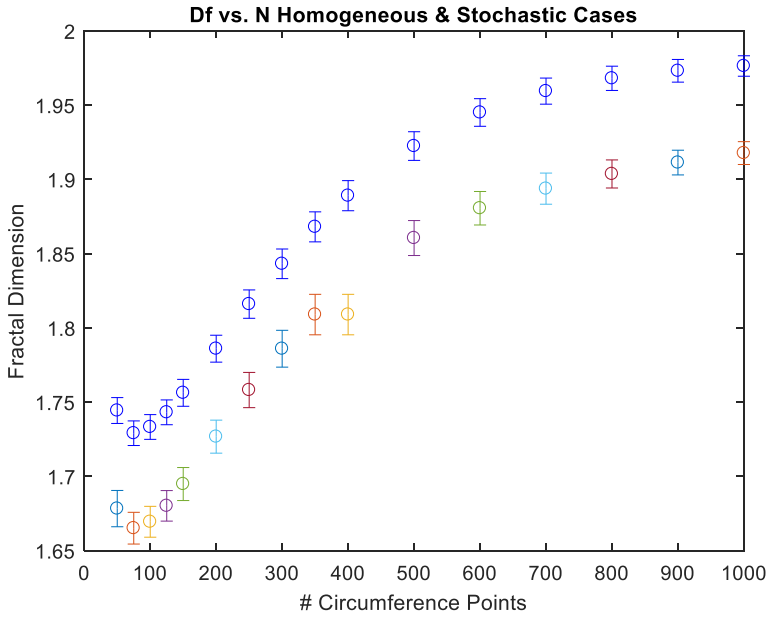

Figure 63. Observe the change in D_f when a homogeneous initial velocity (blue circles) at each circumference point becomes a randomly generated value between 0 and 6mm/sec.

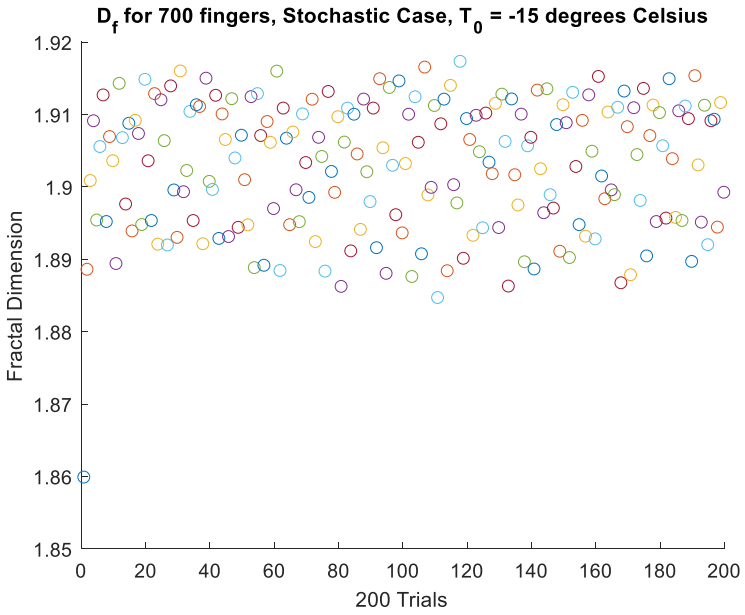

Figure 64. Scatter plot for fractal dimension for 200 trials at frozen temperatures. D_f varies mostly between 1.89 and 1.92, with an outlier at 1.86.

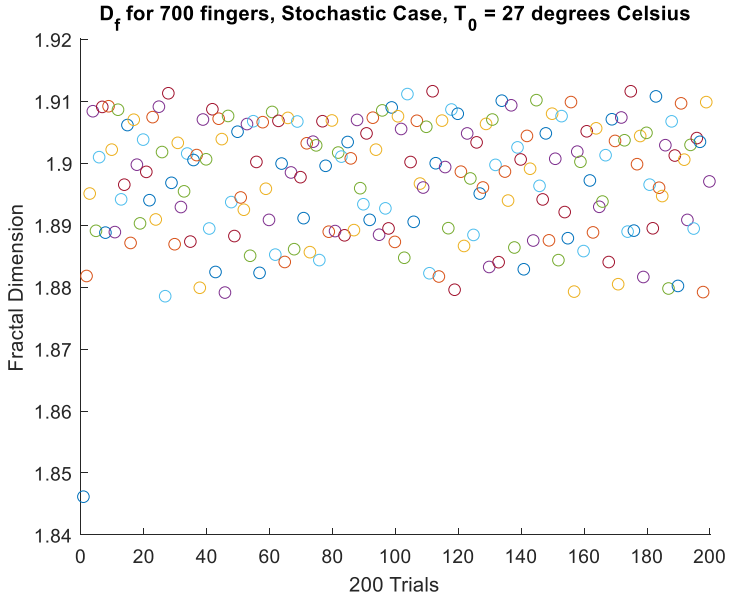

Figure 65. Scatter plot for fractal dimension for 200 trials at room temperature. Fractals range from 1.88 – 1.92, with an outlier around 1.845.

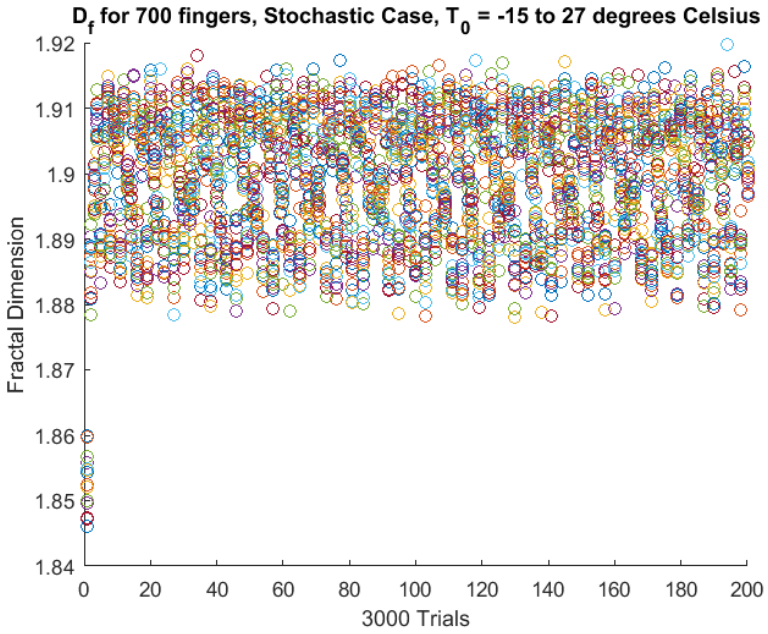

Figure 66. Scatter plot for $N = 700\ fingers, 3000$ trials using our model. Fractal dimensions range from 1.84 - 1.92 as initial substrate temperature changes from -15 degrees Celsius to 27 degrees Celsius.

Chapter 4: Discussion, Conclusions & Future Experiments

In summary, our experimental investigation of droplet patterns from watercolor paints on paper held at different temperatures reveals patterns which depend upon material properties of the paint, paper type, as well as the impact velocity, the temperature, and wetting properties of the canvas. The radial growth pattern of the splash from the time of impact to equilibrium, achieved upon evaporation and settling, is qualitatively similar to that seen in previous studies, but the growth rate can vary between $0.1 - 0.47$, depending upon the level of freezing of the substrate. The range of We and Re puts this analysis in a well-studied part of the experimental phase where capillary and viscous forces compete; however there have been no previous studies on the effects of temperature and the wetting of canvas in quite the same physical context.

Figure 67 gives a qualitative idea of paint absorption which appears to be the greatest at the impact point and caused by the penetration of paint into depths of the wet canvas during first impact (referred to here as "initial absorption"). Details of the absorption process were not pursued in this study which has focused on the long-term pattern evolution. However, we do recognize this to be an important aspect of the fluid dynamics involved here which will be investigated in our follow-up work. We also recognize that the absorption of the paint into the canvas might also continue to occur post impact when the surface is in liquid state. Therefore, in principle, the overall dynamics could be characterized by the competition of not only We and Re, but also perhaps by something additional such as the Blake number, $B = \frac{U\rho D}{\mu(1-\varepsilon)}$, which characterizes flows through porous media. Here U is the flow speed, D the characteristic length, ρ is the

density, μ refers to dynamic viscosity, and ε is the void fraction. In addition, non-Newtonian effects arising from the pigment concentration could also play an important role especially during the impact phase when shear stresses on the droplet are a maximum, making this a truly complex problem. Based on the material and flow parameters of this study, the overall values of B range from $394 - 2155$ and show sensitivity to the canvas, paint type, and release height of the droplet.

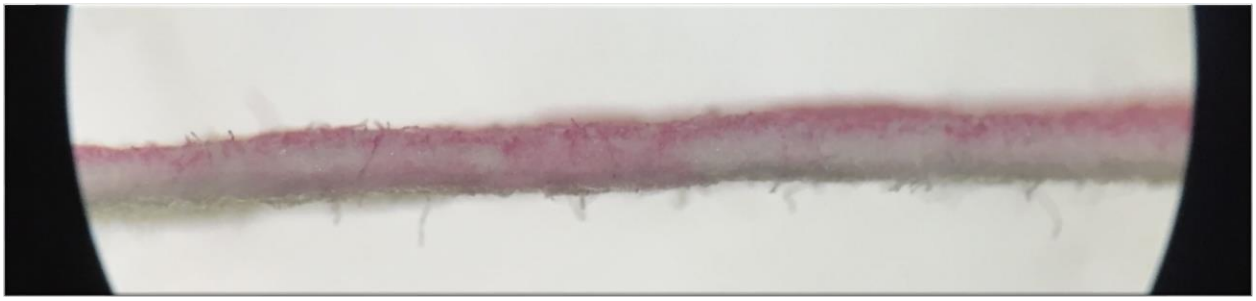

Figure 67. Cross sectional image of canvas showing absorption and penetration of paint through canvas around the droplet impact point.

To qualitatively understand the effect of canvas porosity, we took a few images of the cross-sectional slice of a droplet splash stain done about 5 minutes after the experiment when the paint had not yet had a chance to evaporate. The image was obtained with a confocal microscope set at a magnification of 300. The Figure 67 reveals some penetration, inferred from the pinkish hue of the paint at the center, i.e., the impact point, with not much absorption (at least not at this scale) elsewhere in the observed time. We therefore believe that while absorption might play some role at the early stages of the spread and paint penetration might continue to play a small role at later times as well. Therefore, the phenomenon still maintains the same overall properties as in the case of non-porous surface. In the case of 30-minute paper freezing, the surface is frozen and stays as such for

several minutes past impact reducing the absorption time. Therefore, in this case, viscous and capillary regimes could dominate the absorption phase. Absorption dynamics appear to occur in two extremes of time scales: (i) the very-short time impact scale where the maximum penetration is likely to occur and (ii) the very-long time scales where slow diffusion into the canvas occurs in the liquid-post-molten state of the canvas. Both these phases need further investigation.

Figure 39 demonstrates that our model is quite good for radial paint-drop dispersal on the unfrozen canvas. The gap between the model curve in blue and the measured data in magenta circles is a hopeful indicator that further studies could help refine our model by accounting for this discrepancy, see Figure 52. We hypothesize that our approximation for basal shear stress, $-\tau_\beta \approx \frac{\mu U}{h}$, is the possible source for the model's margin of error, that is we may be missing a non-linear term for our system of ordinary differential equations such as $\varepsilon u''$, if we take a closer look at the acceleration term in the 1-D Saint-Venant equation (**4**). The velocity profiles in Figures 53, 56, and 59 reflect this shortfall in the model, as the measured velocity drops off more sharply than the velocity of our system. In the frozen experiments, there is a lag time in the radial spread due to the melting of the canvas, see Figure 55. With refinement, our model could incorporate this condition by using some form of the logistic model or a time delay. We can adjust for this in equation (**8**), Newton's equation for heating/cooling The velocity profile for the experimental data in Figure 56 (magenta circles) indicates a perturbation in the curve at the 10-minute mark. The experiments under frozen conditions undergo a phase change, a phenomenon that was not previously considered for our model. Incorporating the 1-D Stefan problem, which deals with real, physical problems with a change of phase state, may further refine our model.

We identified specific properties/patterns emerging in our experiments and a rigorous statistical analysis validates the qualitative observations, discussed in Table 2. A box count analysis of the images reveals that the splashes display fractal structure. The fractal dimensions of the observed patterns are analyzed and contrasted with each other, revealing significant correlations to the environmental and material factors in this study. The fingering patterns observed in some of the experiments are seen to strongly correlate to the impact speed of the droplets, and also the freezing temperature and to the wetting of the canvas.

Some of the final patterns left by the paint drops are quite stunning, (Figures 28f, 76, 77). Some patterns are only seen during the transient stages, as presented in the panels for examples of frozen paintings (Figures 22b, 27a-h, 28a-e,). In our 46 paint-drop experiments, we observed that most fractal patterns for this set of images ranged between 1.6 and 1.9, (Figures 73-75), putting our paint-drop experiments, just for comparison's sake, in the range of Pollock paintings from the late-transient period toward the latter years of his productivity, and also yielding dimensions close in value to some of the bench-mark fractals, e.g. Sierpinski gasket, diffusion limited aggregation, etc. Stated simply, fractal dimension is a useful metric. Our model demonstrates that we can generate a pattern with a target D_f value. We must be cautious in using fractal dimension, however. Two patterns may have a fractal dimension similar in value, but appear quite dissimilar. Our "Koch Trefoil", Figure 69, looks nothing like the Sierpinski Triangle, Figure 16c, yet their fractal dimensions are almost identical. There is a discernable pattern along the perimeter of the drop as it radiates outward from the initial drop. It would be a worthwhile pursuit to make a qualitative analysis of fractal patterns found most aesthetically pleasing for different

demographics, similar to the visual studies on Pollock's rhythmic drip paintings [53, 58] and the fascinating application in psychotherapies. It would also be a worthwhile pursuit to make an analytical and quantitative comparison of fractals with dimensions very close in value. Two different figures may look nothing alike or may look similar, and yet their respective fractal dimensions are close in value. The conclusion we draw from these observations, and from our experiments and models is that, strictly using D_f to authenticate an original Pollock is insufficient. Pollock would certainly have moved his body and tools in a unique, rhythmic manner which could theoretically produce a work with a unique result. But, there would, in all probability, be similarities among the works of the entire set. Similarly, it is reasonable to say that all humans share some basic similarities to our personal motions. For example, looking at the set of all signatures of all the world, there are certain characteristics that appear similar among them, just as individual finger prints are unique, but, there are still general qualities in finger prints that are common among the entire population. Fractal dimension, as we showed from our experiments, is affected not only by canvas type, as well as paint volume, viscosity and rheology, but it is also sensitive to the way it is calculated – from the threshold value, used to convert color images to black and white, to the box count method, which exhibited a range of values for an image that was roughly the same as the error for the convergence studies of our bench-mark fractals. But, do fractals offer any other information? They may offer some insight into fluid flow on a greater scale, as in multi fractals [50]. Can we modify our model to make fractal dimension a function of time? Figures 76 and 77 are examples of coincidence of similar patterns left by two different paints. The general shape of these two paintings is not circular, as we assumed for our model. The shape of these two experiments is more like a

trefoil. Is this similar, final result due to one of the forces we neglected? A future consideration might include the include an initial drop oscillating in such a manner that the moment of impact produces the initial shape of the trefoil, fingers radiating outward, and accounting for an angular differential and other sources of energy dissipation. The 2-dimensional, stochastic model for a drop with 700 fingers does indeed look like a very good representation of the real-life phenomenon of a slow-spreading droplet on Arches 140LB rough paper, (Figures 42 and 46) and their respective fractal dimensions are very close in value. These are promising results for our model and confirm that our choice for the stochastic nature of each finger's velocity was a valid assumption. However, could the model be refined by considering what is happening internally to a falling droplet? Are the forces from surface tension, capillary action, or some other neglected stress, i.e. stress toward or away from the central axis, playing more important roles in the drop dispersal than previously thought? Can we begin with a more predictive function for the oscillatory motion of the fluid inside the falling droplet? What if we include a term for angular energy dissipation?

As a scientist, I am pleased with the results achieved with our model. We captured the overall profiles of the various parameters over time, i.e. height, radius and velocity, but what is more, is that there is room for improvement in the model, making this a more exciting and complex mathematical problem. However, as an artist, I find the figures generated by MATLAB lack a certain, 2-dimensional continuity along the perimeter of the final figure which can be seen in the paint-drop experiments. In reality, as water radiates outward, there are interactions and energy dissipation in the xy-plane, however slight as they may be, they add to the overall aesthetics of the final pattern. As a watercolorist, one

of the difficulties of creating a successful painting is to be careful lest the painting look "overworked", a lesson perhaps only learned through trial and error, but good advice given to me by my teacher, Pamela Lovell. In my experience, I have found that most often, the most remarkable results of a painting are the areas where the watercolor paint was left alone to follow its natural spreading behavior, rather than attempt to force the fluid to yield to my wishes - mathematics as art, fluids the artist. As an artist, it is my attempt when painting to elicit a visceral reaction from the viewer from a visual stimulus, by using colors sometimes with various, water-soluble materials (e.g. salt, alcohol, etc.) to achieve a desired effect; to affect a certain mood; to bring a three-dimensional feel to a two-dimensional piece of paper; to paint big so the viewer is brought into the work; to draw influence from some of my favorite artists, e.g. to take Mark Rothko's fields of color technique, or Jackson Pollock's rhythmic motion of paint dripping, a technique he used, inspired by fluid Native American sand painting techniques; and to apply the complexities of watercolor's behavior to see what possibilities emerge; to let nature's forces guide the fluids within the painting creating flowers as mesmerizing as van Gogh's irises or Pollock's drip patterns. These have been some of the principles by which I used to develop a unique, personal style of abstract and representational painting. One of the challenges within the watercolor medium is leaving some white areas of the canvas. This requires some planning ahead. Seeing different kinds of patterns emerge from interactions between water, pigments, and paper became a series of personal exercises in applied mathematics, physics, and chemistry. For example, what will the results be from different combinations of pigments? What will happen if other fluids are introduced to the system, e.g. isopropyl alcohol or gum Arabic? What if instead of brushing paint onto the paper with a stroke, let

a mass of fluid leave its signature pattern? If given a sizeable volume of watercolor paint, could the final dry painting capture the directional flow of the water, the carrier fluid, along with any patterns left by the settling of the pigments mixed in suspension? Using gum Arabic to make watercolor paints more viscous may offer a new and interesting, creative starting point. As a mathematician, it has been exciting to simplify a painting process into a simple but rigorous procedure to investigate the origin, transient stages, and final form of fractals not only as they occur in art, but hopefully to offer some insight and knowledge into further understanding fractals' application in fluid mechanics.

Overall, a thorough analysis of the physics of watercolor image on canvas can be extremely beneficial to watercolor artists to help render more controlled artistic works. Paint droplets on a substrate frozen for 30 minutes often produce a branch structure similar to microscopic blood vessels, after thawing for two to five minutes. Refreezing a painting at this moment may then permit the pigment to settle into the paper in this formation and allow for the emergence of new paint patterns not only for creative exploration but also for further scientific analysis. The beauty of watercolor painting lies in the complex flow of water along with the physical processes and the chemical reactions that occur within a singular pigment and between different paints. The nature of water allows pigment to open up and become translucent. The technique of wet-on-dry, dry-on-dry are equally valid methods, but wet paper makes for more vibrant colors. By freezing the paper, however, new and different patterns, *e.g.*, fingering, branching, and confined sedimentation, become possible. These new and different patterns would otherwise quickly disperse and be a fleeting moment in the lifespan of the painting process. Figure 71 shows two attempts to capture the branching pattern that occurs about 2 minutes after thawing of a frozen

substrate. Figure 68 is a droplet of the watercolor paint, cadmium red, of unknown viscosity. This painting was created, not only as a new experiment, but also for the fun of painting. The result from this particular painting was strikingly similar to a pattern from a permanent rose droplet-painting, shown in Figure 69. Figure 70a, b, and c are the first series of "frozen paintings" which show spectacular results of fluid flow and pigment deposition. Figure 71a and b are close-ups of a frozen droplet painting made using 5 paints different from the ones used in our experiments, released from a medicine dropper onto a 30-minute frozen substrate of Arches 140 LB paper. The initial drop and radial dispersal of the turquoise paint are clearly visible. Hole pattern 1, a characteristic we analyzed in chapter 2, is seen in the center of the Payne's gray, the cadmium red, and the opera rose. The very dry parts of the canvas captured the initial droplet with fingers, thus the correlation we established between D_f and N is easy to see. The range of different patterns is particularly nice in Figure 72b, e.g. the cadmium red spots left after water absorption, dispersal, and evaporation, the different interactions among the 5 pigments to produce a vibrant orange and a subtle purple, and the sprawling coverage of the Payne's gray, highly likely to be the most viscous paint of that group. What would happen if we were to increase the viscosity of the watercolor paint?

The current study is only the first step in our understanding the physics of watercolor painting. Several interesting key questions remain, including the effect of brush (shear stresses) on canvas and surface tension of paints, as well as the additional component from the Stefan problem for a system undergoing a phase change [67]. A more rigorous analysis of impact velocity is also desired. In addition, while a very complicated task, a theoretical/numerical analysis of the problem is also necessary for us to really appreciate

the underlying physics. There have been some attempts at providing analytical explanations for the drop impact and spreading of liquids on solid surfaces [11,33,34]. These previous studies have incorporated Newtonian and non-Newtonian aspects of the liquids, and also considered the effect of drying of the liquid. In the future, with the inclusion of absorption, these models could be considered toward application to our problem. Several of these ideas are either currently being pursued or will be taken up in our future, ongoing work on this subject.

a b c

Figure 68a, b, and c. Cadmium red (Cadmium sulphoselenide PR 108) drop experiment, March 3, 2016. Canson 90lb paper, unfrozen, height at 6 inches, $D_f = 1.5154$. Conversion to black and white (binary) along with binary inversion.

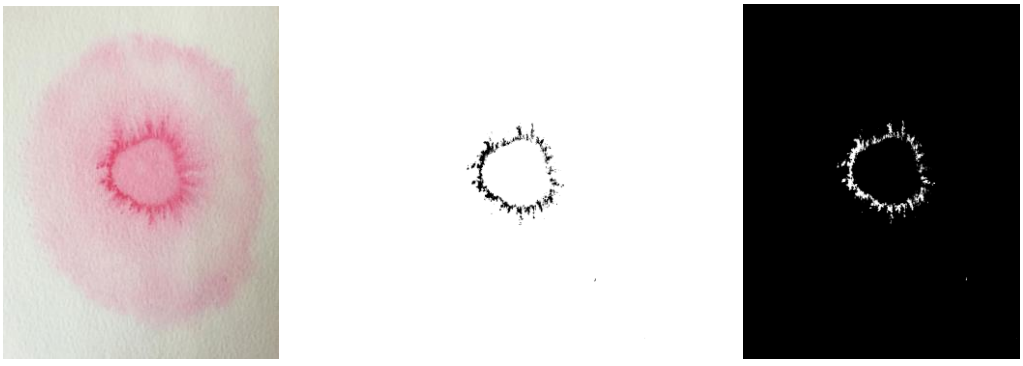

a b c

Figure 69a, b, and c. "Koch Trefoil" - Permanent rose drop experiment, June 10, 2015. Canson 90lb paper, unfrozen, height 6 inches, $D_f = 1.5104$.

Figure 70a, b, c. Three Frozen Paintings. (a) Prussian blue, (b) permanent rose, (c) sepia.

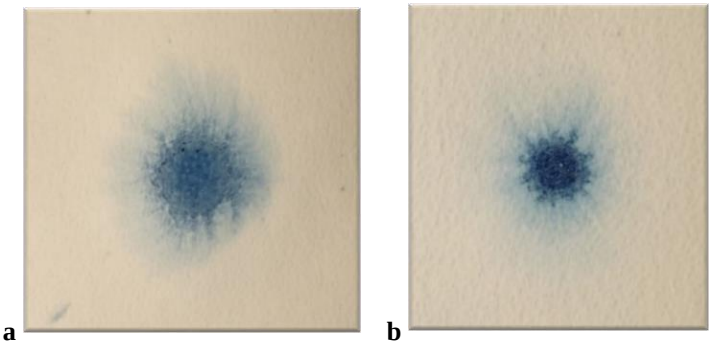

Figure 71a, b. Re-frozen experiment 1 and Re-frozen experiment 2, Prussian blue watercolor paint, Arches 140 LB rough paper.

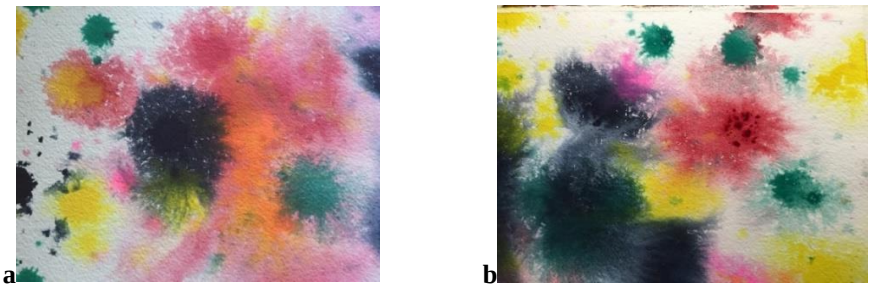

Figure 72a, b. Close-ups frozen substrate painting with drops of Payne's Gray, cadmium red, cobalt turquoise, opera rose, and aureolin yellow watercolor paints on Arches 140 LB rough watercolor paper.

References

1. Lane, R. *Images from the Floating World, The Japanese Print*; Oxford University Press: Oxford, UK, 1978.
2. Taylor, R.; Micolich, A.P.; Jonas, D. The Construction of Jackson Pollock fractal drip paintings. *Leonardo* **2002**, 203-207.
3. Taylor, R.; Micolich, A.P.; Jonas, D. The Construction of Jackson Pollock fractal drip paintings. *Nature* **1999**, *399*,422.
4. Hercynzki, A.; Cernuschi, C.; Mahadevan, L. Painting with drops, jets and sheets. Phys. Today **2011**, *2011*,31-36.
5. Worthington, A.M. *A Study of Splashes*; Longmans: London, UK, 1908; p. 129.
6. Josserand, C.; Thorroddsen, S.T., Drop Impact on a Solid Surface. *Annu. Rev. Fluid Mech*. **2016**, *48*,365-391.
7. Sefiane, K. Patterns from drying drops. *Adv. Colloid Interface Sci.* **2014**, *206*, 372-381.
8. Yarin, A.L. Drop Impact Dynamics: Splashing, Spreading, Receding, Bouncing. *Ann. Rev. Fluid Mech.* **2006**, *38*, 159-192.
9. Rioboo, R; Tropea, C.; Maregno, M. Outcomes from a drop impact on solid surfaces. *At. Sprays* **2001**, *11*, 155-165.
10. Bartolo, D.; Narcy, G.; Boudadoud, A.;Bonn, D. Dynamics of Non-Newtonian Droplets. *Phys. Rev. Lett.* **2007**, *99*, 174502.
11. Luu, L.; Forterre, Y. Drop Impact of yield-stress fluids. *J. Fluid Mech*. **2009**, *632*, 301-327.
12. Marston, J.O.; Mansoor, M.M.; Thoroddsen, S.T. Impact of granular drops. *Phys. Rev. E* **2013**, *88*, 010201.
13. Nicolas, M. Spreading of a drop of neutrally buoyant suspension. *J. Fluid Mech*. **2005**, *545*, 271-280.
14. Peters, I.R.; Xu, Q. and Jaeger, H.M. Splashing onset in dense suspensions. *Phys. Review. Lett*. **2013**, *111*, 028301.
15. Guemas, M.; Marin, A.G.; Lohse, D. Drop Impact experiments of non-Newtonian liquids on micro-structured surfaces. *Soft Matter* **2012**, *8*, 10725-10731.

16. Mysels, K.J. Visual Art: The role of capillarity and rheological properties in painting. *Leonardo* **1981**, *13*, 22-27.
17. Lagubeau, G.; Fontelos, M.A.; Josserand, C.; Maurel, A.; Pagneaux, V.; Petitjeans, P. Spreading dynamics of drop impacts. *J. Fluid Mech*. **2012**, *713*, 50-60.
18. How Watercolor Paints Are Made. Available online: http://www.handprint.com/HP/WCL/pigment1.html (accessed on 15 December 2015).
19. Blair, G.W.S Rheology and Painting. *Leonardo* **1969**, *2*, 51-53.
20. Li, X.; Zhang, H.; Fang Y.; Al-Assaf, S.; Phillips, G.O.; Nishinari, K. Rheological Properties of Gum Arabic Solution: The Effect of Arabinogalactan Protein Complex (AGP). In *Gum Arabic*; Kennedy, J.F.,Phillips, G.O., Williams, P.A., Eds.; Royal Society of Chemistry: London, UK, 2011.
21. Vernon-Carter, E.J.; Sherman, P. Rheological properties and applications of mesquite tree (Prosopis juliflora) gum. 1. Rheological properties of aqueous mesquite gum solutions. *J. Text. Stud*. **1980**, *11*, 339-349
22. Lopez-Franco, Y.L.; Gooycolea, F. M.; Lizardi-Mendoza, *J. Gum of Prosopis/Acacia Species*; Ramawat, K.G., Merillon, J.M., Eds.; Springer International Publishing: Cham, Switzerland, 2015.
23. De Marsily, G. *Quantitative Hydrogeology*; Academic Press Inc.: Orlando FL, USA, 1986.
24. Marmanis, H.; Thorrodsen, S.T. Scaling of the fingering pattern of an impacting drop. *Phys. Fluids* **1996**, *8*, 1344-1346.
25. Rioboo, R.; Marengo, M.; Tropea, C. Time evolution of a liquid drop impact on solid, dry surfaces. *Expts. Fluids* **2002**, *33*, 112-124.
26. Yarin, A.L.; Weiss, D.A. Impact of drops on solid surfaces: self-similar capillary waves, and splashing as a new type of kinematic discontinuity. *J. Fluid Mech*. **1995**, *283*, 141-173.
27. Cossali, G.E.; Coghe, A.; Maregno, M. The impact of a single drop on a wetted solid surface. Exp. *Fluids* **1997**, *22*,463-472.
28. Sivakumar, D.; Tropea, C. Splashing impact of a spray onto a liquid film. *Phys. Fluids* **2002**, *14*, L85-L88.

29. Taylor, R.P.; Guzmana, R.; Martina, T.P.; Halla, G.D.R.; Micolich A.P.; Jonas, D.; Scannella, B.C.; Fairbanks, M.S.; Marlow, C.A. Authenticating Pollock Paintings Using Fractal Geometry. *Pattern Recognit. Lett.* **2007**, *28*, 695.
30. Jones-Smith, K.; Mathur, H.; Krauss, L.M. Drip paintings and fractal analysis. *Phys. Rev. E* **2009**, *79*, doi:10.1103/PhysRevE.79.046111.
31. Joye, Y. Some Reflections on the relevance of fractals for art therapy. *Arts Psychother*. **2006**, *33*, 143-147.
32. Lesmior-Gordon, N. *Introducing Fractal Geometry*; Icon Books Ltd.: Duxford, UK, 2006; p. 176.
33. Howison, S.D.; Moriarty, J.A.; Terrill, E.L.; Wilson, S.K. A mathematical model for drying paint layers. *J. Eng. Math*. **1997**, **32**, 377-394.
34. Kim, H.Y.; Chun, J.H. The recoiling of liquid droplets upon collision with solid surfaces. *Phys. Fluids* **2001**, *13*,643-659.
35. McDonough, J.M. *Lectures in Elementary Fluid Dynamics: Physics, Mathematics and Applications.* University of Kentucky, Lexington, KY 40506-0503, 2009, p. 5-24.
36. How Watercolor Paper Is Made. Available online: http://www.handprint.com/HP/WCL/pigment1.html (accessed on 15 December 2015).
37. Deegan, R.D.; Brunet, P.; Eggers, J. Complexities of Splashing. Institute of Physics, University of Michigan, 2008.
38. Rawlins, F.I.G. The Physics of Painting. The National Gallery of London, U.K. 1941.
39. Mandelbrot, B.B. Fractals and an Art for the Sake of Science. *Leonardo* **1989**, 2, 21-24.
40. Mandelbrot,B.B. The Fractalist: Memoir of a Scientific Maverick. Pantheon Books, New York, USA 2012.
41. Howison, S.D.; Oakendon, J.R.; Oliver, J.M.; Drop Impact on a Thin Fluid Layer. *J. Fluid Mech*. **2004**, 1-21.
42. Lim, S.; Ahn, K.H.; Rheological Properties of Oil Paints and Their Flow Instabilities in Blade Coating. *Rheol. Acta*. **2013**, 52, 643-659.

43. Messaâdi, A.; Dhouibi, N.; Hamda, H.; Belgacem, F.B. M.; Adbelkader, Y.H.; Ouerfelli, N.; Hamzaoui, A.H.; A New Equation Relating the viscosity Arrhenius Temperature and the Activation Energy for some Newtonian Classical Solvents. *J. Chemistry*, **2015**, 163262, 1-12.
44. Thoroddsen, S.T. The Making of a Splash. *J. Fluid Mech*. **2012**, 690, 1-4.
45. Basu, S.; Cetegen, B.M. Analysis of Hydrodynamics and Heat Transfer in a Thin Liquid Film Flowing Over a Rotating Disk by Integral Method. *J. Heat Transfer* **2005**, 1-29.
46. Le Berre, M.; Pomeau, Y. Theory of ice-skating. *Physics Flu. Dyn*. **2015**, 1-15.
47. Grounds, A.; Still, R.; Takashina, K. Enhanced droplet control by transition boiling. *Sci. Reports* **2012**, 2, 1-5.
48. Nariyoshi, R.A.; Shakerin, S. Fluid Dynamics Art Exploration: An undergraduate research course. *Amer. Soc. Eng. Education* **2011**, 1-14.
49. Settles, G.S. On the Fluid dynamicist as artist. Göttingen, Germany, 2006, 1-10.
50. Sreenivasan, K.R. Fractals in Fluid Mechanics. *Fractals* **1994**, 2, 253-263.
51. Aragón, J.L.; Naumis, G.G.; Bai, M.; Torres, M.; Maini, P.K. Kolmogorov Scaling in Impassioned van Gogh Paintings. *Physics* **2006**, 1-5.
52. Aragón, J.L.; Naumis, G.G.; Bai, M.; Torres, M.; Maini, P.K. Turbulent Luminance in Impassioned van Gogh Paintings. *J. Math Imaging Vis*. **2008**, 30, 275-283.
53. Popova, M. The Fluid Dynamics of "The Starry Night": How Vincent van Gogh's masterpiece explains the scientific mysteries of movement and light. www.brainpickings.org, **2014**.
54. Tomassone, M.S.; Krim, J. Fractal scaling behavior of water flow patterns on inhomogeneous surfaces. *Phys. Rev. E* **1996**, 54, 6511-6514.
55. Taylor, R. Personal reflections on Jackson Pollock's fractal paintings. Historía, Ciências, Saúde 2006, Manguinhos, Rio de Janeiro, Brazil, **2006**, 109-123.
56. Ouellette, J. Pollock's fractals: That isn't just a lot of splattered paint on those canvases, it's good mathematics. Discover Magazine **2001**, 1-4.

57. Taylor, R., The curse of Jackson Pollock: The truth behind the world's greatest art scandal. http://www.oregonquarterly.com/winter2010/feature4.php (accessed Feb. 21, **2011**).
58. Krežević, D.; Savić, V. Mathematical modeling of changing dynamic viscosity as a function of temperature and pressure of mineral oils for hydraulic systems. *Mech. Eng*. **2006**, 4, 27-34.
59. Giap, S.G.E. The hidden property of Arrhenius-type relationship: viscosity as a function of temperature. *J. Phys Sci*. **2010**, 21, 29-39.
60. Moore, M.; Howison, S.; Ockendon, J.; Oliver, J. Three-dimensional oblique water-entry problems at small deadrise angles. University of Oxford, Oxford, UK 2012, 1-20.
61. Larrieu, E.; Staron, L.; Hinch, E.J. Raining into shallow water as a description of the collapse of a column of grains. *J. Fluid Mech*. **2006**, 554, 259-270.
62. Lagrée, P.-Y.; Staron, L.; Popinet, S. The granular collapse as a continuum: validity of a two-dimensional Navier-Stokes model with a μ(I)-rheology. *J. Fluid Mech.* **2011**, 1-31.
63. http://www.viscopedia.com/viscosity-tables/substances/water/ (accessed April 6, **2017**).
64. https://en.wikipedia.org/wiki/Temperature_dependence_of_liquid_viscosity (accessed April 6, 2017).
65. Zielinski, D; James Mai, J., Complete Enumeration: A Search for Wholeness. *J. Math and Arts*, 1, 3, **2007**.
66. Irving G.; Segerman, H. Developing Fractal Curves. *J. Math and Arts*, **2013**, 7, 3-4,103-121.
67. Jonsson, T.; On the One-Dimensional Stefan Problem, Umea University, Sweden, **2013**, 1-54.
68. Bountis, T.; Fokas, A.S.; Psarakis, E.Z. Fractal Analysis of Tree Paintings by Piet Mondrian (1872-1944), Inderscience Online, 10, 1, https://doi.org/10.1504/IJART.2017.083902, (accessed July 18, 2017).

Appendix

This first group of Figures 73-75 shows scatter plots investigating the effects from changes to $\boldsymbol{\beta}$, the exponential rate of cooling/heating, for the three cases of paint-drop experiments. Case i: substrate at cold water temperatures, $\boldsymbol{T_0 = 5℃, \beta = 0.010}$, case ii: substrate frozen for 5 minutes, $\boldsymbol{T_0 = -5℃, \beta = 0.031}$, and case iii: substrate frozen for 30 minutes, $\boldsymbol{T_0 = -15℃, \beta = 0.053}$. The fractal dimension was calculated for 200 trials, for each value of $\boldsymbol{\beta}$, to find an average $\boldsymbol{D_f}$ with one standard deviation. Number of fingers N = 700, initial velocity, U, for each finger is a random value between 0 and 1.1 cm/sec. Recall from Figure 50 we saw that $\boldsymbol{D_f}$ increases as T decreases. Prussian blue and sepia paint were discovered to be significantly affected by freezing temperatures. During the melting phase, less pigment is displaced as water, the carrier fluid, disperses. A greater amount of pigment is dispersed for the more viscous permanent rose.

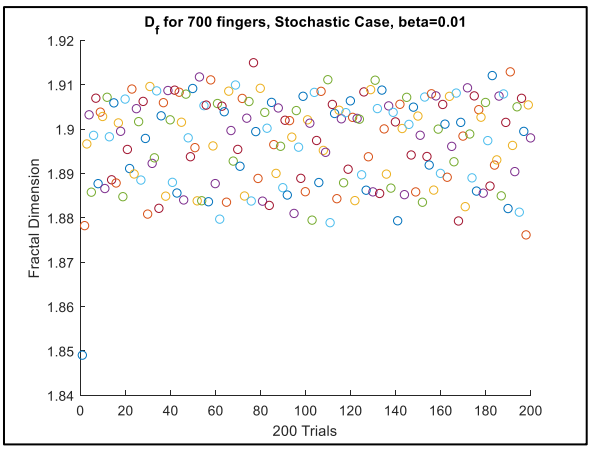

Figure 73. Average $\boldsymbol{D_f = 1.8969}$, standard deviation $\boldsymbol{0.0101}$, exponential rate $\boldsymbol{\beta = 0.01}$.

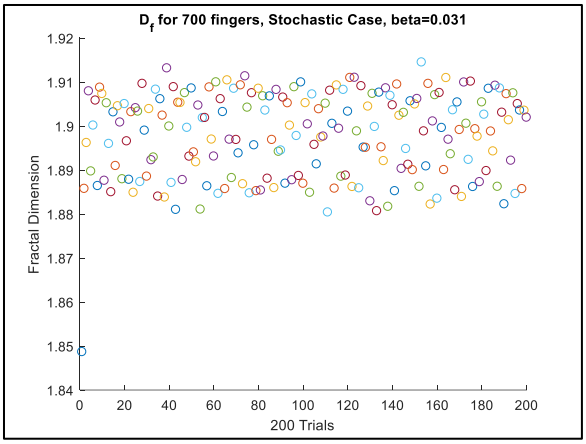

Figure 74. Average $Df = 1.8977$, standard deviation 0.0097, exponential rate $\beta = 0.031$.

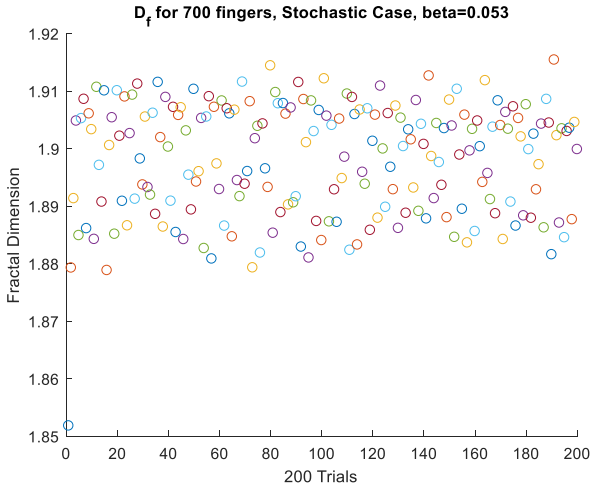

Figure 75. Average $Df = 1.8980$, standard deviation = 0.0098, exponential rate $\beta = 0.053$.

The final groups of Figures 76-80 show scatter plots showing our results for fractal dimension for each final image of our 46-single paint-drop experiments. Our original investigation began by taking a qualitative look at parameters such as height of release, paint viscosity, paper type, i.e. porosity, substrate temperature, and volume of paint-drop.

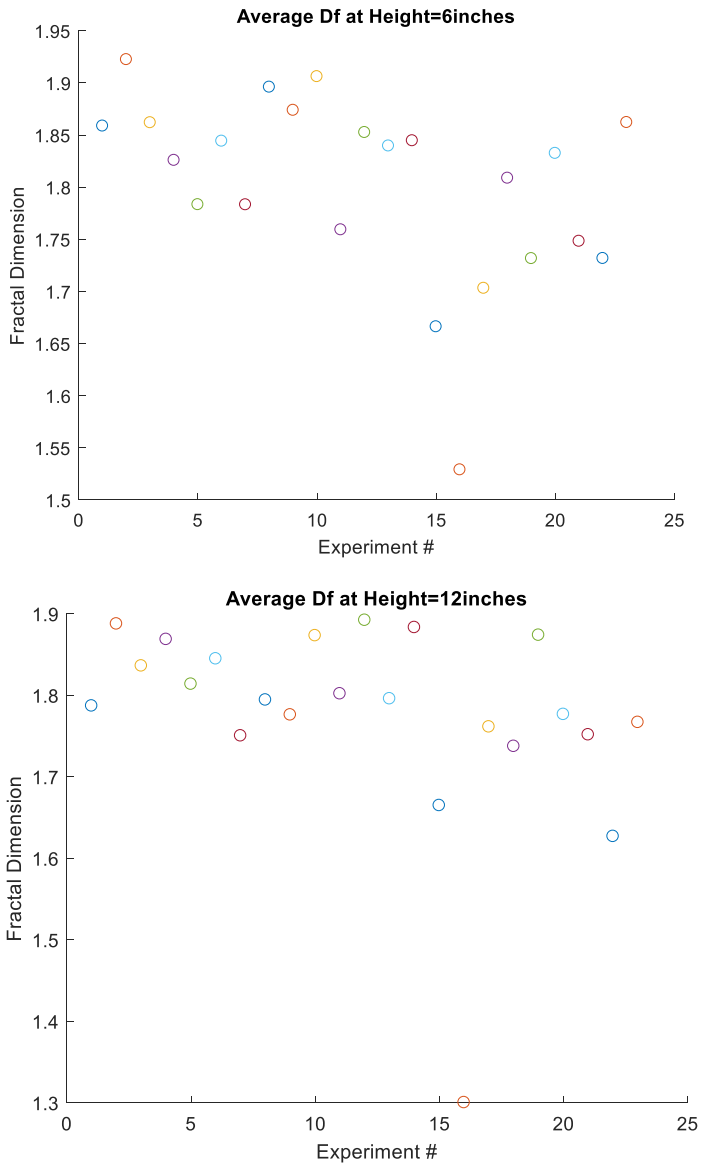

Figure 76. Scatter plot comparing D_f at 6 inches and 12 inches from our paint drop experiments. Fractal dimension values are generally greater for droplets released from a greater release height.

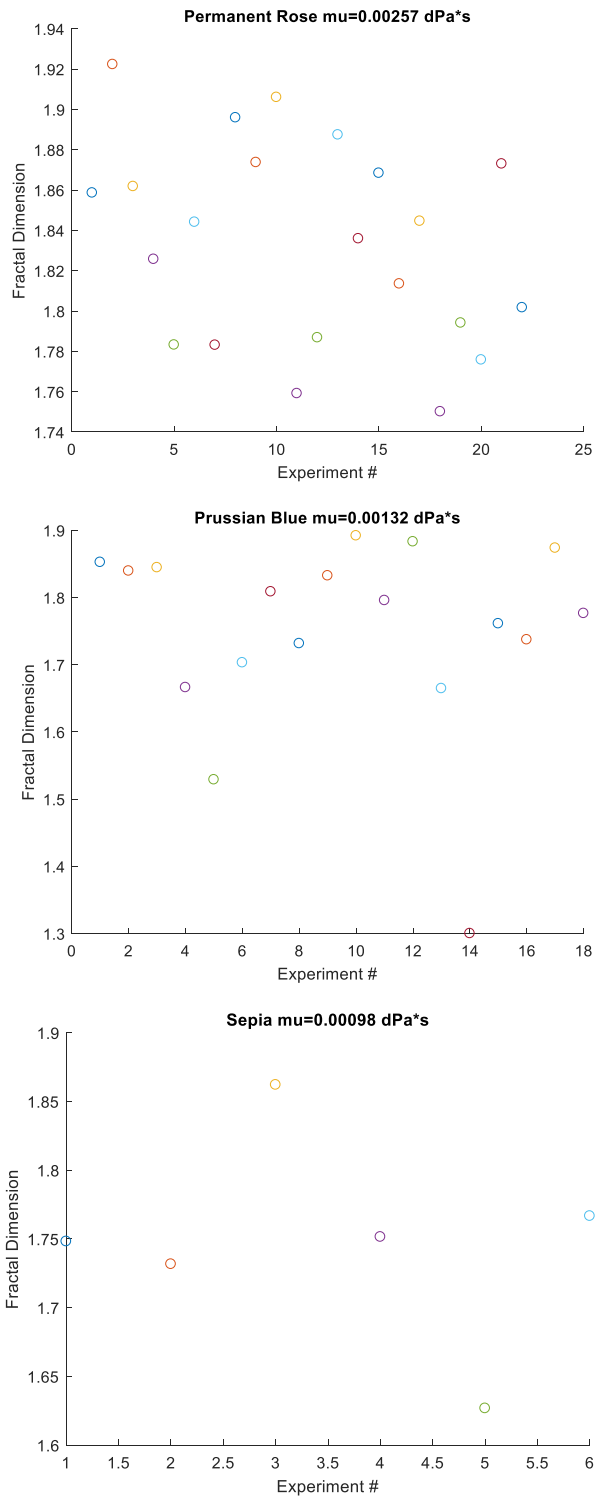

Figure 77. Scatter plots comparing D_f for 3 different viscosities of paint. Permanent rose was determined to have the highest viscosity among the paints we studied. We chose permanent rose on which to base our mathematical model.

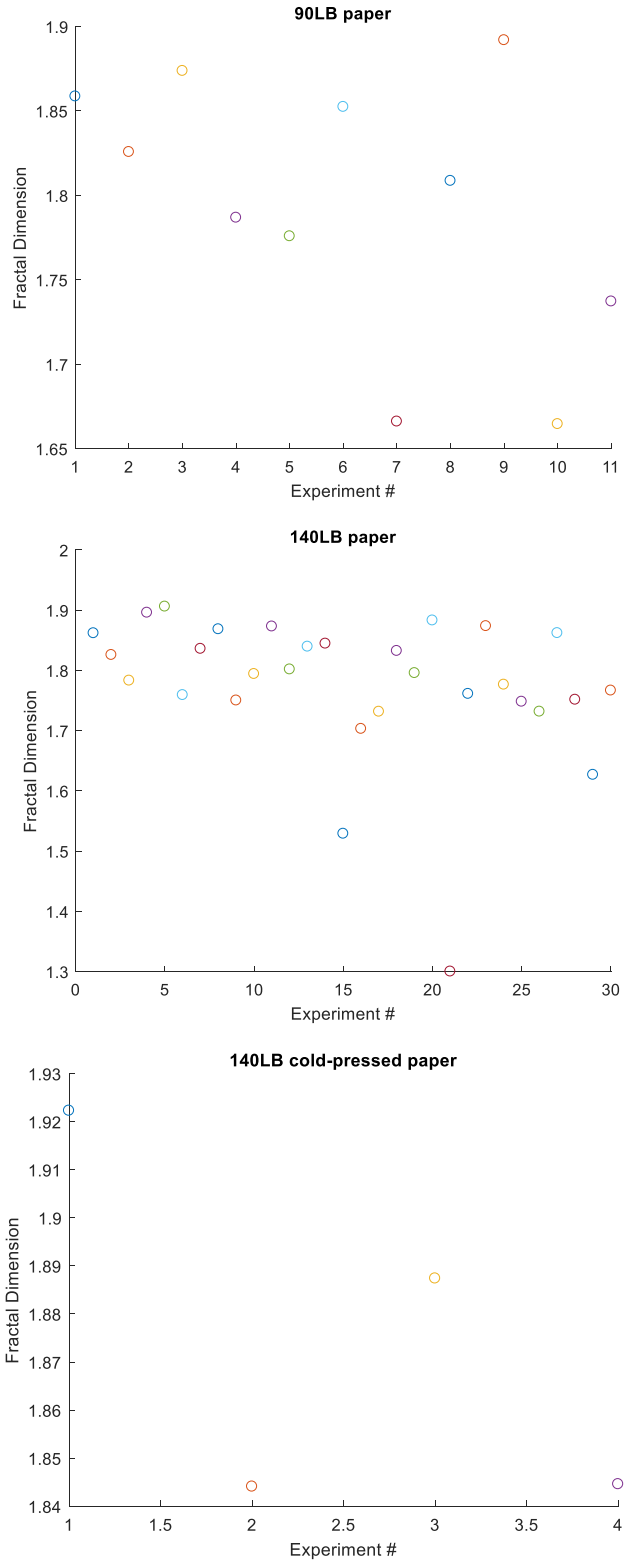

Figure 78. Scatter plots comparing D_f for 3 different types of paper. 90 LB paper, the most porous of the papers we used exhibited the widest range of fractal dimension.

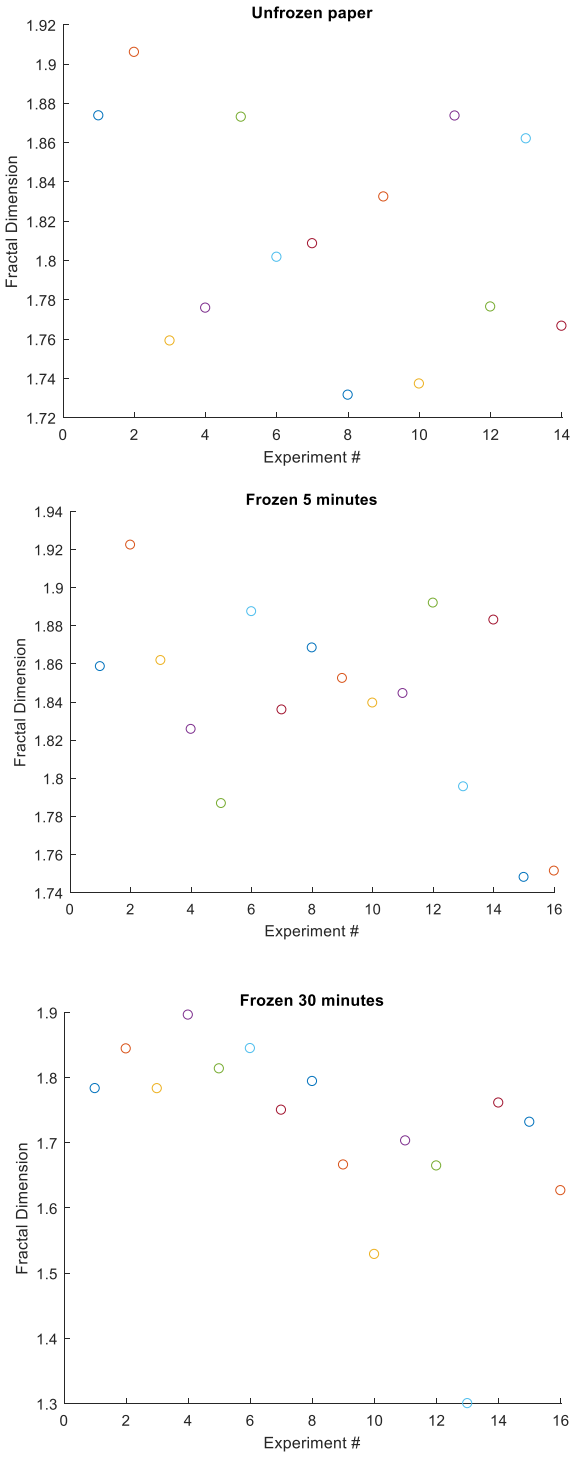

Figure 79. Scatter plots comparing D_f for 3 different substrate temperatures. Freezing temperatures will affect the viscosity of watercolor paint.

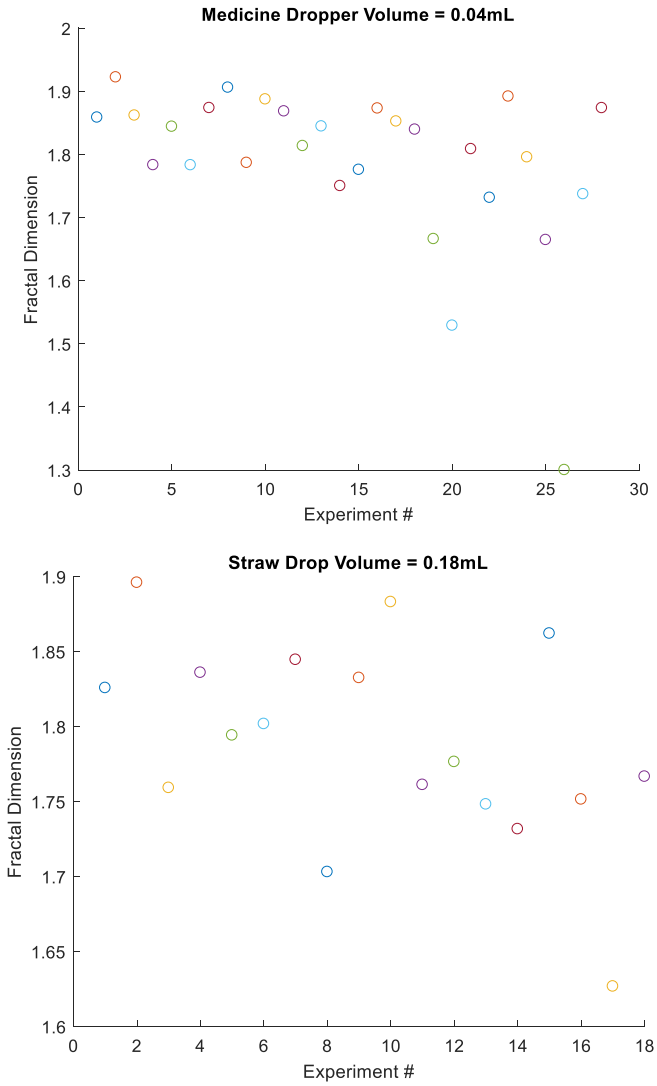

Figure 80. Scatter plots comparing D_f for 2 different volumes of paint drops. The volume of a droplet released from a straw is greater than the volume of the medicine dropper.

MATLAB code for Numerical Simulations

```
function model4
%  Inertial Spread for Droplet
%  Use ode45 to solve system of differential equations
%  dh/dt = -2Uh/R
%  dR/dt = U
%  dU/dt = -tau_b/(rho*h)
%  h = height of droplet
%  R = radius of droplet
%  U = velocity of radialy spreading droplet
%  tau_b = basal shear force figure(1)
%  rho = density of fluid
%  mu = viscosity
close all
clc
rho = 998.228;  %Density of Permanent Rose kg/cubic meters
alpha = 0.02;
T_R = 25;
T_0 = 8;
mu_0 = 0.00257;  % viscosity of permanent rose Pa*s
%mu_0 = 0.00132;  % viscosity of Prussian blue Pa*s
%mu_0 = 0.00098;   % viscosity of sepia Pa*s
%beta = 0.053;
%beta = 0.031;
beta = 0.01;
t_final = 40;
delta_t = 0.01;
T = zeros((t_final)*100+1,1);
V = zeros((t_final)*100+1,1);
%
T(1) = T_0;
V(1) = mu_0*exp(-alpha*((T_0-T_R)));
j=2;
for i = delta_t:delta_t:t_final
   T(j) = T_R+(T_0-T_R)*exp(-beta*i);
   V(j) = mu_0*exp(-alpha*((T_0-T_R)*exp(-beta*i)));
   j = j+1;
end
%velocity = (randi([0,10])+rand)/1000;
velocity = 0.003265;
f = @(t,x)[(-2*x(3)*x(1))/x(2);x(3);
   -(mu_0*(exp(-alpha*(T_0-T_R))*exp(-beta*t)))*x(3)/(rho*x(1)^2)];
[t,xa] = ode45(f,0:delta_t:t_final,[0.0275 0.0171 velocity]);
figure(1)
plot(t,xa(:,1))
title('Height h(t)')
xlabel('time(seconds)'),ylabel('height(meters)')
%
figure(2)
```

```
plot(t,xa(:,2))
title('Radius R(t)')
xlabel('time(seconds)'),ylabel('radius(meters)')
%
figure(3)
plot(t,xa(:,3))
title('Velocity U(t)')
xlabel('time(seconds)'),ylabel('velocity(m/s)')
%
figure(4)
plot(t,T)
title('Temperature T(t)')
xlabel('time (seconds)'),ylabel('Temperature deg Celsius')
%
figure(5)
plot(t,xa(:,2))
title('Radius R(t)')
hold on
%
%y_bar = 0.0123*(t.^0.471);
%y_bar = 0.0171*(t.^0.194);
y_bar = 0.0162*(t.^0.091)
plot(t,y_bar,'--k')
%
hold on
% RadiusData = xlsread('myData.xlsx','Sheet5');
RadiusData = xlsread('Thesis_Data_PermRose_FrozenExperiment.xlsx','Sheet3');
X = RadiusData(:,1);
Y = RadiusData(:,3);
plot(X,Y,'om')
%
xlabel('time(seconds)'),ylabel('Radius (meters)')
%
figure(6)
plot(t,V)
title('Viscosity mu(t)')
xlabel('time (seconds)'),ylabel('Mu (Pa*s)')
%
figure(7)
plot(t,xa(:,3))
title('Acceleration dU(t)/dt meters/sec^2')
xlabel('time (seconds)'),ylabel('velocity (m/s)')
hold on
% RadiusData = xlsread('myData.xlsx','Sheet5');
RadiusData = xlsread('Thesis_Data_PermRose_FrozenExperiment.xlsx','Sheet3');
X = RadiusData(:,1);
Y = RadiusData(:,4);
plot(X,Y,'om')
%
disp('Initial Height  Radius  Velocity')
%
```

```
disp(xa(1,:))
%
disp(' Final Height  Radius  Velocity')
%
disp(xa(end,:))  % display the last row of xa values
%
disp('Initial Temperature')
disp(T(1))
%
disp('Initial Viscosity')
disp(V(1))
%
disp('Final Temperature')
disp(T(end))
%
disp('Final Viscosity')
disp(V(end))
%

function initialspread2(trial,rho,mu_0,alpha,beta,r,s,T_0,T_R,initial_height,initial_radius,num)
%function initialspread2(rho,mu_0,alpha,beta,r,s,T_0,T_R,initial_height,initial_radius,num)

%  It is advised to run the script for model4.m to determine
%  the time at which the radius reaches a maximum distance
%  for the chosen fluid parameters and ode45 Initial Conditions.
%  Time intervals can then be adjusted accordingly.
%
%
%  Run ode45 for the entire droplet on first time interval
t_one_circumference_points = ceil(1/num);
%
del = 0;
% initialize arrays for:
%
d = zeros(t_one_circumference_points,1);
%
C = zeros(t_one_circumference_points,1); % array for final velocities
H = zeros(t_one_circumference_points,1); % array for final heights
R = zeros(t_one_circumference_points,1); % array for final radii
D = zeros(t_one_circumference_points,1); % x-coordinates,
E = zeros(t_one_circumference_points,1); % y-coordinates,
radii = zeros(t_one_circumference_points,1); % to keep track of all the radii end values
heights = zeros(t_one_circumference_points,1); % to keep track of all the height end values
velocities = zeros(t_one_circumference_points,1); % to keep track of all the velocity end values
% %angles
ang = 2*pi/t_one_circumference_points;
i = 1;
for step = 1:t_one_circumference_points
   %velocity = 0.00327; % velocity of radially spreading droplet from experiment
   %velocity = randi([0 10]);
   %velocity = (randi([0,5])+rand)/1000;
```

```
    velocity = (randi([0,10])+rand)/1000;
    %velocity = rand/10;
    %f = @(t,x)[(-2*x(3)*x(1))/x(2);x(3);(-mu*x(3)/(rho*x(1)^2))];
    f = @(t,x)[(-2*x(3)*x(1))/x(2);x(3);(-(mu_0*(exp(-alpha*(T_0-T_R))*exp(-
beta*t)))*x(3)/(rho*x(1)^2))];
    %f = @(t,x)[(-2*x(3)*x(1))/x(2);x(3);(-(mu_0+mu_0*(exp(-alpha*(T_0-T_R))*exp(-
beta*t)))*x(3)/(rho*x(1)^2))];
    [t,xa] = ode45(f,0:0.01:5,[initial_height initial_radius velocity]);
    [e] = xa(:,1); %height of droplet after first time interval
    [d] = xa(:,2); %radius of droplet after first time interval
    [c] = xa(:,3); %velocity of droplet spread after first time interval
    radii(i) = d(end);
    heights(i) = e(end);
    velocities(i) = c(end);
    %maximum_velocity = max(velocities);
    D(i) = (d(end))*cos(del);E(i) = (d(end))*sin(del);
    H(i) = e(end);
    C(i) = c(end);
    R(i) = d(end);
    plot([initial_radius*cos(del) D(step)],[initial_radius*sin(del) E(step)],'-b');
    hold on
    plot(r+D(step),s+E(step),'.g');
    hold on
    i = i+1;
    del = del+ang;
end
longest_finger = max(R);
average_radius = mean(R);
radius_standard_deviation = std(R);
% %
average_final_height = mean(H);
height_standard_deviation = std(H);
% %
average_initial_velocity = mean(c);
maximum_initial_velocity = max(c);
minimum_initial_velocity = min(c);
velocity_standard_deviation = std(c);
%
cell_one = sprintf('A%s',num2str(trial));
cell_two = sprintf('B%s',num2str(trial));
cell_three = sprintf('C%s',num2str(trial));
cell_four = sprintf('D%s',num2str(trial));
cell_five = sprintf('E%s',num2str(trial));
cell_six = sprintf('F%s',num2str(trial));
cell_seven = sprintf('G%s',num2str(trial));
cell_eight = sprintf('H%s',num2str(trial));
cell_nine = sprintf('I%s',num2str(trial));
%
% filename = 'Thesis_Data_CircumPts.xlsx';
% filename = 'Thesis_Data_Stochastic_Case.xlsx';
% filename = 'Thesis_Data_Stochastic_Velocity.xlsx';
```

```
filename = 'Thesis_Data_Temperatures_nonHomogeneous.xlsx';
sheet = 8;
xlswrite(filename,longest_finger,sheet,cell_one);
xlswrite(filename,average_radius,sheet,cell_two);
xlswrite(filename,radius_standard_deviation,sheet,cell_three);
xlswrite(filename,average_final_height,sheet,cell_four);
xlswrite(filename,height_standard_deviation,sheet,cell_five);
xlswrite(filename,average_initial_velocity,sheet,cell_six);
xlswrite(filename,maximum_initial_velocity,sheet,cell_seven);
xlswrite(filename,minimum_initial_velocity,sheet,cell_eight);
xlswrite(filename,velocity_standard_deviation,sheet,cell_nine);


function hausdorffrun(trial)
%%%%%%%%%%%
% this is used to find the hausdorff dimension via the box counting method
% email: p.french@ee.ucl.ac.uk
% web: www.ee.ucl.ac.uk/~pfrench
%%%%%%%%%%%
close all
%clear
%clc
table =[1,2];

% load up original image and convert to gray-scale
%
p = imread('OutputFile.png');
%
%
figure(1)
imshow(p)
K = im2bw(p,0.5275);
figure(2)
imshow(K)
%L = im2bw(p,0.3);
M = imcomplement(K);
figure(3)
imshow(M)
% scan each block to see if the edge occupies any of the blocks.
% If a block is occupied then flag it and record it in boxCount --
% store both size of blocks (numBlocks) and no of occupied boxes (boxCount)
% in table()
Nx = size(M,1);
Ny = size(M,2);

for numBlocks = 1:400

    sizeBlocks_x = floor(Nx./numBlocks);
    sizeBlocks_y = floor(Ny./numBlocks);

    flag = zeros(numBlocks,numBlocks);
```

```
    for i = 1:numBlocks
        for j = 1:numBlocks
            xStart = (i-1)*sizeBlocks_x + 1;
            xEnd   = i*sizeBlocks_x;

            yStart = (j-1)*sizeBlocks_y + 1;
            yEnd   = j*sizeBlocks_y;

            block = M(xStart:xEnd, yStart:yEnd);

            flag(i,j) = any(block(:)==1); %mark this if ANY part of block is true
        end
    end
    boxCount = nnz(flag);
    table(numBlocks,1)    = numBlocks;
    table(numBlocks,2)    = boxCount;
end


% from the above table of discrete points, take a line of best fit and plot
% the raw data (ro) and line of best fit (r-)
x      = table(:,1);    % x is numBlocks
y      = table(:,2);    % y is boxCount

p      = polyfit(x,y,1);
BestFit = polyval(p,x);

figure(4)
hold on
grid on
plot(x,y,       'ko','LineWidth',1)
plot(x,BestFit, 'k-','LineWidth',2)
xlabel('Number of blocks, N','FontSize',12)
ylabel('Box Count, N(s)','FontSize',12)

% calculate Hausdorff Dimension
x2 = log(x);
y2 = log(y);

p2      = polyfit(x2,y2,1);
BestFit2 = polyval(p2,x2);

figure(5)
hold on
grid on
plot(x2,y2,       'bo','LineWidth',1)
plot(x2,BestFit2, 'b-','LineWidth',2)
xlabel('Number of blocks, log N','FontSize',12)
ylabel('Box Count, log N(s)'    ,'FontSize',12)
%
HausdorffDimension = p2(:,1);
```

```
%
cell_ten = sprintf('J%s',num2str(trial));
% filename = 'Thesis_Data_CircumPts.xlsx';
% filename = 'Thesis_Data_Temperatures_350fingers.xlsx';
filename = 'Thesis_Data_Temperatures_halfU.xlsx';
% filename = 'Thesis_Data_Stochastic_Case.xlsx';
% filename = 'Thesis_Data_Stochastic_Velocity.xlsx';
% filename = 'Thesis_Data_Temperatures_nonHomogeneous.xlsx';
% filename = 'Thesis_Data_Comparison.xlsx';
Df= HausdorffDimension;
sheet = 8;
xlswrite(filename,Df,sheet,cell_ten)
```